

**Theory and applications of confocal micro-Raman
spectroscopy on hybrid polymer coatings and
PDMS membranes and spectroscopic studies of
doped B₂O₃-Bi₂O₃ glass systems**

Dissertation

zur Erlangung des
naturwissenschaftlichen Doktorgrades
der Bayerischen Julius-Maximilians Universität Würzburg

vorgelegt von

Gheorghe Lucian Baia

aus
Tîrnăveni, Rumänien

Würzburg 2002

Eingereicht am:.....
bei der Fakultät für Chemie und Pharmazie.

1. Gutachter:.....
2. Gutachter:.....
der Dissertation.

1. Prüfer:.....
2. Prüfer:.....
der mündlichen Prüfung.

Tag der mündlichen Prüfung:.....

Doktorurkunde ausgehändigt am:.....

Content

1. Introduction.....	1
2. Theoretical background.....	5
2.1. Molecular vibrations.....	5
2.2. Infrared spectroscopy.....	9
2.3. Raman spectroscopy.....	9
2.3.1. Confocal micro-Raman spectroscopy.....	10
2.3.2. Resonance Raman spectroscopy.....	12
2.3.3. FT Raman spectroscopy.....	13
3. Experimental.....	16
3.1. Samples preparation.....	16
3.2. Sample measurements.....	18
4. Modelling and measuring the effect of refraction and diffraction on the focus lengthening on confocal micro-Raman experiments.....	21
4.1. Introduction.....	21
4.2. The effect of refraction on the depth resolution of confocal micro-Raman microscopy.....	24
4.2.1. Ray tracing analysis	24
4.2.2. Laser intensity distribution.....	30
4.2.3. Confocal micro-Raman response profile.....	32
4.2.4. Comparison of theory with experimental results.....	35
4.3. The influence of both refraction and diffraction effects on the depth resolution on confocal micro-Raman microscopy.....	42
4.3.1. Laser intensity distribution.....	42
4.3.2. Micro-Raman response profile.....	45

Content

4.3.3. Confocal micro-Raman response profile.....	47
4.3.4. Comparison of theoretical data with experimental results.....	50
4.5. Conclusion.....	54
5. Characterisation of diffusion-processes of pharmacologically relevant molecules through PDMS-membranes by means of confocal resonance micro Raman spectroscopy.....	56
5.1. Introduction.....	56
5.2. Results and discussion.....	58
5.3. Conclusion.....	63
6. Spectroscopic investigations of copper and iron doped B_2O_3 - Bi_2O_3 glass systems	65
6.1. Structural investigations of copper doped B_2O_3 - Bi_2O_3 glasses with high bismuth oxide content.....	65
6.1.1. Introduction.....	65
6.1.2. Results and discussion.....	67
6.1.3. Conclusion.....	77
6.2. Spectroscopic investigations of highly iron doped B_2O_3 - Bi_2O_3 glasses.....	78
6.2.1. Introduction.....	78
6.2.2. Results and discussion.....	79
6.2.3. Conclusion.....	91
7. Summary/Zusammenfassung.....	92
7.1. Summary.....	92
7.2. Zusammenfassung.....	96
References.....	100
Appendix.....	108

Abbreviations

CCD	Charge Coupled Device
DMSO	dimethyl sulfoxide
<i>d.o.f.</i>	depth of focus
FT	Fourier Transform
FWHM	full width at half maximum
GLYMO	3-(glycidoxypropyl)trimethoxysilane
<i>l</i>	length of the focus
<i>NA</i>	numerical aperture
<i>NA_{eff}</i>	“effective” numerical aperture
PDMS	polydimethylsiloxane
PSF	point spread function
PVC	polyvinyl chloride
PVDF	poly(vinylidene fluoride)
TESSA	3-(triethoxysilyl)propyl succinic anhydride

1

Introduction

Infrared and Raman spectroscopy have both a long and interesting history and an illustrious record of contributions to science. Infrared spectroscopy is older than Raman spectroscopy by 128 years and was discovered in 1800 by William Herschel.¹ After the second World War the infrared spectroscopy has represented a standard method primarily due to the development of sensitive infrared detectors and advances in electronics. A second major infrared advance occurred in the 1970s when the development and incorporation of computers within spectrometers enabled the multiplex and energy-throughput advantages of interferometry to be exploited. Fourier transform mathematical analysis of the interferogram was used to derive conventional intensity versus frequency spectra. The infrared source documents for this period are the

comprehensive book published in 1986 by Griffiths and de Haseth² and a set of papers by Miller³, Wilks⁴, Griffiths⁵, Sheppard⁶ and Beckman.⁷

The inelastic scattering of photons, named the Raman effect after its experimental discoverer, was first observed in 1928, and provides an important method for studying the frequency ranges associated with molecular vibrations and rotations. Raman and Krishnan⁸ discovered the effect in Calcutta in 1928 while studying the scattering of sunlight, made quasi-monochromatic by the use of a filter, by liquids. Smekal⁹ had theoretically predicted that such an effect is possible, while Landsberg and Mandelstam¹⁰ have independently observed the effect in light scattering in quartz but published their results shortly after Raman and Krishnan's paper in *Nature*. In an article published in 1934, Placzek¹¹ comprehensively laid out the theory for selection rules, relative intensities and polarizations of features in Raman spectra. By 1940s, Raman spectroscopy had become an important method of non-destructive chemical analysis,^{12,13} showing its wide-ranging applications. These included vibrational studies of smaller molecules, which, in conjugation with infrared data, enabled complete or near complete assignments of the frequencies of the fundamental normal modes. From the development of lasers in the 1960s as ideal and intense monochromatic excitation source Raman spectroscopy became widely applied to a variety of problems.¹⁴⁻¹⁹

Twenty five years ago it was shown²⁰ that the best way to develop micro-Raman instruments was to use a microscope for both illuminating the sample and collecting the Raman light. Indeed, microscope objectives with high numerical aperture (*NA*) optics are able to focus the laser beam into a very small volume and to collect the light scattered by this volume under a wide angle. Thus, both the enormous increase of the local irradiance and the wide angle of collection compensate for the decrease of the number of molecules in the probed volume. Moreover, the use of a microscope allows the user to observe the sample precisely and to select any part of interest for micro-Raman experiments. However, the optical coupling between the microscope and the spectrometer must be optimised all along the optical path. In addition the use of a pinhole, which is placed at the back focal plane of the microscope, provides a substantially improvement of the spatial resolution. Unlike the conventional microscope

where the entire field of view is uniformly illuminated and observed, the “confocal” arrangement takes benefit from the combined effects of spatial filtering by optically conjugated pinhole diaphragms. Such a system isolates the light originating from a small region of the sample coincident with the illuminated spot, and efficiently eliminates the contribution from out-of-focus zones, making the Raman investigation of micron-sized sample volumes possible.

In the present work two principal techniques are employed, infrared absorption and Raman spectroscopy. The first part of the work contributes to a better understanding of physical phenomena, which occur in sample when confocal micro-Raman measurements are employed, making easier a future vibrational characterization of different levels into the sample. The determination of diffusion properties of molecules across membranes by using the same spectroscopic technique represents an important step in the pharmacological research, opening new ways of the application possibilities of this spectroscopic method. In the second part of this work the vibrational characterization of a material structure with high applicability, such as doped B_2O_3 - Bi_2O_3 glasses, performed by means of infrared absorption and Raman spectroscopy, demonstrates the great potential of the above mentioned techniques, when are simultaneously applied, for obtaining relevant structural information from such materials. The following paragraphs describe briefly the content of all chapters, which constitute the present work.

Chapters 2 and 3 contain a very short general description of the Raman and infrared spectroscopy terms, and confocal micro-Raman spectroscopy in particular. The experimental part makes up the next chapter and contains details about the sample preparation and measurements.

A relatively new and not very well understood spectroscopic technique, which showed an exponentially increase in interest in the last decade due to its non-destructive capabilities, is confocal micro-Raman spectroscopy. Chapter four presents a rather detailed theoretical-experimental study, which includes the application of a model that describes the influence of the refraction effect on the focus length on confocal micro-

Raman experiments, the development of a new model that additionally considers the effect of diffraction on the focus dimensions, and a comparison between the experimental and theoretical data followed by a discussion of the observed differences. A parallel comparison between these two theoretical approaches is also drawn throughout of this section.

The next chapter deals with the characterisation of diffusion processes of pharmacologically relevant molecules (β -carotene dissolved in dimethylsulfoxide) through a polydimethylsiloxane (PDMS)-membrane by means of confocal resonance Raman spectroscopy. The diffusion rate as a function of the measurement depth and diffusion time as well as the concentration gradient under a steady flux have been determined, the measurements showing that the confocal micro-Raman technique is a powerful tool to investigate the kinetics of diffusion processes within a membrane before the steady state has been reached.

In chapter 6 infrared and Raman spectroscopic studies of copper and iron doped B_2O_3 - Bi_2O_3 glass systems are performed in order to obtain specific data regarding their local structure and the role played by dopant ions on boron and bismuthate units. The interest for these doped glasses is determined by their many fold possible applications, such as non-linear optical and electronically uses.²¹ The statistical disorder characteristic of B_2O_3 - Bi_2O_3 based glasses, e.g. variations in ring sizes, bond angles, and coordination numbers, combining to give topological disorder, means that there is no translational symmetry, in contrast to the situation in crystalline materials. Therefore, complementary structural studies are essential in order to obtain as much insight as possible into the structure of these glasses. Our goal was also to evidence the changes of B_2O_3 and Bi_2O_3 structural units due to the relaxation of the amorphous structure, which is induced in these samples by the thermal treatment.

The last chapter of the present work contains conclusions drawn from all above mentioned topics.

2

Theoretical background

2.1. Molecular vibrations

Molecules consist of atoms which have a certain mass and are connected by elastic bonds. As a result, they can perform periodic motions, and have vibrational degrees of freedom. All motions of the atoms in a molecule relative to each other are a superposition of so-called *normal vibrations*, in which all atoms are vibrating with the same phase and normal frequency. Their amplitudes are described by a *normal coordinate*. Polyatomic molecules with N atoms possess $3N - 6$ normal vibrations (linear ones have $3N - 5$ normal vibrations), which define their vibrational spectra. These spectra depend on the masses of the atoms, their geometrical arrangement, and

the strength of their chemical bonds. In “super molecules” such as crystals or complexes the vibrations of the individual components are coupled.

The simplest model of a vibrating molecule describes an atom bound to a very large mass by a weightless spring. The force F , which is necessary to move the atom by a certain distance x from an equilibrium position, is given by Hooke’s law, and is proportional to the force constant f_b , which represents a measure of the bond

$$F = -f_b \cdot x. \quad (2.1)$$

By using Newton’s law, from where the force is also proportional to the mass M and its acceleration (the second derivate of the elongation with respect to the time, d^2x/dt^2), and solving the second order differential equation, which possesses the solution

$$x = x_0 \cdot \cos(2 \cdot \pi \cdot \nu \cdot t + \varphi), \quad (2.2)$$

where φ represents the phase angle, the frequency of the vibration of the mass connected to a very large mass by an elastic spring can be expressed²² as follows:

$$\nu = \frac{1}{2 \cdot \pi} \cdot \sqrt{\frac{f_b}{M}}. \quad (2.3)$$

If a diatomic molecule is considered, the mass M is called *reduced mass* of the diatomic molecule with the masses M_1 and M_2 and is given by the following formula:

$$\frac{1}{M} = \frac{1}{M_1} + \frac{1}{M_2}. \quad (2.4)$$

Eq. 2.3 gives the frequency ν (in Hz, s^{-1}) of the vibration. In vibrational spectroscopy, it is common to use wavenumber $\tilde{\nu}$ (in cm^{-1}) instead of frequency, which is the reciprocal wavelength λ :

$$\tilde{\nu} = \frac{\nu}{c} = \frac{1}{\lambda}. \quad (2.5)$$

The potential energy of a molecule, which obeys Hooke’s law, is obtained by integrating Eq. 2.1, and has the following expression:

$$V = \frac{1}{2} \cdot f \cdot R^2 \quad (2.6)$$

in which $R = x - x_c$, x_c representing the Cartesian coordinate of the potential minimum. Because the atoms vibrate with a definite frequency, according to the cosine function in Eq. 2.2, the potential energy given by Eq. 2.6 represents the harmonic potential of a molecule. In the complex structure of the substances the molecular potentials are not exactly harmonic, therefore, an expression for an anharmonic potential was necessary. Thus, anharmonic molecular potentials have been represented by approximate functions, e.g., the Morse function²³ :

$$V = D \cdot \left[1 - \exp\left(-R \cdot \sqrt{\frac{f_e}{2 \cdot D}}\right) \right]^2, \quad (2.7)$$

where f_e is the force constant near the potential minimum and D stands for the dissociation energy. There are other empirical potential functions which are especially useful to describe intermolecular potentials, i.e., the potentials between atoms, which are not connected by chemical bonds.^{24,25} According to classical mechanics, a harmonic oscillator may vibrate with any amplitude, which means that it can possess any amount of energy, large or small. However, quantum mechanics shows that molecules can only exist in definite energy states. In the case of harmonic potentials, these states are equidistant,

$$E_i = h \cdot \nu \cdot \left(v_i + \frac{1}{2} \right), \quad v_i = 0, 1, 2, \dots \quad (2.8)$$

while for anharmonic potentials the distances between energy levels decrease with increasing energy. In Eq. 2.8 h and ν represent the Planck constant and the vibrational quantum number of each energy level, respectively. For $v_i = 0$ the potential energy has its lowest value, which is not the energy of the potential minimum. This is the so called zero point energy. This energy cannot be removed from the molecule, even at temperatures approaching absolute zero.

For polyatomic molecules the frequency of normal vibrations may be calculated by applying the Lagrange equation to expressions of the kinetic and potential energy of the molecule.²⁶ Generally, the potential function of a polyatomic molecule can be described by a Taylor series:

$$V(r) = V_0 + \sum_i f_i \cdot R_i + \frac{1}{2} \cdot \sum_{i,j} f_{i,j} \cdot R_i \cdot R_j + \frac{1}{6} \cdot \sum_{i,j,k} f_{ijk} \cdot R_i \cdot R_j \cdot R_k + \dots, \quad (2.9)$$

where the R_i are suitable displacement coordinates from the equilibrium geometry at a potential minimum and the constants

$$f_i = \left(\frac{\partial V}{\partial R_i} \right)_0; \quad f_{ij} = \left(\frac{\partial^2 V}{\partial R_i \cdot \partial R_j} \right)_0; \quad f_{ijk} = \left(\frac{\partial^3 V}{\partial R_i \cdot \partial R_j \cdot \partial R_k} \right)_0 \quad (2.10)$$

are called linear, quadratic, cubic, etc. force constants. The potential can be defined such that $V_0 = 0$. By definition, the second term in Eq. 2.9 is equal to zero, because the molecule is regarded as to be in its equilibrium.²⁷ Due to the fact that the cubic and higher terms have many components with a comparatively small value and are difficult to be determined, the potential function has the form:

$$V = \frac{1}{2} \cdot \left(\frac{\partial^2 V}{\partial R_i \cdot \partial R_j} \right)_0 \cdot R_i \cdot R_j = \frac{1}{2} \cdot \sum_{i,j} f_{ij} \cdot R_i \cdot R_j. \quad (2.11)$$

The diagonal force constants f_{ij} with $i = j$ describe the elasticity of a bond according to Hooke's law. The interaction force constants, the constants with $i \neq j$, describe the change of the elastic properties of one bond when another bond is deformed. Thus, the force constants of the bonds, the masses of the atoms, and the molecular geometry determine the frequencies and the relative motions of the atoms.

Infrared and Raman spectroscopy represent two of the most important methods used in vibrational spectroscopy. Depending on the nature of the vibration, which is determined by the symmetry of the molecule, vibrations may be active or forbidden in the infrared or Raman spectrum. Perhaps the most important point, which arises when both infrared and Raman spectroscopy are used, is represented by the fact that both provide complementary images of molecular vibrations, because in these spectroscopic techniques the mechanisms of the interaction of light quanta with molecules are quite different.

2.2. Infrared spectroscopy

Infrared spectra are usually recorded by measuring the transmittance of light quanta through a continuous distribution of the sample. Interaction of infrared radiation with a vibrating molecule is only possible if the electric vector of the radiation field oscillates with the same frequency as does the molecular dipole moment. A vibration is infrared active only if the molecular dipole moment is modulated by the normal vibration,

$$\left(\frac{\partial\mu}{\partial q}\right)_0 \neq 0, \quad (2.12)$$

where μ is the molecular dipole moment and q stands for the normal coordinate describing the motion of the atoms during a normal vibration. If the condition (Eq. 2.12) is fulfilled, then the vibrations are said to be *allowed* or *active* in the infrared spectrum, otherwise they are said to be *forbidden* or *inactive*. The frequencies of the absorption bands are proportional to the energy difference between the vibrational ground and excited states.

2.3. Raman spectroscopy

If a light quantum $h\nu_0$ hits a molecule, an elastic scattering process, i.e., *Rayleigh scattering* of quanta with the same energy $h\nu_0$, has the highest probability. The inelastic process, during which vibrational energy is exchanged, has a much lower probability and is called *Raman scattering*. In this case quanta of the energy $h\nu_0 \mp h\nu_s$ are emitted. At ambient temperatures most molecules are in their vibrational ground state. According to Boltzmann's law, a much smaller number is in a vibrationally excited state. Therefore, the Raman process, which transfers vibrational energy to the molecule and leaves a quantum of lower energy ($h\nu_0 - h\nu_s$) has a higher probability than the reverse process. Raman lines are referred to as Stokes and anti-Stokes lines. Stokes lines are caused by quanta of lower energy, since their intensities are higher than those of anti-Stokes lines, only these lines are usually recorded as Raman spectrum.

When a molecule is exposed to an electric field, electrons and nuclei are forced to move in opposite directions. Thus, a dipole moment, which is proportional to the electric field strength and to the molecular polarizability α , is induced. A molecular vibration can be observed in the Raman spectrum only if there is a modulation of the molecular polarizability by the vibration,

$$\left(\frac{\partial \alpha}{\partial q} \right)_0 \neq 0. \quad (2.13)$$

If the condition (Eq. 2.13) is fulfilled, then the vibrations are said to be *allowed* or *active* in the Raman spectrum, otherwise they are said to be *forbidden* or *inactive*.

The intensity of the signal delivered by the detector of a spectrometer analysing a given Raman line at the wavelength λ can be expressed by:²⁸

$$S \propto I_L \cdot \sigma_\lambda \cdot N_m \cdot \Omega \cdot T_\lambda \cdot s_\lambda \quad (2.14)$$

where I_L is the laser irradiance at the sample ($\text{W}\cdot\text{cm}^{-2}$), σ_λ is the differential cross-section for the Raman line analysed ($\text{cm}^2\cdot\text{sterad}^{-1}\cdot\text{molecule}^{-1}$), N_m is the number of molecules in the probed volume V_p . Ω is the solid angle of collection of the Raman light, and T_λ and s_λ are the throughput of the instrument and the sensitivity of the detector at λ , respectively. When a small volume of matter has to be examined, only a few parameters can be modified to compensate for the large reduction in the number of molecules N_m in the probed volume, V_p , namely I_L and Ω . The use of microscope objectives²⁰ for both illuminating the sample and collecting the Raman light represents the best way to decrease V_p , while increasing Ω and I_L . Microscope objectives with a high numerical aperture are able to focus the laser beam into a very small volume and to collect the light scattered by this volume under a wide angle.

2.3.1. Confocal micro-Raman spectroscopy

A confocal setup means that the sample is illuminated with a diffraction limited spot and the illuminating spot is imaged on an ideally point-like detector. Practically, the point-like detector is realized with an adjustable pinhole in front of the real detector (or

spectrograph entrance slit in our case). By using a confocal optical system a separation of the signal from each layer of a layered sample, or an isolation of the signal from an inclusion against the signal coming from the surrounding medium can be achieved.²⁹⁻³²

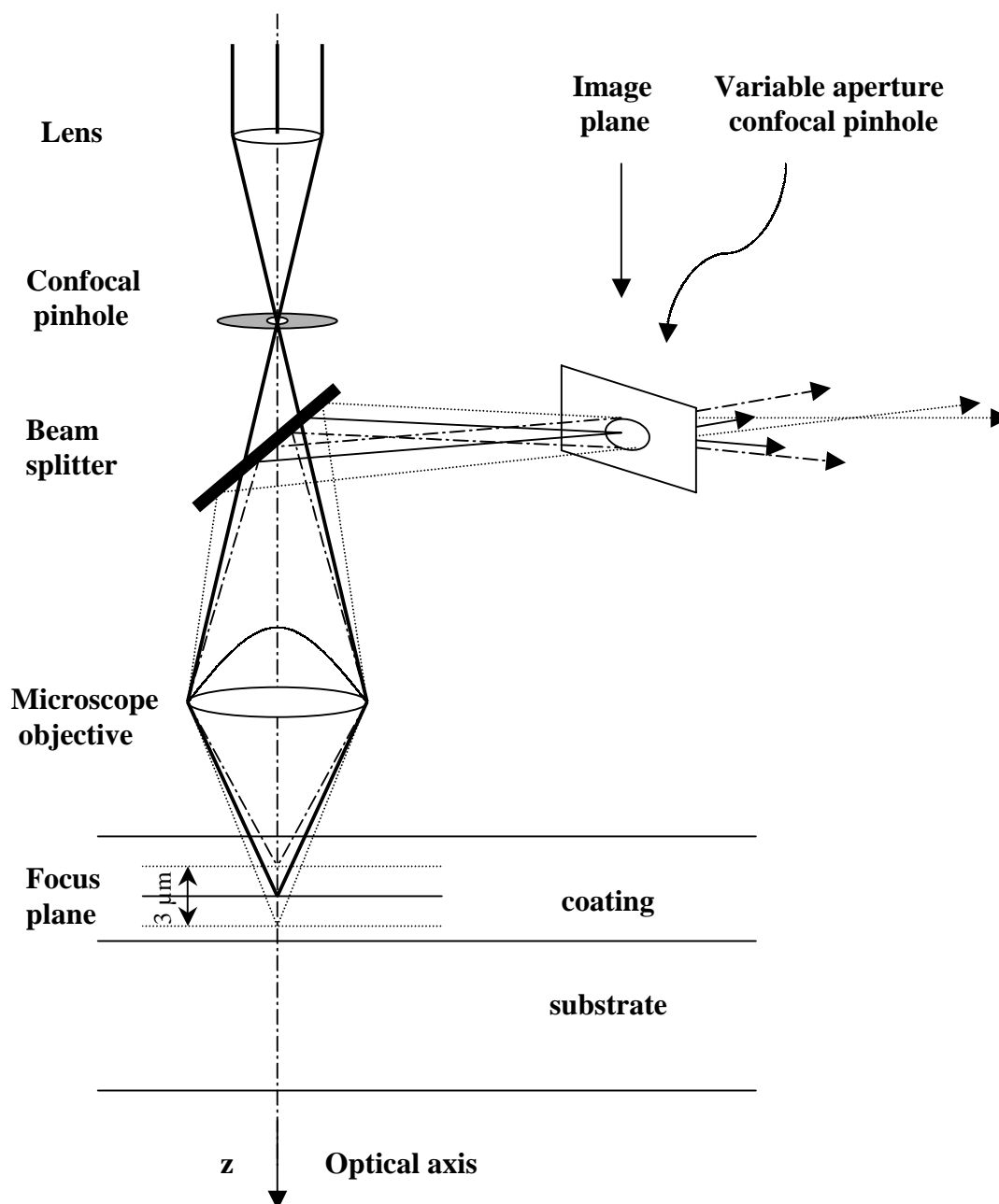


Fig. 2.1. Scheme which presents the principle of the confocal microscopy and the depth discrimination, obtained when a coated sample is employed in confocal micro-Raman measurements.

A schematic diagram of the illuminating and collecting optics of a confocal micro-Raman setup, which illustrates the confocal axial discrimination, is depicted in Fig. 2.1. It can be seen from this figure that a real confocal configuration requires a very accurate optical alignment and a high degree of stability and reproducibility of the mechanical and optical alignment.

The main advantages of confocal microscopy may be summarized as follows:

- (i) Dramatic improvement of the depth discrimination which allows an “optical sectioning” of transparent specimens. In order to correctly evaluate the depth discrimination a careful analysis of the spatial distribution of local irradiance in the focal volume close to the laser beam’s secondary waist, combined with the calculation of light collection by a wide aperture objective are necessary.
- (ii) Improvement of lateral resolution. The intensity point spread function, otherwise limited to the Airy diffraction disc dimension, can be reduced theoretically by a factor of 0.7 but at the expense of very low throughput, since it requires pinhole diaphragms of small diameter.
- (iii) Extremely low light level of Raman signals compared to the intensity of the excitation radiation which is retro-scattered by reflection at the interfaces or that of the diffuse scattering by the specimen (typically 10^{-3} to 10^{-12}).
- (iv) The possibility of spectral analysis in a relatively narrow domain adjacent to the intense parent line at the laser frequency (Rayleigh line) (typically 100 to 3500 cm^{-1} for routine vibrational spectroscopy).

2.3.2. Resonance Raman spectroscopy

Resonance occurs in Raman spectroscopy when the photon energy of the exciting laser beam is approximately equal to the energy of an electric dipole allowed transition of the material under investigation. Two types of resonance Raman effect can be identified: the pre-resonance Raman effect and the rigorous resonance Raman effect. The first effect is observed when the exciting radiation frequency comes within the high or low

frequency wings but not under the observable vibrational structure of the electronic absorption band involved in the Raman scattering process. When the exciting radiation frequency falls within the observable vibrational structure, then the rigorous resonance Raman effect is observed. The intensities of Raman bands associated with totally symmetric vibrational modes, which are strongly coupled to the electronic excited state, may be enhanced by as much as a factor of 10^6 . In principle, no special Raman instrumentation is needed to perform resonance Raman spectroscopy because resonance Raman spectra can be obtained with conventional Raman spectrometers, if the suitable excitation wavelength is applied. Many important studies³³⁻⁴⁷ dealt with the development of resonance Raman spectroscopy in a wide application range.

2.3.3. Fourier Transform Raman spectroscopy

The first Fourier transform (FT) Raman spectrum was reported in 1984. Weber et al. measured the Raman spectra of gases using an argon laser and the interferometer at the Kitt observatory.^{48, 50} Chase and Rabolt⁵⁰ note that Chantry et al.⁵¹, suggested already 1964 the use of infrared radiation in combination with an interferometer as a detector to record Raman spectra. They demonstrate the feasibility of the technique, with the important remark that the long excitation wavelength would avoid the excitation of fluorescence. Following a discussion between B. Chase and T. Hirschfeld, the existing Fourier transform infrared instruments were modified⁵² to measure Raman spectra excited with krypton and Nd:YAG lasers (emitting at 647.1 nm and 1.064 μm).

The central component of a FT spectrometer is a Michelson interferometer (Fig. 2.2). FT spectrometers operate by splitting an incoming beam into two parts, applying a differential phase shift, then recombining the beams. While varying the phase shift an interference pattern known as an interferogram is obtained as a function of the phase shift. The phase shift is produced by translating a mirror along the beams, thus producing an optical path difference between the fixed and movable mirror. The resolution is determined by the maximum displacement of the translating mirror. From the interferogram the spectrum as a function of wavelength is calculated by applying a Fourier transformation (FT), which gives the instrument its name.

For a continuous function of one variable $f(t)$, the Fourier transform $F(\nu)$ will be defined as:

$$F(\nu) = \int_{-\infty}^{+\infty} f(t) \cdot e^{-2\pi i \nu t} dt, \quad (2.15)$$

and the inverse transform as:

$$f(t) = \int_{-\infty}^{+\infty} F(\nu) e^{2\pi i \nu t} d\nu. \quad (2.16)$$

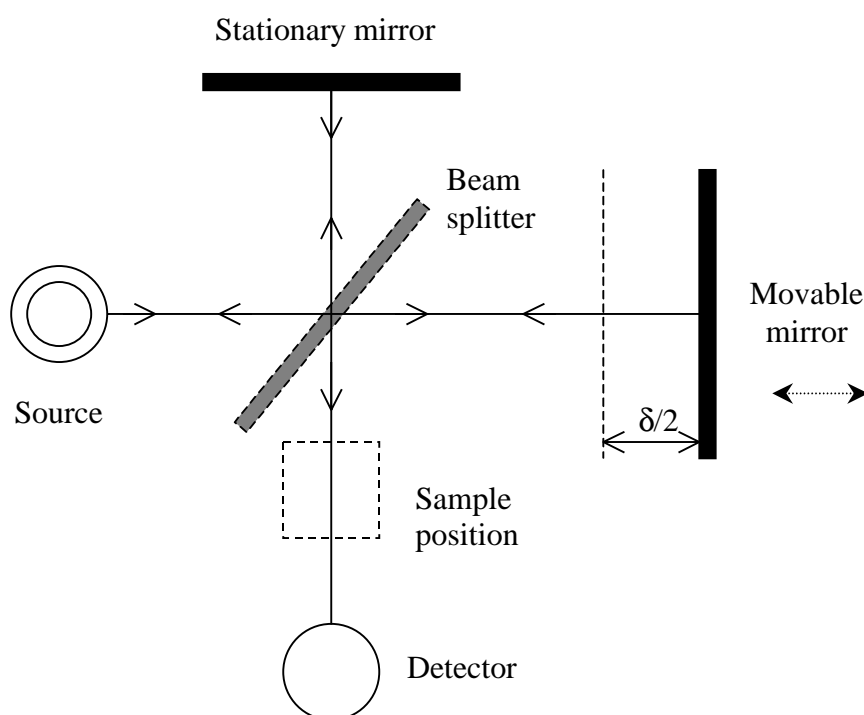


Fig. 2.2. Scheme which illustrates the optical principle of the Michelson interferometer.

The relative advantages and disadvantages of an FT-Raman equipment versus a dispersive equipment may be summarised as follows:

Advantages:

- (i) Multiplex advantage (Fellgett's advantage): an interferometer provides information about the entire spectral range during the entire period of the measurement, whereas a dispersive spectrometer provides information only

about the narrow wavenumber region which falls within the exit slit of the monochromator at any given time.

- (ii) Throughput advantage (Jacquinot's advantage): the interferometer can operate with a large circular aperture, and using large solid angles at the source and at the detector, whereas a dispersive spectrometer requires long, narrow slits to achieve adequate resolution.
- (iii) Connes advantage: the wavelength accuracy and precision is extremely good because of the use of a HeNe laser to reference the interferometer.

Disadvantages:

- (i) Multiplex disadvantage, which occurs because the signal is detected at all wavelength simultaneously so the shot noise from the entire spectrum is spread into every spectral element.
- (ii) FT-Raman spectroscopy is normally a single beam technique, thus comparison of sample and reference has always to be performed by computer subtraction.

3

Experimental

3.1. Samples preparation

Precursors for the preparation of the inorganic-organic hybrid polymer (ORMOCER^{®*}) coatings of 6.2 and 20.2 μm ($\pm 0.5 \mu\text{m}$) thickness were 3-glycidoxypropyltrimethoxysilane (GLYMO), purchased from ABCR, and 3-(triethoxysilyl)propyl succinic anhydride (TESSA), purchased from Wacker Chemie, with purities of 98 % and 95 %, respectively. 100 mmoles of GLYMO containing a catalytic amount of an amine were hydrolyzed with 150 mmoles of distilled water under vigorous stirring. After the hydrolysis was complete - determined by FT-Raman spectroscopy⁵³ – subsequently 10 g

* Trademark of Fraunhofer-Gesellschaft zur Förderung der angewandten Forschung e.V., Munich, Germany

of 1-propanol was added, the sol was cooled to 10 °C, and 50 mmoles of TESSA were dropwise added. After stirring for 1 hour 20 wt.% 1-propanol was added and the sol has been placed in a dip-coating reservoir. A bisphenol-A polycarbonate sheet of the dimension 100*35*2 mm³ was subsequently rinsed with distilled water and ethanol, dried with compressed air, and dip-coated four times with a withdrawing speed of 100 mm/min. After every dipping process the samples were air-dried for 2 minutes in each case. Thermal curing was performed at 130 °C for 30 minutes. The coating thickness was determined by means of an UBM profilometer.

The PDMS membranes have been prepared by an addition reaction of linear PDMS with terminal vinyl groups (Silopren[®] U1 and U10; Bayer Silicons) and of low molecular PDMS carrying Si-H functional groups (Silopren[®] U crosslinking agent 430; Bayer Silicons). For this reaction a platinum catalyst has been used (Silopren[®] U catalyst Pt/S; Bayer Silicons). In order to achieve better mechanical properties tetramethyl-tetravinyl-cyclotetrasiloxan (Bayer Silicons) was added. The different components were mixed together in a beaker glass and stirred gently with a glass rod. Then the polymer mixture was evacuated in an exsiccator in order to eliminate air-bubbles trapped in this mixture.⁵⁴ The membrane was made by means of an automatic ductor coating device K101 (Coefeld) and a coating ductor 300 on a glass plate which was heated to allow for cross-linking (30 min. by 80 °C). The film thickness was determined with a MiniTest 1100 (ElektroPhysik). β -carotene and DMSO have been used as purchased (Aldrich).

Glass samples belonging to 99.5% $[xB_2O_3(1-x)Bi_2O_3]0.5\%CuO$ with $0.07 \leq x \leq 0.625$, 95% $[xB_2O_3(1-x)Bi_2O_3]5\%Fe_2O_3$ with $0.07 \leq x \leq 0.90$ and 99.5% $[xB_2O_3(1-x)Bi_2O_3]0.5\%Fe_2O_3$ with $x = 0.20$ were prepared using as starting materials H_3BO_3 , $Bi(NO_3)_3 \cdot 5H_2O$, CuO and Fe_2O_3 of reagent purity grade. The mixtures corresponding to the desired compositions were melted in air, in sintered corundum crucibles, in an electric furnace at 1100 °C and maintained for 10 minutes at this temperature. The melts were quickly cooled at room temperature by pouring and pressing between two stainless steel plates.⁵⁵⁻⁵⁷ The glass samples were subjected to partial crystallization by heat treat-

ment applied at 575 °C for 10 hours.

3.2. Sample measurements

The micro-Raman measurements of all samples have been performed on a Lab Ram Raman spectrometer (Jobin Yvon) equipped with a confocal aperture.

For confocal measurements the coated samples and the membrane were mounted on an x, y motorized stage, the z-displacement was controlled by a piezo-transducer on the objective. The confocal pinhole diameter was 200 μm and the slit width was 40 μm . The depth resolution has been measured by focusing the laser beam just above a silicon wafer, and measuring the 520.7 cm^{-1} band as the wafer is raised vertically through the beam focus. The full width at half maximum (FWHM) of the silicon signal gives an indicator of the depth of the laser focus *in air*. Under these conditions, the confocal depth of the focus, assessed by z-scanning a silicon wafer, was measured to be $\sim 2 \mu\text{m}$ FWHM. The exact depth resolution in a particular measurement is affected by the sample/air interface.⁵⁸ The estimation of the depth resolution for a particular confocal measurement can be achieved by measuring the intensity response, from zero to maximum intensity, as the focal point is scanned through the surface of the investigated sample. For all samples employed in confocal measurements we obtained a step profile with a FWHM of $\sim 3 \mu\text{m}$. The spectral resolution was about 2 cm^{-1} .

In recording the confocal micro-Raman measurements of the coated samples a He-Ne laser excitation (633 nm line), a 100 \times 0.9 NA microscope objective, and a laser power of $\sim 3 \text{ mW}$ incident on the sample have been used, while the spectra recorded during the diffusion through the PDMS membrane have been obtained by applying the 514 nm line of an argon ion laser with a power of $\sim 105 \text{ mW}$ incident on the sample and using a 100 \times 0.8 microscope objective. A small square piece of a $\sim 200 \mu\text{m}$ thick PDMS membrane was centred above the small hole of the circular sample holder (see Fig. 3.1). The membrane was fixed by a plane washer (height 1.2 mm; diameter 1.5 cm) which was used as the donor cell, filled with 0.4 ml of the sample liquid and sealed by a thin

glass lid to avoid evaporation of the sample liquid.

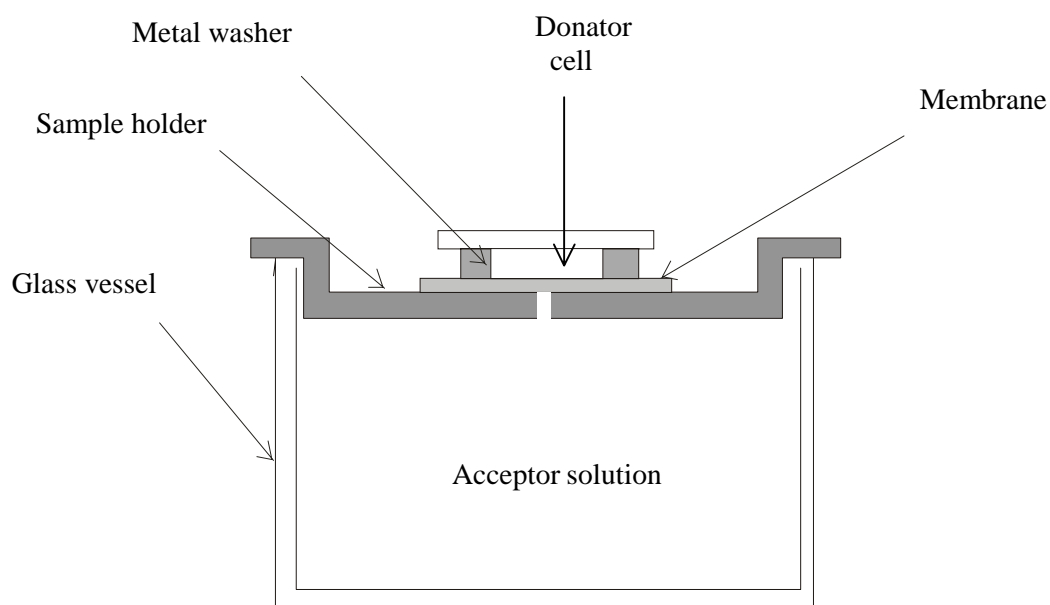


Fig. 3.1. Schematic sketch of the sample cell.

In order to determine the distribution of β -carotene within a saturated PDMS membrane by means of Raman measurements the above described donator cell has been placed on top of a small Petri dish filled with DMSO to guarantee constant sink conditions. After the adjustment of a dynamic equilibrium which takes 20 h, Raman spectra have been recorded at depths of 40, 60, 80, 100, 120, 140 and 160 μm inside the membrane. The kinetic measurements were done with an empty Petri dish underneath the donator cell over a period of 60 - 180 min. In order to determine the diffusion properties of β -carotene across a PDMS membrane, Raman spectra have been recorded every 10 s.

Raman measurements of the $99.5\%[\text{x}\text{B}_2\text{O}_3(1-\text{x})\text{Bi}_2\text{O}_3]0.5\%\text{CuO}$ samples were performed by using a NIR optimised Olympus LMPlan Fl 50 microscope objective, a 950 lines/mm grating and an external SDL-8530 cw diode laser with an emission wavelength of 785 nm, while for the micro-Raman measurements of $95\%[\text{x}\text{B}_2\text{O}_3(1-\text{x})\text{Bi}_2\text{O}_3]5\%\text{Fe}_2\text{O}_3$ glasses an Olympus LMPlan Fl 50 microscope objective, an 1800 lines/mm grating and an external laser with an emission wavelength of 514 nm have been used. In the recording of the micro-Raman spectra a power of 100 mW incident on

the sample has been employed. The spectral resolution was about 4 cm^{-1} .

FT-Raman spectra of $99.5\%[\text{xB}_2\text{O}_3(1-\text{x})\text{Bi}_2\text{O}_3]0.5\%\text{Fe}_2\text{O}_3$ glasses, presented only for comparison purposes, were recorded using a BRUKER IFS 120HR spectrometer equipped with a FRA 106 Raman module. The spectral resolution was 2 cm^{-1} . Radiation of 1064 nm from a Nd:YAG laser with an output power of 800 mW was employed for excitation. A Ge detector cooled with liquid nitrogen was used.

For infrared measurements the glasses and heat-treated samples were powderized and mixed with KBr in order to obtain thin pellets with a thickness of about 0.3 mm. The infrared spectra were recorded with a Bruker IFS 25 spectrometer; the spectral resolution was 2 cm^{-1} .

X-ray diffraction measurements were performed on as prepared samples, before and after thermal treatment, with a standard DRON-3M powder diffractometer by using Cu K_α radiation.^{55,56}

4

Modeling and measuring the effect of refraction and diffraction on the focus lengthening on confocal micro-Raman experiments

4.1. Introduction

Raman microscopy offers a unique combination of spatial resolution and chemical/physical characterization. Although its spatial resolution is worse than that of electron microscopy, it enables the measurement of a host of chemical and physical properties, including chemical composition, molecular orientation, conformation, crystallinity, strain, temperature, etc.. No other microprobe technique offers such a com-

bination of spatial resolution and information content. Simply focusing the laser beam to a small spot does not provide a good spatial resolution, since the turbidity spreads the laser intensity over a large sample volume, and the resultant Raman signal source is therefore not being “tightly” located in space. Many authors have pointed out that this effect can be suppressed by placing a confocal aperture at a back focal image plane in order to block the light that originates from the out diffraction-limited laser focal volume⁵⁹⁻⁶³, thus improving both the lateral as well as the axial resolution. Mostly a physical aperture such as an adjustable pinhole has been used, but the same result can be obtained by using a charge coupled device (CCD) detector as an “electronic” aperture.⁶³ The second approach considers the entrance slit as one dimension of the aperture and pixel binning of the CCD as the orthogonal aperture axis. However, the confocal aperture is designed to collect the Raman radiation that originates only from the laser focal volume within a diffraction-limit. The dimensions of the focal region depend on the numerical aperture (NA) of the focusing lens and the degree to which it is filled by the laser beam. By using a microscope objective with a high NA filled by the laser beam, one obtains a focal “tube” with a waist diameter of $\sim 1.22 \lambda/NA$ and a depth of $\sim 4 \lambda/(NA)^2$. The lateral diameter can be determined by scanning the laser spot over a material with a very sharp edge or feature, and measuring the response.⁶⁰ The focal depth can be measured by focusing the laser beam just above a silicon wafer, and measuring the 520 cm^{-1} band intensity as the wafer is raised vertically though the beam focus. The full width at half maximum (FWHM) of the silicon signal gives an indication of the depth of the laser focus *in air*. Its shape and volume will, however, be distorted if the beam is focused into a material of different refractive index. Several authors⁶³⁻⁶⁷ have already tried to obtain information from thin layers considering the allowed depth discrimination by confocal micro-Raman spectroscopy.

Depth-profiling analysis of two coated samples (6.2 and 20.2 μm in thickness), which in this case represent the confocal Raman signal given by a substrate band as a function of the depth, which is considered the center of the focus position into the sample, are presented in Fig. 4.1. Taking into account that both coatings and substrates have the same chemical composition but different thickness, a lack of understanding of the broa-

dening of the coating/substrate boundary still remains. In order to solve this problem we tried to characterize the dimensions of the focus inside the coating, substrate, and at the coating/substrate interface by means of a sol-gel hybrid polymer coating applied to a polycarbonate substrate by considering two of the most important effects present when confocal Raman measurements are employed, refraction and diffraction. It should be noted that the coating and the substrate have approximately the same refractive index ($n_1 = 1.5$).

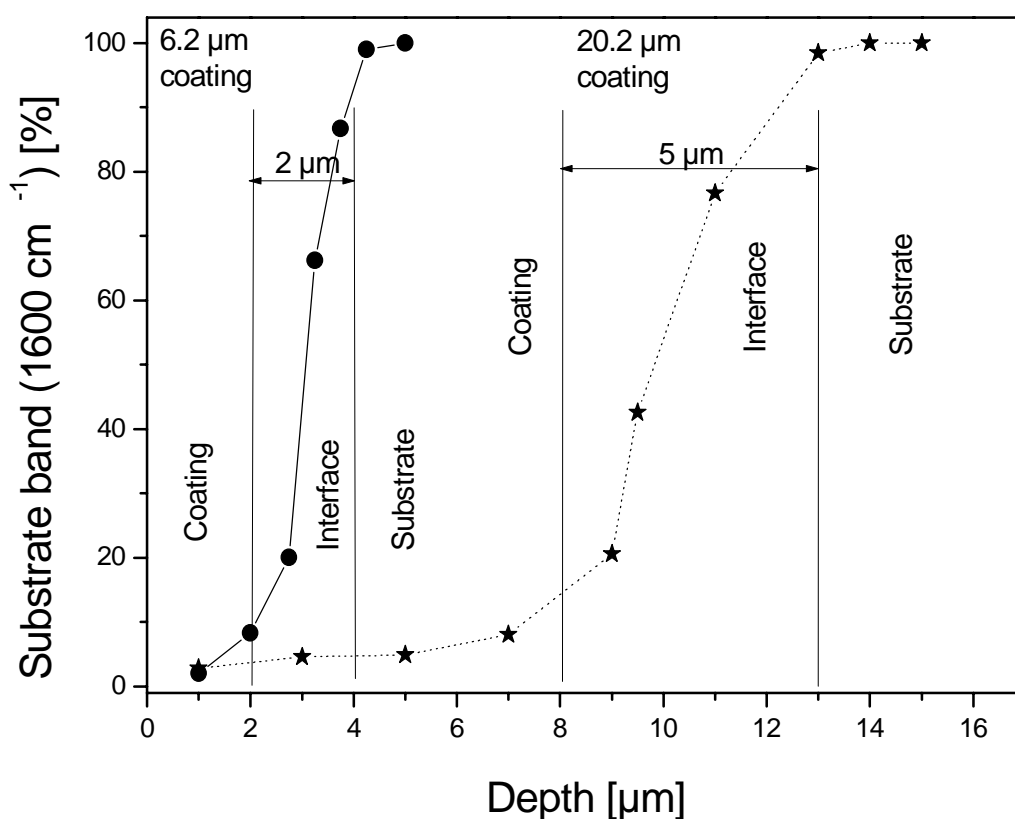


Fig. 4.1. Depth-profiling analysis of two coated samples which have the same chemical compositions but different thickness. Note how the coating/substrate boundary is broadened significantly for a thicker coating.

4.2. The effect of refraction on the depth resolution of confocal Raman microscopy

4.2.1 Ray tracing analysis

In the past it has been assumed that the diffraction limited depth of focus of the laser beam, as measured *in air*, is indicative of the depth resolution attainable inside the sample. However, there were few authors who considered the refraction aberration effect in more detail. Rosasco⁵⁹ discussed the problem and predicted the magnitude of such an effect for an ellipsoidal collection mirror with an uniform laser illumination, while Delhaye et al.²⁰ gave an expression for the maximum depth of the focus. They also pointed out that if a “dry” objective is used to analyse samples either beneath a cover slip or embedded deep in a matrix, the confocal depth resolution is severely degraded. However, none of them compared theoretical expression with experimental data. A theoretical approach^{58,68} considering the refraction effect has been applied in order to characterize the dimensions of the focus inside the coating, the substrate as well as at the coating/substrate interface. The starting point of this model is the assumption that the effects of diffraction are small compared with the influence of refraction. Therefore, only refraction-induced aberrations are considered and modelled by ray tracing analysis. In Fig. 4.2. the relevant parameters are defined. The microscope objective with a numerical aperture (NA) of $\sin \alpha_{\max}$ and a working distance f is placed in a medium of refractive index n_2 (assumed to be 1 for air). The final lens of the microscope objective is assumed to have a limiting aperture radius of r_{\max} . The last two parameters together with the numerical aperture NA are related through the equation:

$$r_{\max} = \frac{f \cdot NA}{(1 - NA^2)^{1/2}}. \quad (4.1)$$

When focusing through a material boundary, a ray originating at a radius r measured from the centre of the microscope objective is brought to a focus at a point \mathbf{P}^l , which lies a distance z_k^l below the sample/air interface.

If the material has a refractive index of $n_1 = 1$, the same ray would be focused in **P**, at a distance Δ below the interface.

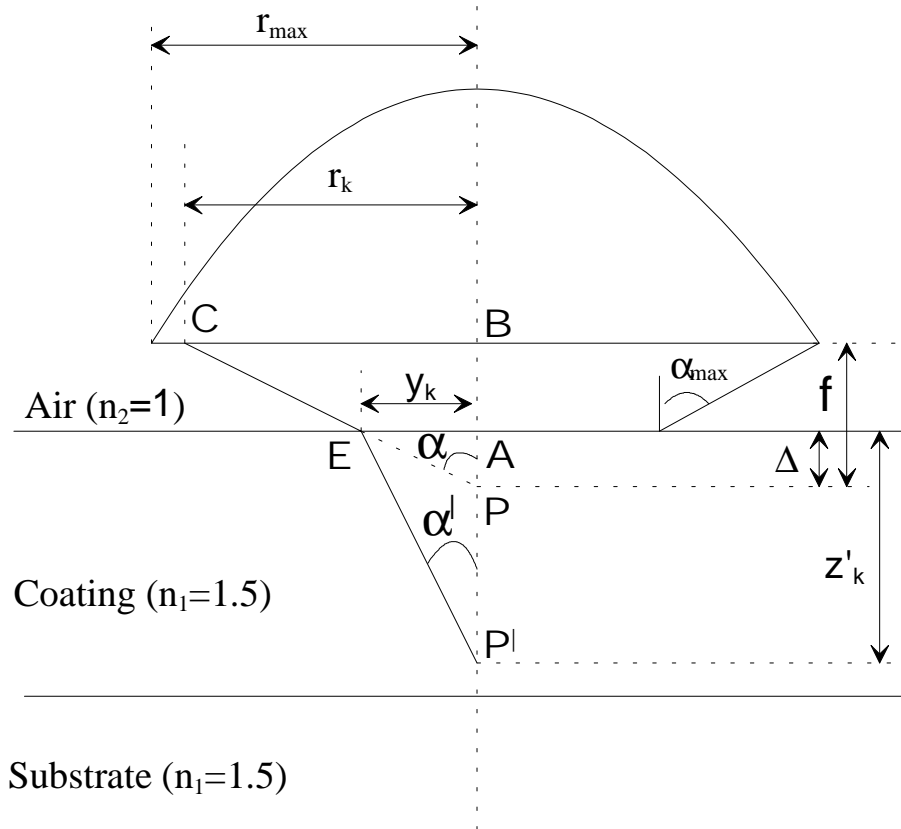


Fig. 4.2. Scheme that presents the ray tracing in a medium when only the refraction effect is considered. For convenience the objective lens is depicted as a hemisphere; the exact shape is not important. In the absence of refraction, all rays are focused at a point **P**, refraction causes rays to be focused deeper into the sample (**P'**). All terms are defined in text.

Note that Δ is actually the distance moved by the sample when shifting the focus from the sample surface to point the **P**. Δ is called the “apparent” focal point, since it is the vertical distance moved according to the scale on the microscope stage.

The purpose of this analysis was to calculate the true focal position z'_k and the intensity

distribution inside the coating, within the substrate as well as at the coating/substrate interface, as a function of $n (= n_1/n_2)$, NA , and Δ , and to relate the position and the depth of focus to Δ . This approach enables an estimation of the true illuminated region when focusing a nominal distance Δ into a sample. It was assumed that all rays are focused along the z -axis, the orthogonal spreading has been neglected.

From Fig. 4.2, considering the k -th ray (i.e., one originating from radius r_k), the $\sin \alpha$ and $\cos \alpha$ can be expressed, from the triangle **PCB**, as follows:

$$\sin \alpha = \frac{r_k}{\sqrt{r_k^2 + f^2}}, \quad \cos \alpha = \sqrt{1 - \sin^2 \alpha}. \quad (4.2)$$

By using Snell's law:

$$\sin \alpha^l = \frac{\sin \alpha}{n}, \quad (4.3)$$

Eq. 4.2 becomes:

$$\sin \alpha^l = \frac{r_k}{n \cdot \sqrt{r_k^2 + f^2}}, \quad \cos \alpha^l = \sqrt{1 - \frac{\sin^2 \alpha}{n^2}}. \quad (4.4)$$

By applying the tangent function for the triangles **P^lEA** and **PEA** we get:

$$z_k^l = \frac{y_k}{\tan \alpha^l} = \frac{\Delta \cdot \tan \alpha}{\tan \alpha^l}. \quad (4.5)$$

Eqs. 4.3-4.5 lead to a simple expression (Eq. 4.6) for the true point of the focus z_k^l within a medium for any ray, as a function of the apparent focal point Δ , the lens working distance f , and the refractive index n :

$$z_k^l = \frac{\Delta}{f} \left[n^2 \cdot (r_k^2 + f^2) - r_k^2 \right]^{1/2}. \quad (4.6)$$

With the use of Eq. 4.1 to substitute for f , Eq. 4.6 can be rewritten as follows:

$$z_m^l = \Delta \left[\frac{r_k^2 \cdot NA^2 \cdot (n^2 - 1)}{r_{\max}^2 \cdot (1 - NA^2)} + n^2 \right]^{1/2},$$

$$z_m^l = \Delta \left[m^2 \cdot \frac{NA^2 \cdot (n^2 - 1)}{(1 - NA^2)} + n^2 \right]^{1/2}, \quad (4.7)$$

where the parameter m is defined⁵⁸ as the normalised radius ($m = r/r_{\max}$), i.e., the fractional distance across the last lens of the microscope objective. When $m = 1$ we have a marginal ray, i.e., one with the highest possible angle of incidence, whereas $m = 0$ implies a ray normal to the sample surface. Fig. 4.3 illustrates the variation of z_m^l with m for four nominal focal points ($\Delta = 2, 5, 8$ and $12 \mu\text{m}$), assuming a 0.9 NA objective.

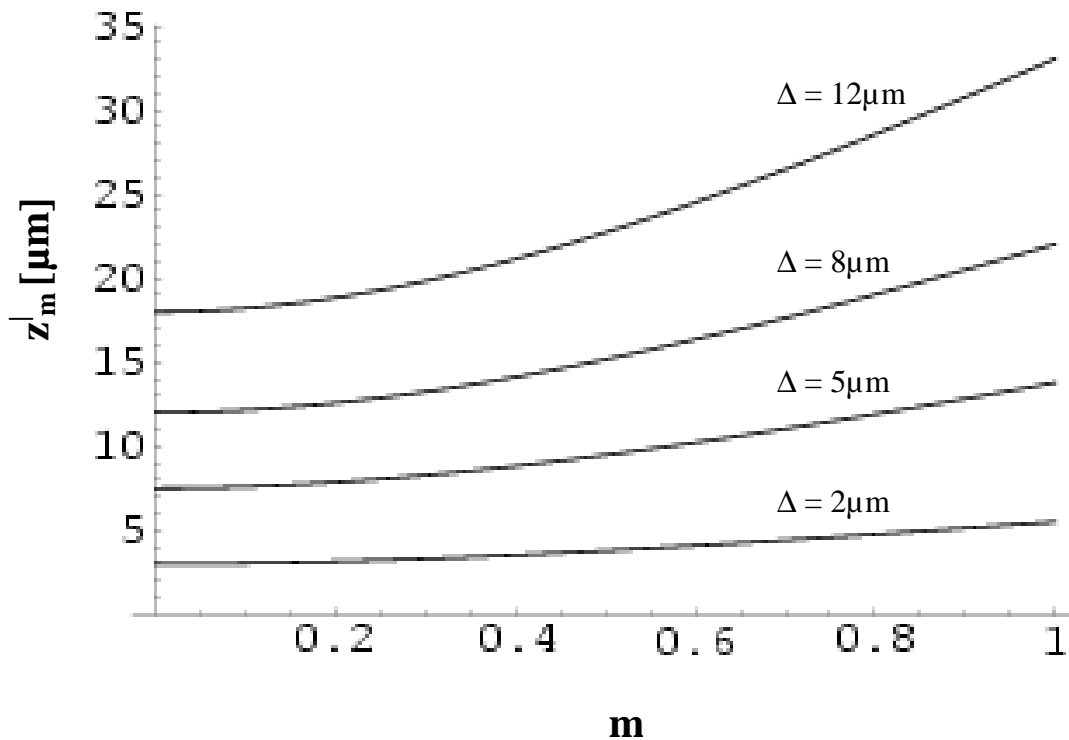


Fig. 4.3. Distance of the focal point z_m^l below an air interface, as a function of the fractional distance across the objective m . Note how increasing of Δ causes rays to be focused deeper in the sample. Rays originating near the maximum objective aperture ($m = 1$) are also focused deeper.

From Eq. 4.7 and Fig. 4.3 several considerations can be drawn:

- (i) If the microscope objective is grossly underfilled ($m \approx 0$), Eq. 4.7 reduces to $z_m^l = \Delta \cdot n$, and the true focal point is shifted by a factor n relative to the apparent focus. This is the minimum deviation between the apparent and the

true focus that can be obtained with a dry objective; even so, for a nominal focus 10 μm below the sample surface, the true focus, which now becomes a point, would actually be 15 μm . By using an immersion objective the refractive indices will be matched ($n \approx 1$), the aberrations, which appear due to the refraction effect, will be minimised, the apparent and actual focal point arriving approximately in the same point **P**.

- (ii) The maximum depth of a focal point in the sample for a given Δ is obtained, by using Eq. 4.7 for the marginal ray ($m = 1$).

Taking into account the above mentioned considerations, which are derived from a closely analysis of Eq. 4.7 and Fig. 4.3, a simple expression for the range of laser focal positions within the sample (i.e., the depth of focus, *d.o.f.*) can be obtained:

$$d.o.f. = z_{m=1}^l - z_{m=0}^l = \Delta \cdot \left\{ \left[\frac{NA^2 \cdot (n^2 - 1)}{(1 - NA^2)} + n^2 \right]^{1/2} - n \right\}. \quad (4.8)$$

From this equation, one important result can be highlighted, namely that the depth of focus increases linearly with the apparent focal point Δ , and is dependent on the refractive index of the coating and substrate n . It should be noted that not only the point of focus is changing with Δ , but also the depth of the focus.

The effect of the NA on the depth of the focus of the laser beam, when the diffraction effect is neglected, can be analysed from a plot of the ratio $d.o.f./\Delta$ as a function of NA as shown in Fig. 4.4. It can be seen that the relative depth of focus increases very rapidly when microscope objectives that exceed $0.9 NA$ are employed, suggesting the use of microscope objectives with small NA s. However, when objectives with small NA s are employed, the diffraction effect becomes dominant, causing a focus lengthening, due to the dependency of the length of the focus of the numerical aperture ($\sim 1/NA^2$).

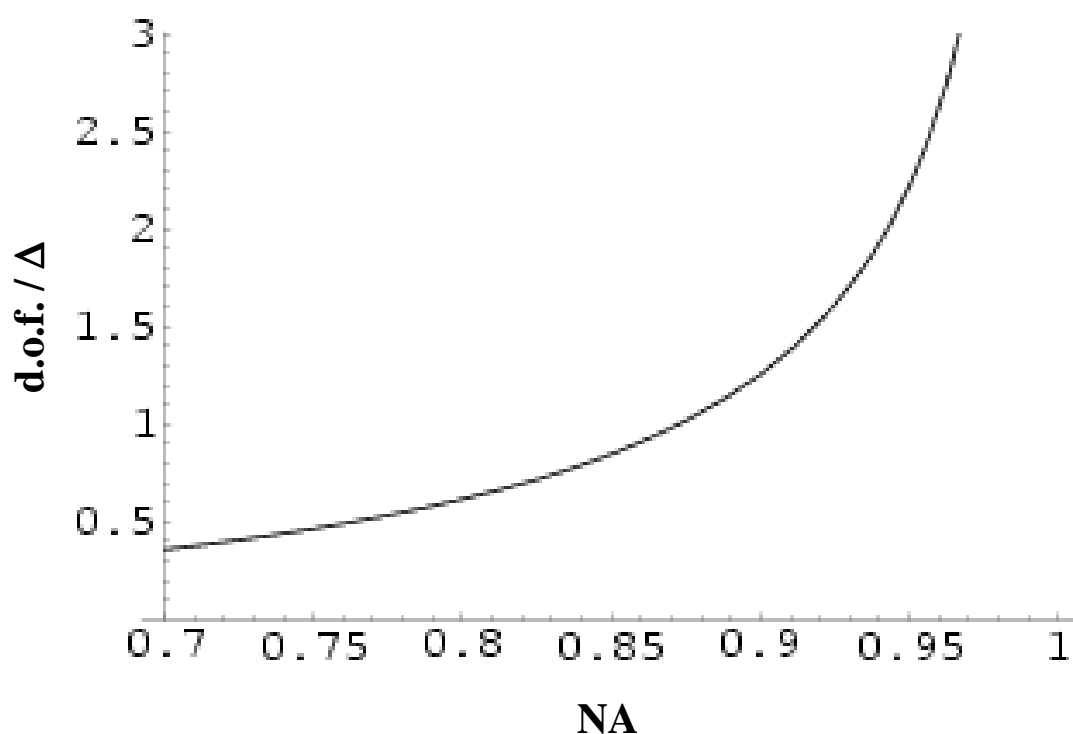


Fig. 4.4. Ratio of depth of focus ($d.o.f.$)/ Δ as a function of NA neglecting the diffraction effect. Note that for high NA and large Δ the $d.o.f.$ becomes very large. However, at low NA and small Δ , the diffraction effect will dominate resulting in a lengthening of the depth of focus.

The overall result derived from the analysis of Fig. 4.4 is that it is not possible to monotonically improve the depth resolution by using lower NA microscope objectives, because at some points the diffraction effect will dominate and the depth of focus will begin to rise again. These points depend upon the value of Δ , since the refraction effect is becoming dominant for high Δ . Taking all these considerations into account we decided to perform all confocal micro-Raman measurements presented in this section with a microscope objective with 0.9 NA that represents the optimum according to Fig. 4.4.

4.2.2. Laser intensity distribution

The laser intensity distribution in the sample is strongly influenced by the laser intensity distribution in the microscope objective. Assuming that the laser beam has a Gaussian intensity profile, one normally tries to fill the entrance pupil of the microscope objective so that the beam is apertured at the $1/e^2$ intensity points. This procedure results in an Airy pattern at the focal plane and produces a focal “tube” with a waist diameter of $\approx 1.22 \lambda/NA$ and a depth of focus of $\approx 4 \cdot \lambda/(NA)^2$. In this case, the microscope objective will be only slightly overfilled, the intensity distribution being expressed as a truncated Gaussian:

$$I(r) = I_0 \cdot \exp\left(\frac{-2 \cdot r^2}{r_{\max}^2}\right), \quad (4.9)$$

where the waist radius containing $\sim 86\%$ of the total beam intensity matches the limiting objective radius r_{\max} . In terms of the normalized radius m , this distribution becomes:

$$I(m) = I_0 \cdot \exp\left(\frac{-2 \cdot m^2}{\phi^2}\right), \quad (4.10)$$

where ϕ represents the “fill factor” of the microscope objective. Keeping in mind that the integrated intensity of all rays originating from points on the microscope objective is proportional to the normalized radius m , the laser intensity throughout the focal region could be calculated. Thus, by assuming a circular symmetry, if the radial intensity distribution is $I(m)$, the overall intensity of all rays originating from a radius m is proportional to $m \cdot I(m)$.

In Fig. 4.5 the intensity distribution $m \cdot I(m)$ inside the sample as a function of focal position z_m^{\perp} is plotted for five different values of Δ (2.5, 5, 8, 10 and 12 μm , respectively) assuming a 0.9 NA objective, $I_0 = 1$, and $\phi = 1$. These plots are normalized to a constant integrated intensity in order to maintain the same intensity of the laser in a focal volume for different given Δ values.

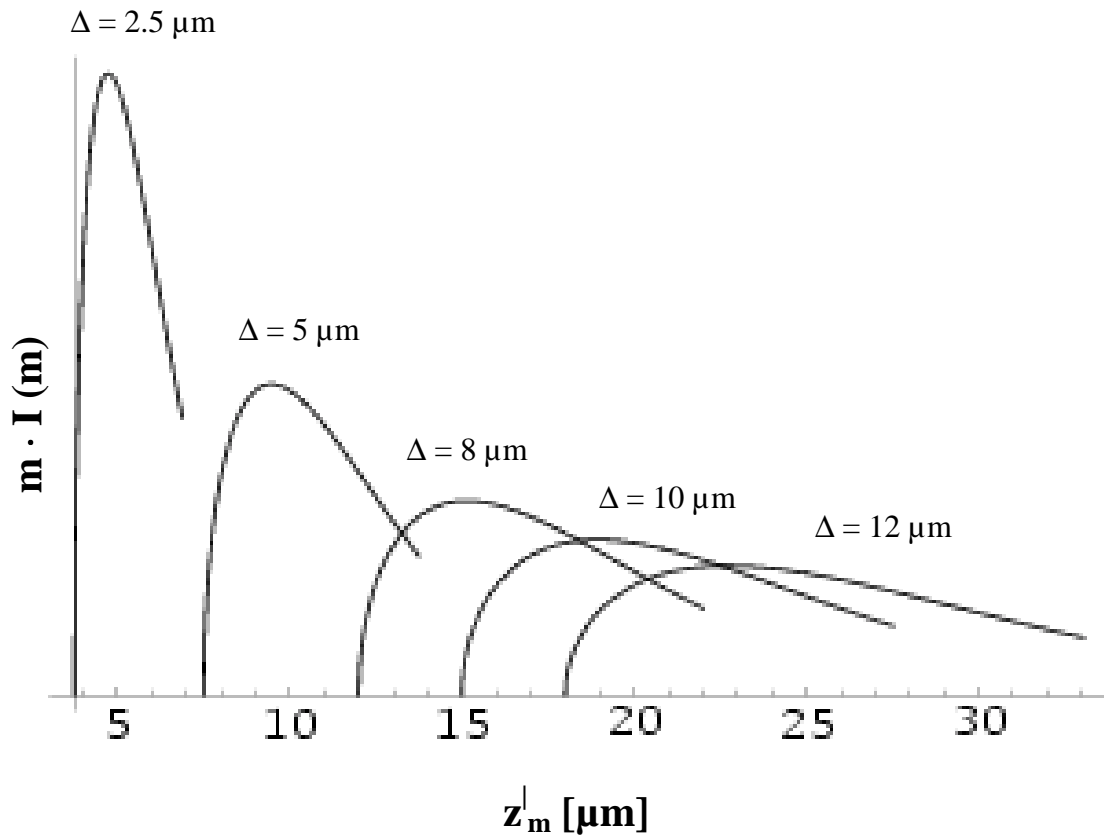


Fig. 4.5. Laser intensity $m \cdot I(m)$ vs. focal position in sample z_m^l as a function of apparent focal point Δ . Note that the integrated intensity has been normalized to a constant area, for all Δ values.

From Eq. 4.8 and Fig. 4.5 two important remarks can be concluded:

- (i) For $\Delta = 2.5 \mu\text{m}$, the depth of focus is comparable to the diffraction limit ($\sim 3 \mu\text{m}$), the increase of Δ value causes a lengthening of the focus. Thus, for $\Delta = 5 \mu\text{m}$ a spread of the focus by $\sim 6.25 \mu\text{m}$ occurs.
- (ii) For large Δ , a significant intensity exists throughout the depth of focus, a spread of ~ 12.5 and $15 \mu\text{m}$ for $\Delta = 10$ and $12 \mu\text{m}$, respectively, is appearing.

We should note that these intensity distributions as a function of depth below the air interface have been calculated and discussed, for the different Δ values, considering only the refraction effect.

4.2.3. Confocal micro-Raman response profile

Raman scattering occurs at any point within the illuminated regions described by Fig. 4.5, with a magnitude proportional to the laser intensity at each point. The probability of a Raman photon to be collected by the microscope objective and to pass through the confocal aperture in order to reach the detector will depend upon the point of origin (i.e., z_m^l), which in turn depends on m for the incident ray. In order to obtain an expression for the Raman response as a function of focal position in the sample z_m^l , each point within the sample is weighted, according to the square of the numerical aperture into which a photon can be emitted and still captured by the microscope objective. This “effective” NA is given by the following equation:

$$(NA_{eff})^2 = \frac{1}{n^2} \cdot \left[\frac{m^2 \cdot NA^2}{1 - NA^2 + m^2 \cdot NA^2} \right]. \quad (4.11)$$

Keeping the above mentioned considerations in mind the Raman response profile $R(z_m^l)$ can be obtained by multiplying the laser intensity distribution $m \cdot I(m)$ by the square of the effective numerical aperture NA_{eff}^2 :

$$R(z_m^l) = m \cdot I(m) \cdot (NA_{eff}^2). \quad (4.12)$$

Our goal is to determine the confocal Raman profile as a function of the focal position in the sample z_m^l , therefore a second approach is considered, which assumes that the confocal aperture works perfectly, and only the photons scattered with a specific angle are collected and imaged by the microscope objective and then passed through the pinhole. Neglecting chromatic aberration, this angle is the same as that of the incident laser rays that are focused at the point z_m^l .

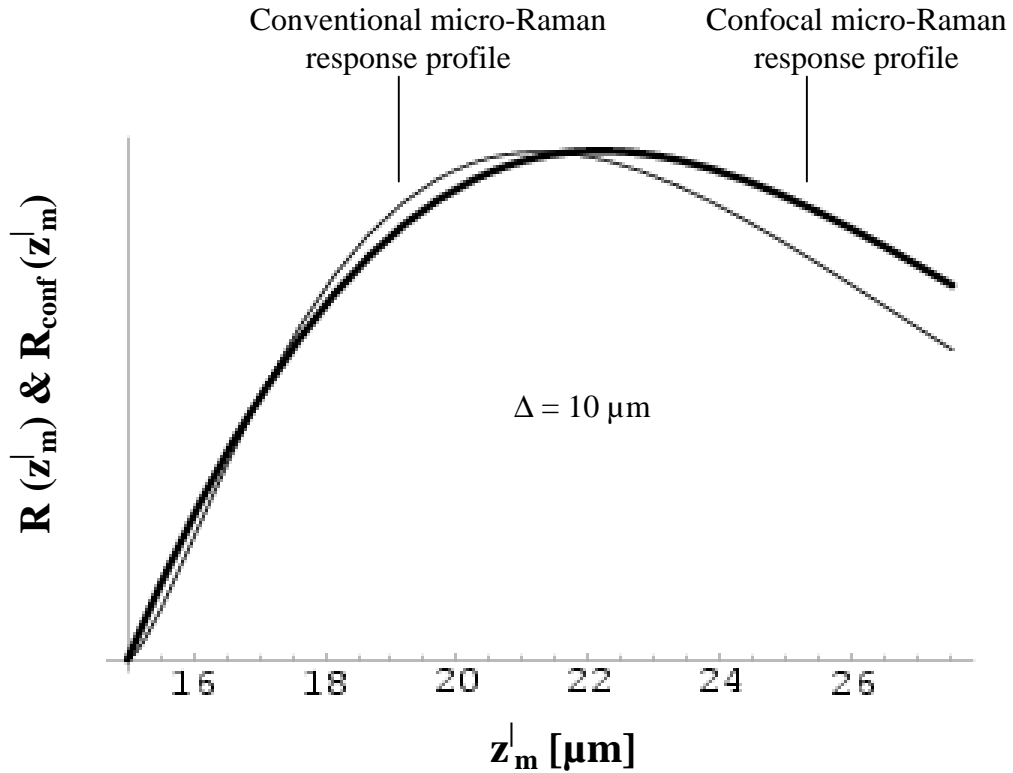


Fig. 4.6. Comparison between conventional micro-Raman and confocal micro-Raman response profiles as a function of the focal position in the sample z_m^l for a nominal focal depth of $\Delta = 10 \mu\text{m}$, when only the refraction effect is considered. Note how the confocal micro-Raman response profile is maximized slightly deeper than the conventional micro-Raman response.

We have already seen that the weighting factor for the probability of a ray traversing this path is simply m . By multiplying the laser intensity distribution by this weighting factor, the confocal Raman response can be expressed as follows:

$$R_{conf}(z_m^l) = m^2 \cdot I(z_m^l). \quad (4.13)$$

The conventional and confocal Raman response profiles are compared in Fig. 4.6. for a nominal depth of $\Delta = 10 \mu\text{m}$. It can be seen that the distributions are fairly similar, the main difference is represented by the fact that the confocal weighting scheme slightly favours signals originating deeper in the sample. The confocal Raman response profiles

as a function of Δ are compared in Fig. 4.7 and are calculated under the assumption that the weighting scheme given by Eq. 4.13 pertains.

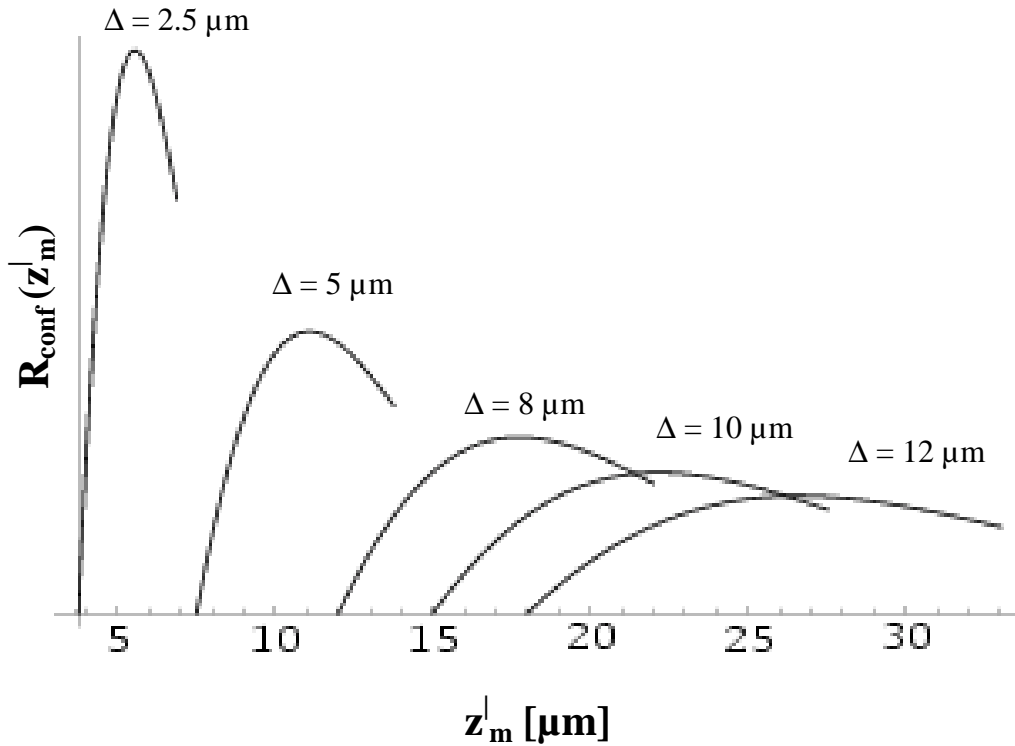


Fig. 4.7. Confocal micro-Raman response $R_{\text{conf}}(z_m)$ vs. focal position in sample z_m as a function of the apparent focal point Δ . Note that the integrated Raman response has been normalised to a constant area, for all Δ values.

From Fig. 4.7 one can observe, as in the calculation of the laser intensity distribution, that the Raman intensity is detected with an increasing depth of focus, as Δ increases. By comparing the Raman response profile with the laser intensity distribution for certain given Δ value, e.g. $\Delta = 10 \mu\text{m}$, one observes that the Raman response is maximised several micrometers deeper than the laser peak intensity (see Fig. 4.8). The shift of the confocal Raman profile maximum compared to the laser intensity distribution maximum becomes higher as Δ increases.

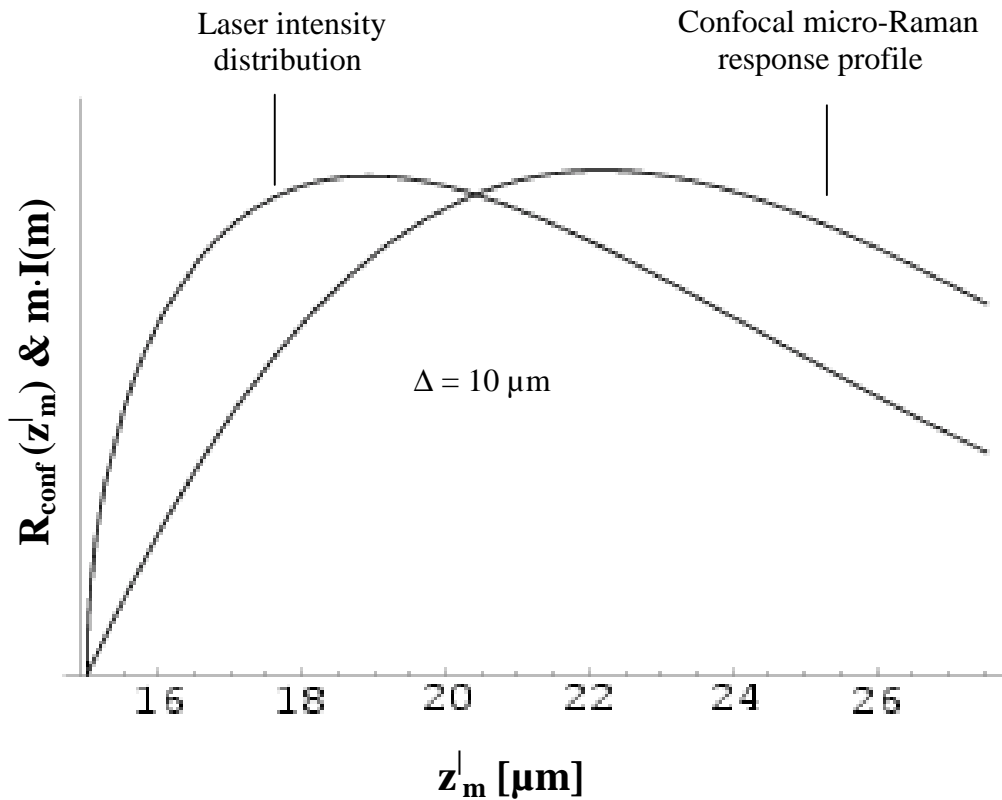


Fig. 4.8. Comparison of the confocal micro-Raman response profile $R_{\text{conf}}(z_m)$ with the laser intensity distribution $m \cdot I(m)$ for $\Delta = 10 \mu\text{m}$. Note how the Raman response is maximised several micrometers deeper than the laser peak intensity.

4.2.4. Comparison of theoretical data with experimental results

The systems chosen for the comparison were described in the experimental section i.e., inorganic-organic hybrid polymer (ORMOCER^{®*}) coatings of 20.2 and 6.2 μm thickness applied on a bisphenol-A polycarbonate sheet of 100*35*2 mm^3 . These samples are perfectly suited for this study since the coating and substrate show at certain spectral regions a good spectral contrast. It should be noted that the substrate is a

* Trademark of Fraunhofer-Gesellschaft zur Förderung der angewandten Forschung e.V., Munich, Germany

very strong Raman scatterer, intense signals could be obtained even from a point situated at some tens of micrometers below the surface. Perhaps the most important point arising from this analysis is the calculation of the confocal Raman response profile across of coating-substrate boundary. It is necessary to emphasize that Raman response profiles can not be directly measured as shown in Fig. 4.7. In fact, only the change in Raman signal intensity as the laser is focused at different points, while the Raman profile moves across a boundary, can be measured. The measured response is the convolution of the changing Raman response profile with the spatial composition profile of the sample.

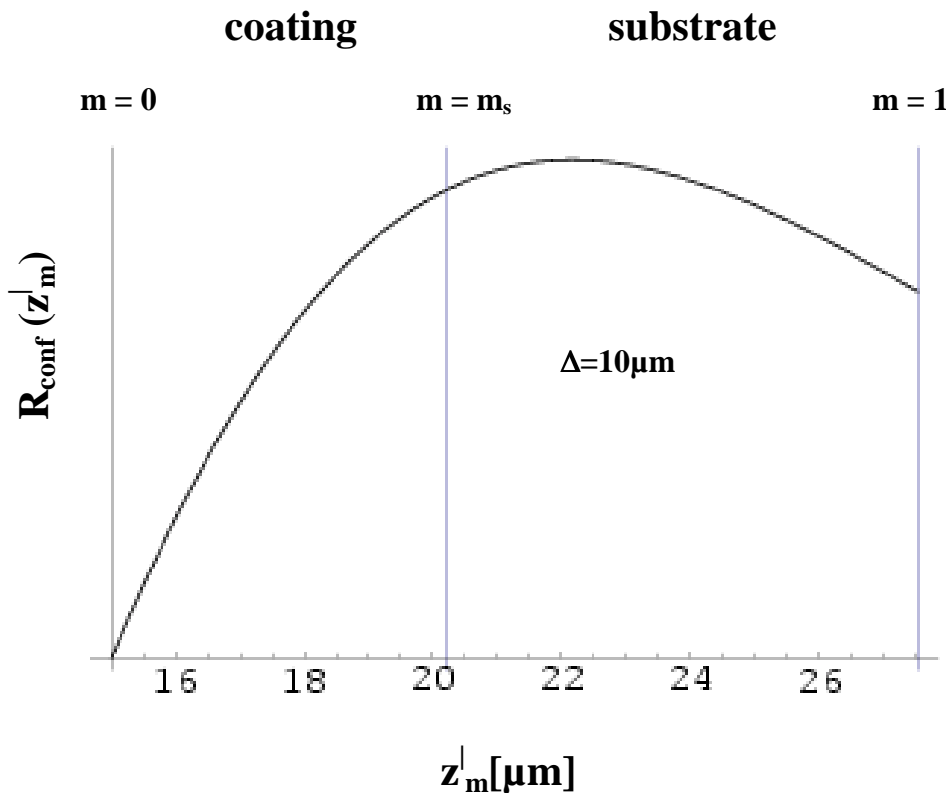


Fig. 4.9. Schematic diagram illustrating the calculation of the substrate signal as a function of Δ . The signal is proportional to the area to the right of the coating-substrate interface.

We evaluate this overlap by calculating the variation in the substrate signal as we focus down through the coating into the substrate (i.e., predict the polycarbonate Raman sign-

al as a function of Δ). This procedure entails the calculation of the area beneath the Raman response curve to the right of the vertical line depicted schematically in Fig. 4.9 and expressed by Eq. 4.14, that represents the boundary between coating and substrate, for a given Δ value (for convenience we have chosen $\Delta = 10 \mu\text{m}$)

$$R_{conf}^{sub}(z_m^{\perp}) = \int_{z_m=m_s}^{z_m=1} R(z_m^{\perp}) \cdot dz_m^{\perp}. \quad (4.14)$$

In Eq. 4.14 and Fig 4.9 m_s represents the value of m for which a Raman ray originates precisely from the coating-substrate boundary. For values $m > m_s$, the rays originate within the substrate and contribute to the detected intensity. As Δ increases, the profile broadens and shifts to higher z_m^{\perp} values, while the boundary position remains constant ($20.2 \mu\text{m}$ in this case). We should mention that the attenuation of the signal due to absorption and turbidity has been neglected.

Several spectra obtained by focusing onto the coating surface and then moving the point of focus into the polycarbonate substrate for both coated samples are presented in Figs. 4.10 and 4.11. We have considered the surface of the coating as the starting point of the measurements ($\Delta = 0 \mu\text{m}$). In order to characterize the intensity evolution of the bands originating solely from the substrate, first we had to identify a spectral region where only bands of the substrate appear. From Figs. 4.10 and 4.11 it is obvious that the Raman bands given by the substrate become more intense as we focused deeper into the sample. Thus, the integrated intensities of the bands between $1546\text{-}1673 \text{ cm}^{-1}$ and $603\text{-}656 \text{ cm}^{-1}$ assigned to the C=C stretching mode in the phenyl ring and phenyl ring bending mode, respectively can be used to test the predicted variations of the Raman response intensity of the substrate at different apparent focal points Δ .

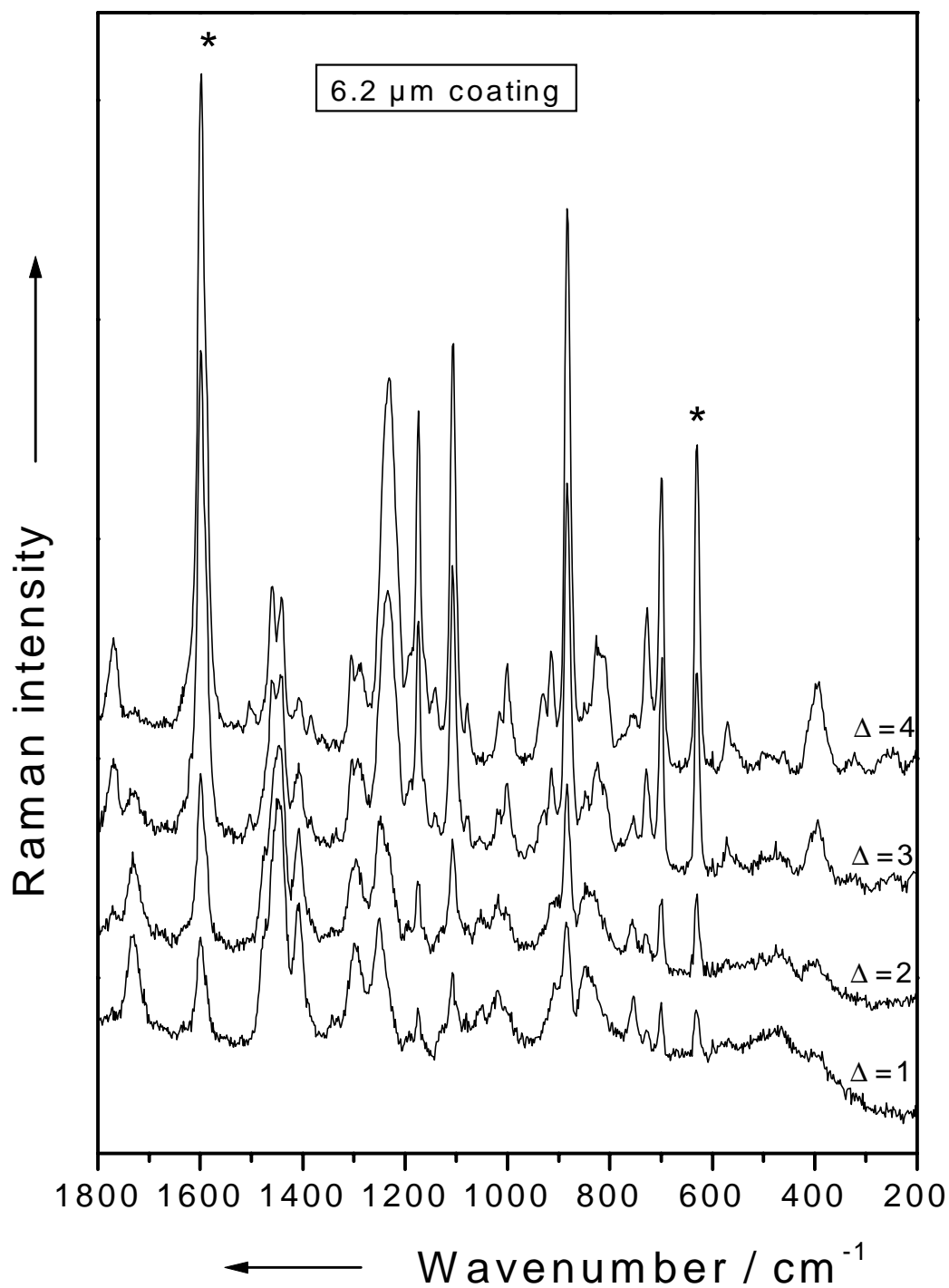


Fig. 4.10. Confocal Raman spectra of polycarbonate sheets equipped with a hybrid polymer coating (6.2 μm in thickness) as a function of apparent focal points Δ . *: denotes the discussed bands. Δ values are given in μm.

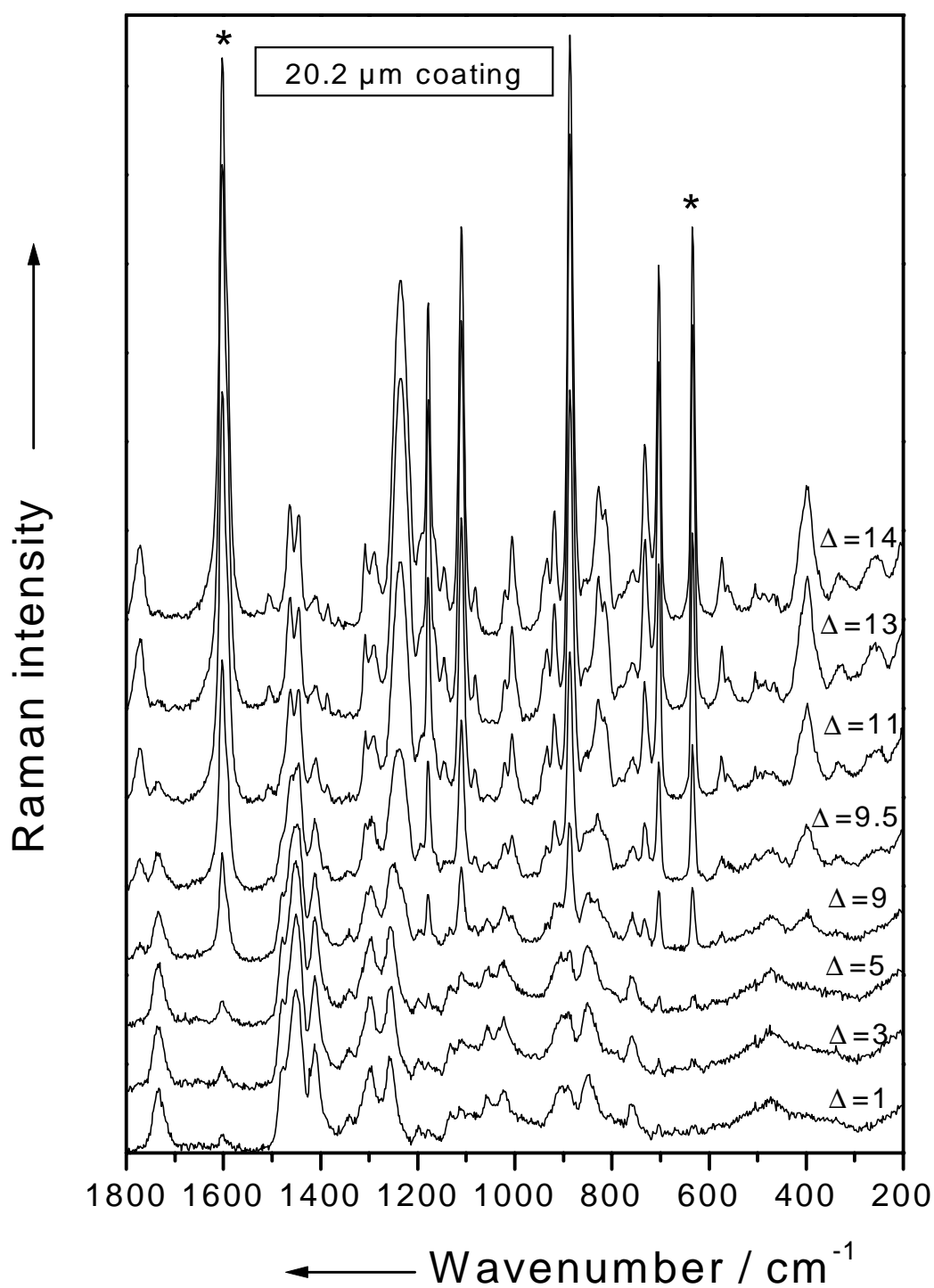


Fig. 4.11. Confocal Raman spectra of polycarbonate sheets equipped with a hybrid polymer coating (20.2 μm in thickness) as a function of apparent focal points Δ . *: denotes the discussed bands. Δ values are given in μm.

In order to determine the accuracy of the theoretical approach we compared the theoretical data with the experimental results. The theoretical and experimental data are plotted as the percentage of the total confocal Raman response $R_{conf}(z_m^l)$ vs. apparent focal points Δ in Fig. 4.12.

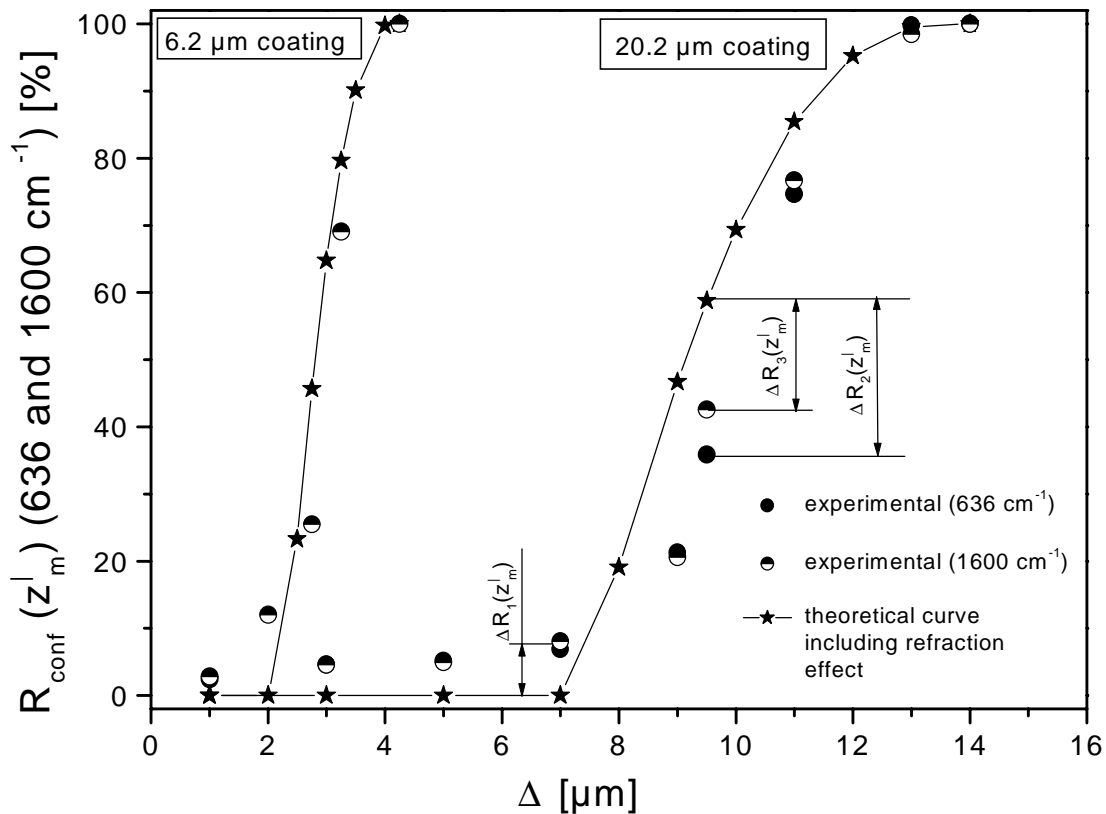


Fig. 4.12. Comparison of calculated and observed percentage of the total confocal micro-Raman responses $R_{conf}(z_m^l)$ of two polycarbonate substrate bands (1600 and 636 cm^{-1}) as a function of the apparent focal points Δ , when only the refraction effect was considered.

By comparing the theoretical results with the experimental data (Fig. 4.12) a fairly good agreement can be observed. However, a detailed analysis of Fig. 4.12 reveals the presence of some discrepancies between experimental and theoretical results. Possible interpretations of the observed differences between the measured and calculated values could be the following:

-
- (i) The differences between experimental and theoretical data might be due to the fact that the differential cross-section of the analyzed substrate modes is higher than that of the strongest coating modes. Thus, the polycarbonate Raman bands at 636 and 1600 cm^{-1} are present even at small Δ values (e.g., $\Delta R_1(z_m^l)$ for the Raman bands at 636 and 1600 cm^{-1} , respectively, at $\Delta = 7$ μm for the sample of 20.2 μm thickness).
 - (ii) The laser intensity outside the Airy disc could contribute also to the deviations (e.g., $\Delta R_1(z_m^l)$ observed at small Δ values).
 - (iii) The neglect of the diffraction effect could contribute to the appearance of the errors between experimental and theoretical data especially at the coating/substrate interface (e.g., $\Delta R_2(z_m^l)$ and $\Delta R_3(z_m^l)$ for the Raman bands at 636 and 1600 cm^{-1} , respectively, at $\Delta = 9.5$ μm for the sample with 20.2 μm thickness).

In a recent study, Baldwin and Batchelder⁶⁹ demonstrated that the pinhole plays a very important role and must be considered for thick films (e. g. thousands of micrometers). It rejects some of the Raman signal originating from the blurred laser focus and gives a sharper depth resolution than is predicted by the above applied model^{58,68}, but only at depths of thousands of micrometers. However, both models only treat the influence of the refraction effect on confocal measurements. In order to minimize the above observed errors, $\Delta R_2(z_m^l)$ and $\Delta R_3(z_m^l)$, respectively, a model which takes additionally the diffraction effect on the focus lengthening on confocal micro Raman experiments into account has been developed and will be presented in the next section.

4.3. The influence of both refraction and diffraction effects on the depth resolution on confocal Raman microscopy

When using geometrical optics to characterize a lens, it is assumed that no diffraction effect occurs. However, geometrical optics itself is an approximation. If we want to make a rigorous wave-optical analysis of the formation of an image by a lens, we would find that diffraction effects arise in a natural way. The image formed by a lens can be distorted by other effects, including chromatic and spherical aberrations. These effects can be substantially reduced or eliminated by suitable shaping of the lens surfaces or by introducing correcting elements into the optical system. However, no design can eliminate the effects of diffraction, which are only determined by the size of the aperture (the diameter of the lens) and the wavelength of the light. In diffraction, nature imposes a fundamental limitation on the precision of the instruments.

In imaging applications, spatial resolution is ultimately limited by diffraction. The diffraction pattern resulting from an uniformly illuminated circular aperture, the final lens in the microscope objective, actually consists of a central bright region, known as the Airy disc, which is surrounded by a number of much fainter rings, each ring being separated by a circle of zero intensity.

4.3.1. Laser intensity distribution

The main advantage of confocal microscopy is represented by the dramatic improvement of the depth discrimination and a slight decrease of the lateral resolution. The latter, known as intensity point spread function (PSF) is given by:^{70,71}

$$I(v) = \left[\frac{2J_1(v)}{v} \right]^4, \quad (4.15)$$

where J_1 is the first order Bessel function and v is the normalized distance to the optical axis.

The intensity variation in a confocal microscope along the z -axis in the neighborhood of the image plane of a point object placed at a normalized distance

$$u = \frac{2\pi}{\lambda} \cdot z \cdot \sin^2 \alpha \quad (4.16)$$

from the focal plane of the microscope objective (of angular aperture α) is given by:^{70,71}

$$I(u) = \left| \frac{\sin \frac{u}{4}}{\frac{u}{4}} \right|^4. \quad (4.17)$$

Because the depth of focus increases as Δ increases, due to the refraction effect, we have defined⁷²⁻⁷⁴ a “**broadening factor**“ of the diffraction in a medium with the refractive index n_1 ($n_1 = 1.5$ in our case) as follows:

$$k = \frac{d.o.f.}{l}, \quad (4.18)$$

where l represents the length of the focus in micrometers, neglecting its raising as Δ increases ($l = 3$ in our case). This effect onto the focus lengthening can be observed in the intensity variation along the z -axis if z in Eq. 4.16 is replaced by z_m^l/k . Considering that in a medium with a refractive index n_1 (see Fig. 4.2),

$$\sin \alpha_{\max}^l = \frac{n_2 \cdot \sin \alpha_{\max}}{n_1} = \frac{NA}{n_1}, \quad (4.19)$$

and that the diffraction maximum occurs in the z_m^l points (along the optical axis), where the laser intensity in the sample has a maximum value when only the refraction effect is considered, Eq. 4.16 becomes:

$$u^l = 2\pi \cdot NA^2 \cdot \frac{z_m^l - z_m^l \left(\frac{dI(z_m^l)}{dz_m^l} \right) \Big|_0}{\lambda \cdot k \cdot n_1^2}. \quad (4.20)$$

Taking into account that both the term $dI(z_m^l)/dz_m^l$ and the factor k are defined as a function of the apparent focal point Δ , the intensity variation along the z -axis has different values at different depths into the sample and can be expressed as following:

$$I^l(z_m^l) = \left| \frac{\sin \left[\frac{2\pi \cdot NA^2 \cdot (z_m^l - z_m^l) \left(\frac{dI(z_m^l)}{dz_m^l} \right) \Big|_0}{\lambda \cdot k \cdot n_1^2} \right]}{4} \right|^4 \cdot \frac{2\pi \cdot NA^2 \cdot (z_m^l - z_m^l) \left(\frac{dI(z_m^l)}{dz_m^l} \right) \Big|_0}{\lambda \cdot k \cdot n_1^2}}{4} \quad (4.21)$$

In Fig. 4.13 we have plotted the intensity distribution $I^l(z_m^l)$ as a function of the focal position z_m^l for five different values of Δ (2.5, 5, 8, 10, and 12 μm , respectively) assuming the intensity amplitude of the laser beam $I_0 = 1$, an optimum filling of the microscope objective ($\phi = 1$) and a microscope objective with 0.9 NA.

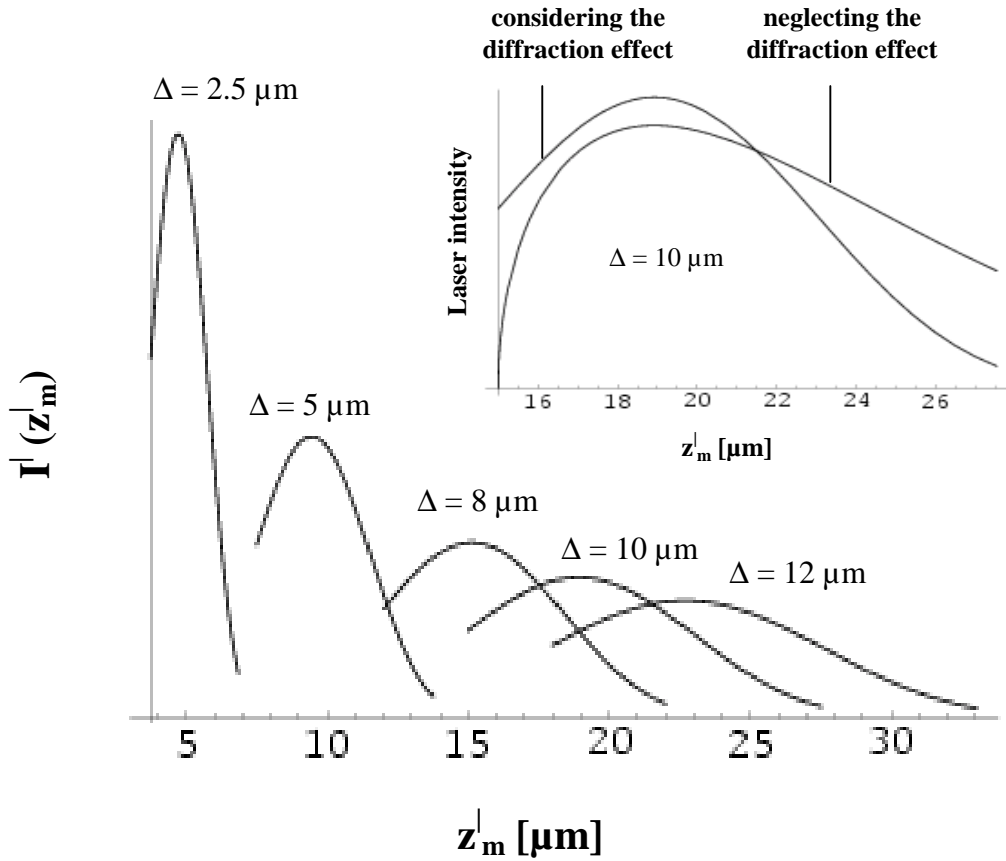


Fig. 4.13. Laser intensity $I^l(z_m^l)$ vs. focal position in the sample z_m^l as a function of the apparent focal point Δ . Note that the integrated intensity has been normalized to a constant area, for all Δ values. The insert compares the laser intensity distribution for two cases: neglecting and considering the diffraction effect.

These plots have been normalized to a constant integrated intensity in order to maintain the same intensity of the laser in the entire focal volume at different values of Δ . We have considered that the maximum integrated intensity is obtained for the broadening factor $k = 1$. We should emphasize that these intensity distributions as a function of depth below the air/sample interface have been calculated for different Δ values considering both the refraction effect as well as the diffraction effect. By analysing Fig. 4.13. the following observations can be made:

- (i) For a small Δ value ($\Delta = 2.5 \mu\text{m}$) the depth of focus is comparable to the diffraction limit ($\sim 3 \mu\text{m}$). An increase of the Δ value has as a consequence a lengthening of the focus.
- (ii) By comparing the behaviour of the laser intensity distribution when only the refraction effect occurs with that when diffraction effect is additionally considered (see the inserted figure), a remarkable change of the laser intensity distribution is evidenced.

4.3.2. Micro-Raman response profile

The next step in the development of a theoretical model, which considers both refraction and diffraction effects, is to derive an expression for weighting the Raman response at different focal points z_m^l as a function of the apparent focal point Δ applying the already computed laser intensity distribution. Therefore, we consider that each point inside the sample is weighted according to the square of the numerical aperture (a photon can be emitted and still captured by the objective; see Eq. 4.11), and thus the Raman response at different depths can be calculated with the following equation:

$$R^l(z_m^l) = I^l(z_m^l) \cdot (NA_{eff}^2). \quad (4.22)$$

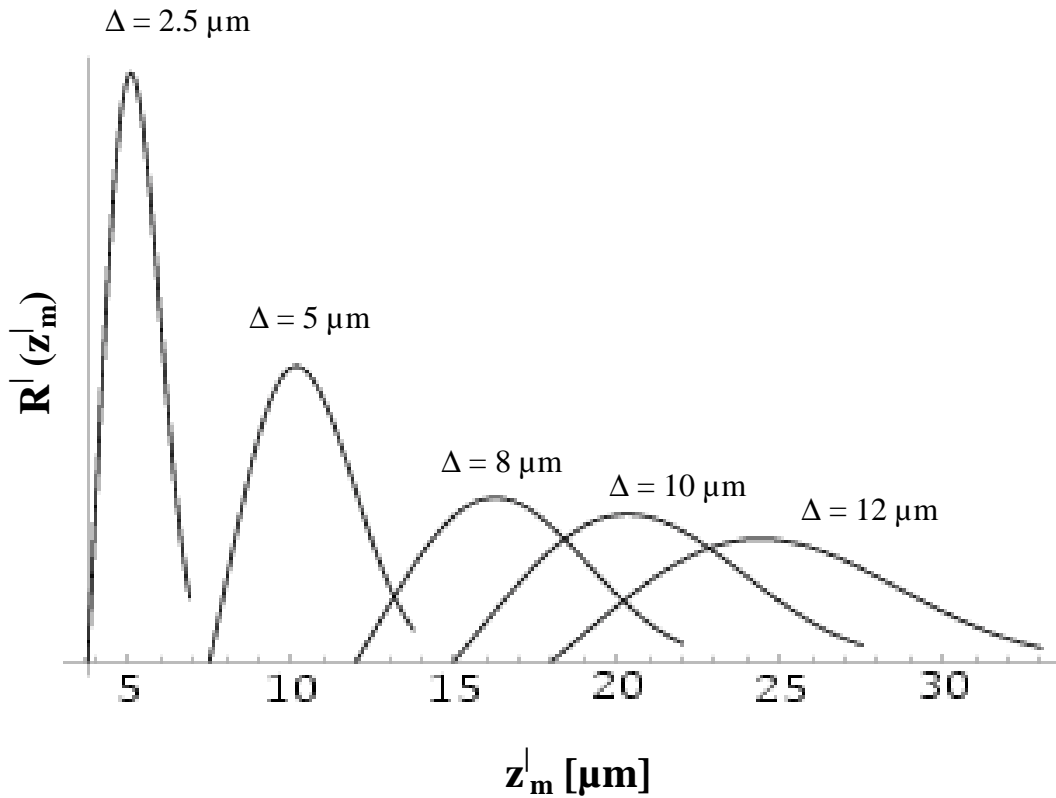


Fig. 4.14. Raman response $R^l(z_m)$ vs. focal position in sample z_m^l as a function of the apparent focal point Δ . Note that the integrated Raman response has been normalised to a constant area, for all calculated Δ values.

Assuming that at different z_m^l levels lengthways the focus, the integrated intensity along the x and y axis remains constant (no refraction effect), we can now consider and compute the spatial Raman response $R^l(z_m^l)$ given by Eq. 4.22. The dependence of the Raman response profile $R^l(z_m^l)$ on the focal position inside the sample z_m^l as a function of the apparent focal point Δ is illustrated in Fig. 4.14. It can be observed from this figure that, when both refraction and diffraction effects are considered, the Raman response distribution is detected with an increasing depth of focus as Δ increases.

4.3.3. Confocal micro-Raman response profile

The main benefit of confocal micro-Raman spectroscopy in comparison to conventional Raman spectroscopy consist of the ability of the confocal system to eliminate regions out of focus, an improvement of the spatial resolution, especially the depth discrimination, occurring. In order to compute the confocal Raman response, which arrives on the CCD detector, the Raman response behind the confocal pinhole must be calculated. It should be also noted that the lateral resolution remains constant for every measurement along the z -axis. A calculation of the proportion of the flux Φ_T , which is transmitted through the pinhole diaphragm (confocal Raman response) has been reported in a previous study.⁷⁰ This is given by:

$$\Phi_T \approx \frac{R_d}{\left\{ \Gamma_0 \left[NA \cdot z_m^l + R_0 \cdot \sqrt{1 + (\sin^{-1} NA \cdot z_m^l)^2} \right] \right\}^2}, \quad (4.23)$$

where z_m^l , R_d , R_0 , Γ_0 and NA are the axial altitude of a slice of the sample, the radius of the pinhole, the radius of the laser beam at the sample, the magnification factor and the numerical aperture of the microscope objective, respectively. The maximum Raman response $(dR^l(z_m^l)/dz_m^l)|_0$ occurs at the same normalized radius m indifferent of the depth where it was calculated. Replacing the z_m^l value by z_m^l/k in Eq. 4.22, translating the normalized flux transmitted through the pinhole at the z_m^l points, where the maximum Raman response occurs, and normalizing Eq. 4.22, the percentage from the confocal Raman response, which arrives behind the confocal pinhole, can be obtained for each z_m^l level lengthways the focus

$$\Phi_T^l \approx ct \cdot \frac{R_d}{[\Gamma_0 \cdot (A + B)]^2}, \quad (4.24)$$

where:

$$A = NA \cdot \frac{z_m^l - z_m^l (dR^l(z_m^l)/dz_m^l)|_0}{k}$$

and

$$B = R_0 \cdot \sqrt{1 + \left(\sin^{-1} NA \cdot \frac{z_m^l - z_m^l (dR^l(z_m^l)/dz_m^l)|_0}{k} \right)^2}.$$

The confocal Raman response on the CCD detector as a function of the axial altitude into the sample can be expressed as:

$$R_{conf}^l(z_m^l) \approx I^l(z_m^l) \cdot (NA_{eff})^2 \cdot \Phi_T^l. \quad (4.25)$$

Furthermore, we evaluated the variation in the confocal Raman substrate signal $R_{conf}^l(z_m^l)$ as we focused down through the coating into the polycarbonate substrate. Five of these confocal Raman responses are plotted as a function of z_m^l in Fig. 4.15, for $\Delta = 2.5, 5, 8, 10,$ and $12 \mu\text{m}$, respectively.

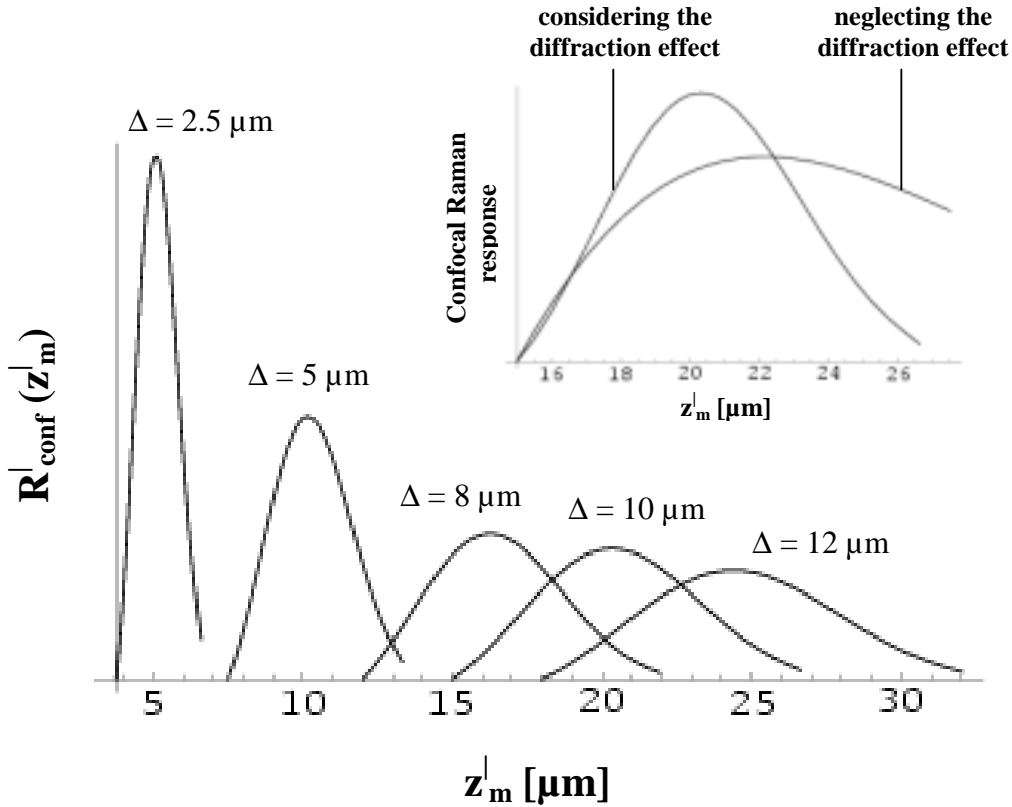


Fig. 4.15. Confocal Raman response $R_{conf}^l(z_m^l)$ vs. focal position in the sample z_m^l as a function of the apparent focal point Δ . Note that the integrated Raman response has been normalized to a constant area, for all calculated Δ values. The insert compares the confocal Raman responses for two cases: neglecting and considering the diffraction effect.

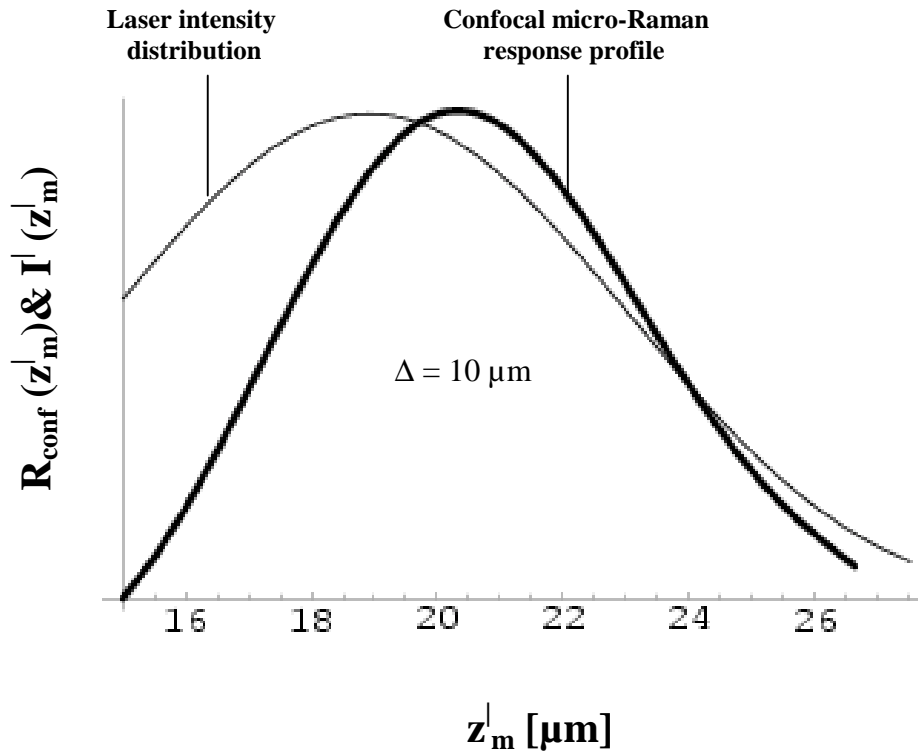


Fig. 4.16. Comparison of the confocal micro-Raman response profile $R_{conf}^l(z_m^l)$ with the laser intensity distribution $I^l(z_m^l)$ for $\Delta = 10 \mu\text{m}$ when both refraction as well as diffraction effects are considered. Note how the confocal Raman response is maximised several micrometers deeper than the laser peak intensity.

By comparing the confocal Raman response profile with the laser intensity distribution for a given Δ value, e.g. $\Delta = 10 \mu\text{m}$, one remarks that, similar to the case when only the refraction effect has been considered, the Raman response is maximised several micrometers deeper than the laser peak intensity, even if both refraction and diffraction effects are taken into account (see Fig. 4.16). It can be also seen that the shift of the Raman profile maximum compared to the intensity distribution maximum becomes larger as Δ increases.

4.3.4. Comparison of theoretical data with experimental results

We should note that similar to the previous case when only the refraction effect was considered, in the present approach, when additionally the diffraction effects is taken into account, only the change in Raman signal intensity as the laser is focused at different points and the Raman profile moves across a boundary can be computed. In fact, the measured confocal Raman response represents a convolution of the substrate Raman response, which passes through the pinhole diaphragm.

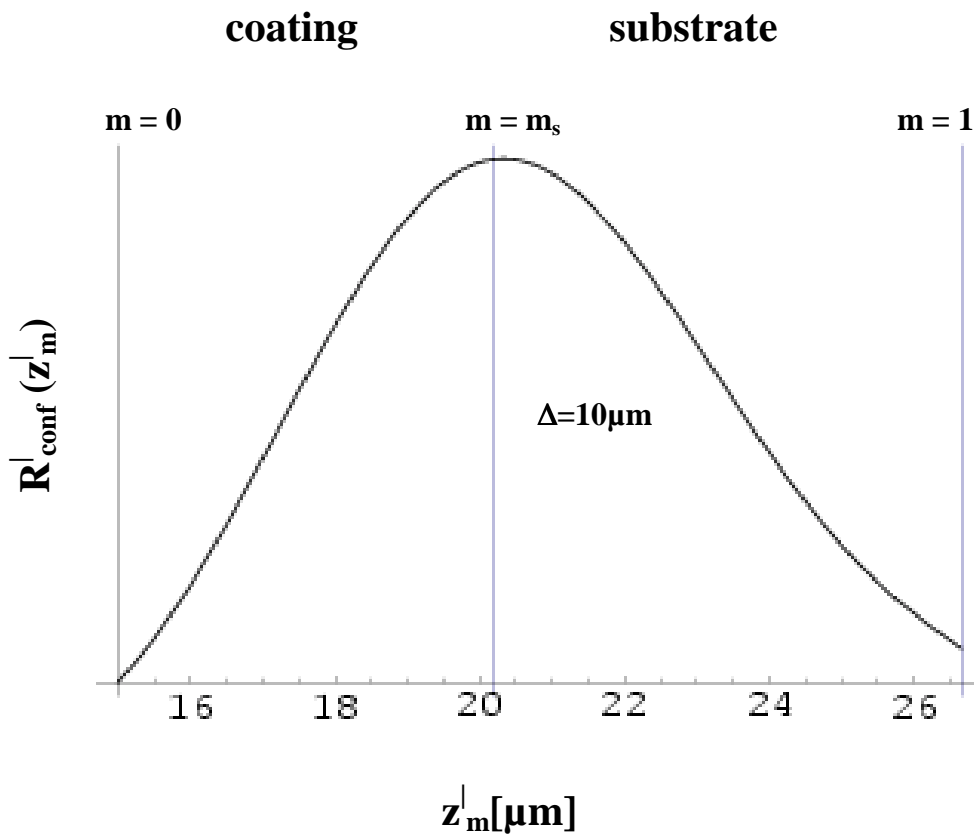


Fig. 4.17. Schematic diagram illustrating the calculation of the substrate signal as a function of Δ . The signal is proportional to the area right of the coating/substrate boundary.

We evaluate this overlap by calculating the variation in the substrate signal as we focus down through the coating into the substrate (i.e., predict the polycarbonate Raman sign-

al as a function of Δ). This procedure entails the calculation of the area under the curve to the right of the vertical line (Fig. 4.17), this line is corresponding to the boundary between coating and substrate (for convenience we have chosen $\Delta = 10 \mu\text{m}$). In Fig. 4.17, m_s represents the value of m for which a Raman ray originates precisely from the coating/substrate boundary.

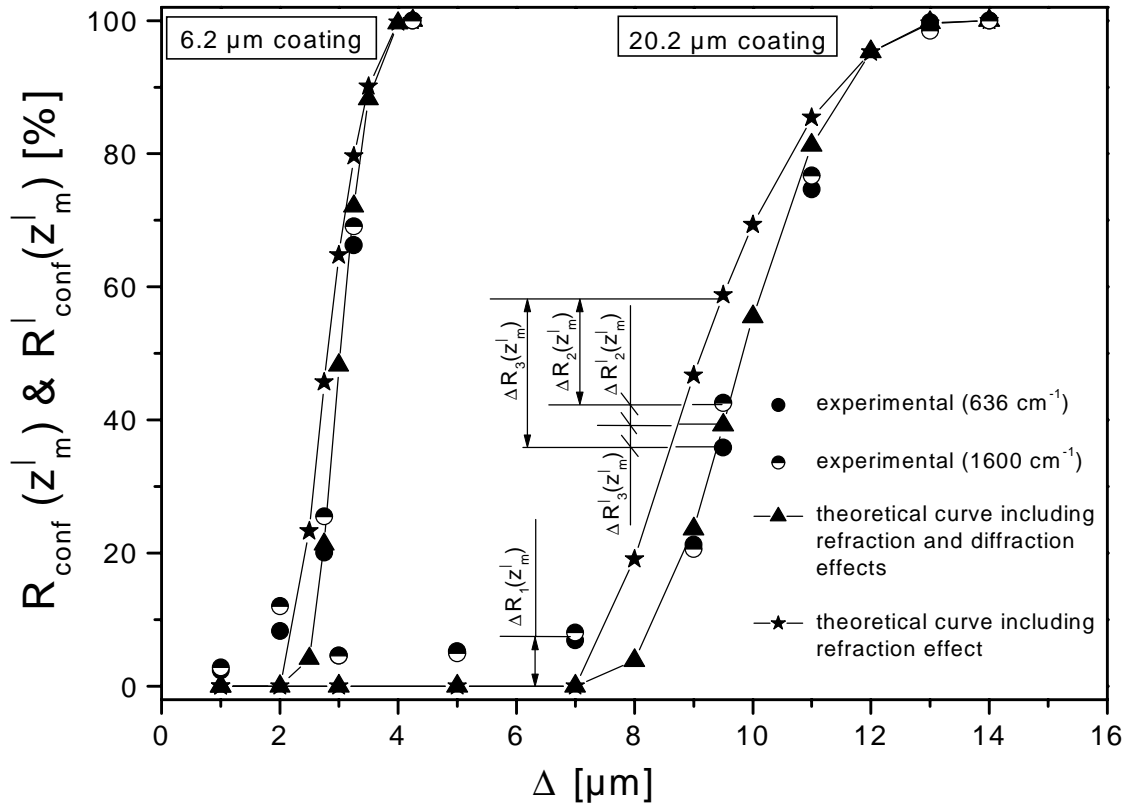


Fig. 4.18. Comparison of calculated confocal Raman response percentage when the diffraction effect is neglected $R_{\text{conf}}(z_m^l)$ and considered $R_{\text{conf}}^l(z_m^l)$ with the observed data for two polycarbonate substrate bands (1600 and 636 cm^{-1}) as a function of apparent focal points Δ .

In order to compare the theoretical data with the experimental results, we have characterized the evolution of the same Raman bands given by the substrate, as it has been presented in the previous section, when only the refraction effect was considered. Thus, the integrated intensities of the polycarbonate bands at 1600 cm^{-1} and 636 cm^{-1} assigned to the C=C stretching mode in the phenyl ring and phenyl ring bending mode,

respectively, have been used to test the predicted variations of the polycarbonate Raman signal at different apparent focal points Δ . A plot of the theoretical values obtained when the diffraction effect is neglected and then considered, $R_{conf}(z_m^l)$ and $R_{conf}^l(z_m^l)$, respectively, and of the experimental data as the percentage of the confocal Raman response vs. apparent focal points Δ is presented in Fig. 4.18. As can be observed, by considering both the refraction as well as the diffraction effects the agreement between the experimental and theoretical data is improved in particular at the coating/substrate interface in comparison with the theoretical approach, where only the refraction effect was taken into account.

By comparing the above presented models with the experimental data (Fig. 4.18), the following considerations, concerning the errors which appear between the measured and calculated values, could be drawn.

- (i) Even if the diffraction effect is considered the differences observed in Fig. 4.18 at small Δ values may suggest that the differential Raman cross-section of the analyzed substrate modes is higher than that of the strongest coating modes. Thus, the polycarbonate Raman bands at 636 and 1600 cm^{-1} are present even at small Δ values (e.g., $\Delta R_1(z_m^l)$ represents the error between theory and experiment for the Raman bands at 636 and 1600 cm^{-1} , respectively at $\Delta = 7 \mu\text{m}$ for the sample with 20.2 μm thickness).
- (ii) The laser intensity outside the Airy disc could contribute also to the deviations observed at small Δ values.
- (iii) The errors, which have been evidenced in the previous model, where only the refraction effect has been considered, have been minimized by considering a new approach (see Fig. 4.18), which takes both the refraction and the diffraction effects into account (e.g., $\Delta R_2(z_m^l)$ and $\Delta R_3(z_m^l)$ in comparison with $\Delta R_2^l(z_m^l)$ and $\Delta R_3^l(z_m^l)$, respectively, for the polycarbonate

Raman bands at 636 and 1600 cm^{-1} , at $\Delta = 9.5\text{ }\mu\text{m}$ for the sample with $20.2\text{ }\mu\text{m}$ thickness).

- (iv) The length of the focus calculated according to the previous model, where only the refraction effect has been considered, agrees quite well with the experimental data for thin coatings and was found to be $\sim 12.5, 15,$ and $17.5\text{ }\mu\text{m}$ for Δ of $10, 12,$ and $14\text{ }\mu\text{m}$, respectively. When the diffraction effect is taken into account the focus length becomes $\sim 11.65, 14,$ and $16.3\text{ }\mu\text{m}$ for the same Δ values. By comparing the values of the focus length calculated according to both theoretical models we can conclude that the diffraction effect reduces the lengthening of the focus, improving thus the degree of agreement between theory and experiment.

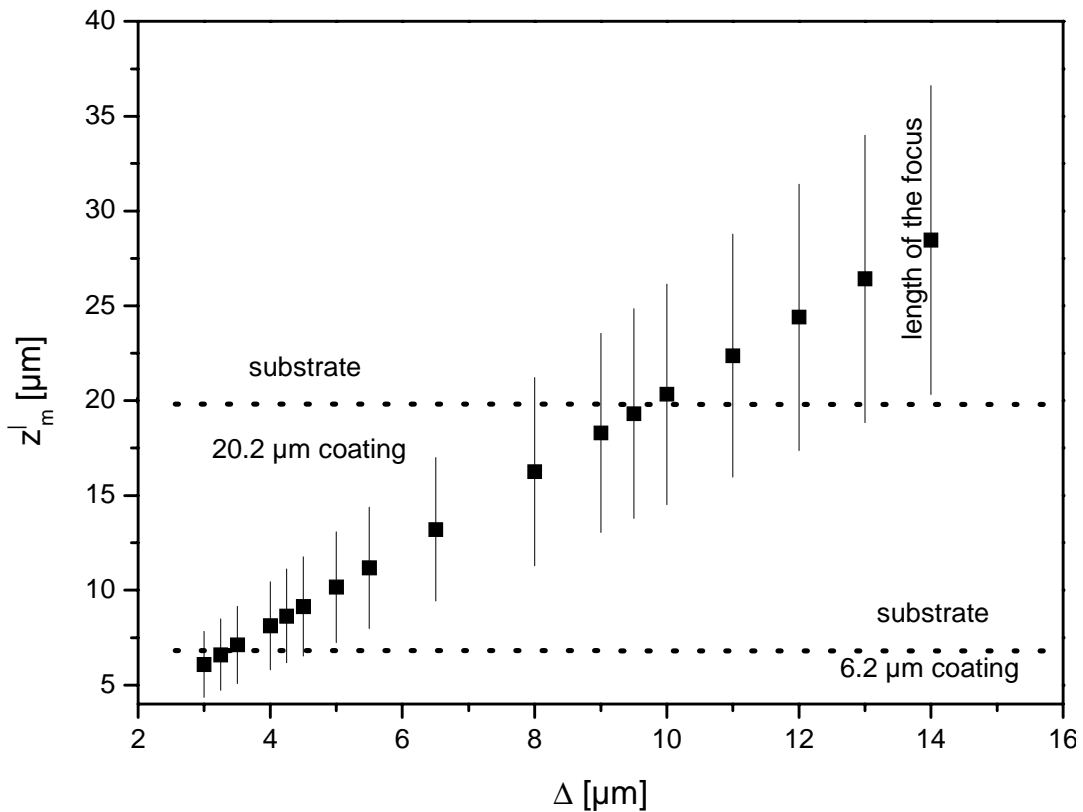


Fig. 4.19. The lengthening of the focus along the z -axis for different apparent focal points Δ when refraction and diffraction effects are considered. Note how a better discrimination of the Raman response proceeded from different levels along the optical axis could be obtained if the thickness of the coating is smaller.

The theoretical variation of the focus length at different focal positions z_m^l as a function of apparent focal points Δ is presented in Fig. 4.19. It can be seen that the focus length is enlarged when the focus is placed deeper into the sample, thus preventing a sharp discrimination along the optical axis. Fig. 4.19 also reveals that by decreasing the coating thickness an improved discrimination along the optical axis can be achieved.⁷³

4.4. Conclusion

A relatively straightforward analysis based on ray tracing has been applied in order to compute the confocal micro-Raman response profile at different depths inside two different coated samples of 6.2 and 20.2 μm thickness, by considering the spherical aberrations induced by the presence of the air/coating interface, and a focus lengthening was evidenced. The obtained theoretical data have been compared with the experimental and a fairly good agreement was observed.

Furthermore, a theoretical approach that considers both the effects of refraction and diffraction on the focus lengthening on confocal micro-Raman experiments has been developed. A calculation of the confocal micro-Raman response profile as a function of the apparent focal point Δ , numerical aperture and magnification of the objective (NA , Γ_0), refractive index of the sample n , and the characteristics of the pinhole and the laser beam (R_d , R_0) for different z_m^l levels into the sample has been performed. The results obtained by applying the developed theoretical model are in good agreement with the experimental data.

According to this approach, the lengthening of the focus deeper into the sample becomes less pronounced as compared to the case when only the refraction effect is considered. The intensity of the Raman response given by the substrate is already increased in the neighborhood of the substrate level, preventing thus a sharp discrimination. If the thickness of the coating is smaller, a better discrimination of the confocal Raman response proceeding from different levels along the optical axis could be obtained. In comparison to the model, which takes only the refraction effect into acc-

out, a shortening of the focal length is obtained when both the refraction and diffraction effects are considered, thus improving the agreement between the experimental and theoretical data, particularly at the coating/substrate interface.

5

Characterisation of diffusion processes of pharmacologically relevant molecules through PDMS membranes by means of confocal resonance micro Raman spectroscopy

5.1. Introduction

During the past few years the development of new application systems for a defined release of active ingredients became more and more important in the pharmaceutical industry. In his pioneering work Zaffaroni pointed out⁷⁵ that such objectives can be met by what he called therapeutic systems. Such systems always consist of four basic comp-

onents: an energy source which delivers the energy needed for a controlled drug release, a drug depot, a support element which fixes the therapeutic system at the application site and carries the other elements of the system, and eventually an element to control rate and extent of the drug release. Usually a polymer membrane is used to control the drug release.⁷⁵ The advantages of using PDMS membranes for drug delivery system is known since the beginning of the sixties. Due to their biocompatibility and inertness PDMS membranes are widely used in pharmaceuticals e.g. as coating material for tablets, in ophthalmic preparations, in transdermal devices to control drug delivery into the skin, in intrauterine inserts, as vaginal rings as well as subdermal implants to deliver contraceptives.⁷⁶⁻⁸¹ The knowledge of the diffusion properties of such control membranes is very important in order to achieve a defined and constant drug release from therapeutic systems. However this knowledge is still insufficient. Therefore it is important to continue to investigate these properties carefully.

Recently, some studies have evidenced that confocal micro-Raman spectroscopy is an excellent tool for probing spatial variations in multiphase materials.⁸²⁻⁸⁴ Proton-conducting membranes of poly(vinylidene fluoride), PVDF, grafted with styrene and thereafter sulfonated, were investigated by Raman spectroscopy.⁸² The depths and surface distribution of polystyrene grafts and crosslinker, as well as the sulfonation efficiency, were determined by using confocal micro Raman spectroscopy. The same spectroscopic method has been used in order to determine the structural changes in the PVDF-graft-poly(styrene sulfonic acid) membrane composition after fuel cell experiments.⁸³ Composition profiles generated by diffusion in the concentrated regime between poly(phenylene oxide)-polystyrene blend pairs have been also experimentally determined by means of confocal micro-Raman spectroscopy.⁸⁴ By depth profiling of PVC laminates with aminothiophenol a gradient in the degree of modification has been established.^{85,86} A quantification of pharmacokinetic variables by using *in vivo* confocal Raman spectroscopy in order to obtain continuous real-time monitoring of the drug concentration in the corneal hydration from rabbit eyes has been also reported.^{87,88} Significant qualitative differences in the axial hydration gradient were observed between the *in vitro* and *in vivo* situation from the characterization of the axial corneal hydration process.⁸⁹ H₂O/D₂O exchange in human eye lens has been monitored *in vitro*

by confocal Raman microspectroscopy and the diffusion coefficient of D₂O in the human eye lens has been established.⁹⁰

In the work presented here, this method of confocal resonance Raman spectroscopy is applied to the investigation of the diffusion process of β -carotene dissolved in DMSO through a PDMS membrane. β -Carotene has been used as a test molecule for pharmaceutically relevant substances.

5.2. Results and discussion

As the Raman signal is proportional to the concentration, confocal resonance Raman spectroscopy can be used for quantitative analysis. The concentration of molecules diffusing through the membranes is rather low. Therefore, β -carotene was chosen as a test molecule to investigate the diffusion process through PDMS-membranes. It can be detected even in low concentrations by taking advantage of the resonance Raman effect. Resonance Raman scattering occurs when the photon energy of the exciting laser beam matches that of an electronic transition of a chromophoric group within the system under study. Under these conditions bands belonging to the chromophore are selectively enhanced by factors of 10^3 to 10^5 . In the case of β -carotene the excitation laser at 514 nm is resonant with the S₂-absorption in β -carotene.

In order to investigate the diffusion process of β -carotene through PDMS membrane Raman spectra as a function of the time have been recorded at various depths inside the membrane by considering the upper surface of the membrane as the starting point of the measurements. Because the substances involved in these confocal Raman investigations have different refractive indexes, the theoretical models, which have been presented in the previous chapter and describe the influence of refraction and diffraction effects on the focus lengthening on confocal micro-Raman experiments, could not be applied.

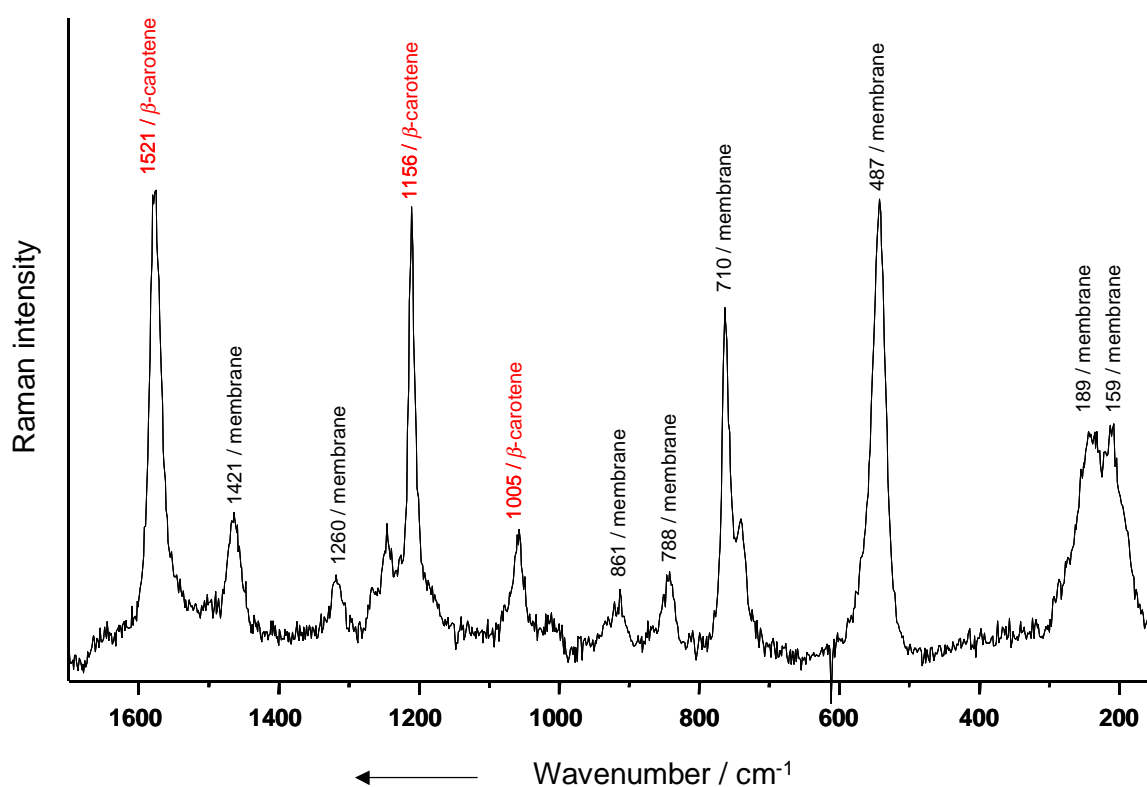


Fig. 5.1. Raman spectrum recorded during the permeation of β -carotene/DMSO-solution through a PDMS membrane. The membrane and β -carotene peaks are marked as indicated.

Figure 5.1 shows a Raman spectrum recorded during the diffusion of β -carotene through a PDMS membrane at a depth of 25 μm inside the membrane (value read on the microscope scale). The spectrum only shows bands, which can be assigned to vibrations of the polymer chains forming the membrane, or of β -carotene but no bands of the solvent DMSO could be observed, probably due to its low concentration or to the high intensity of β -carotene bands. The integral of any β -carotene peak is directly proportional to the amount of β -carotene being present at a specific depth of measurement at a given time. In order to correct potential variations in the laser intensity the integral over the β -carotene peak at 1521 cm^{-1} was normalized to the membrane peak at 487 cm^{-1} .

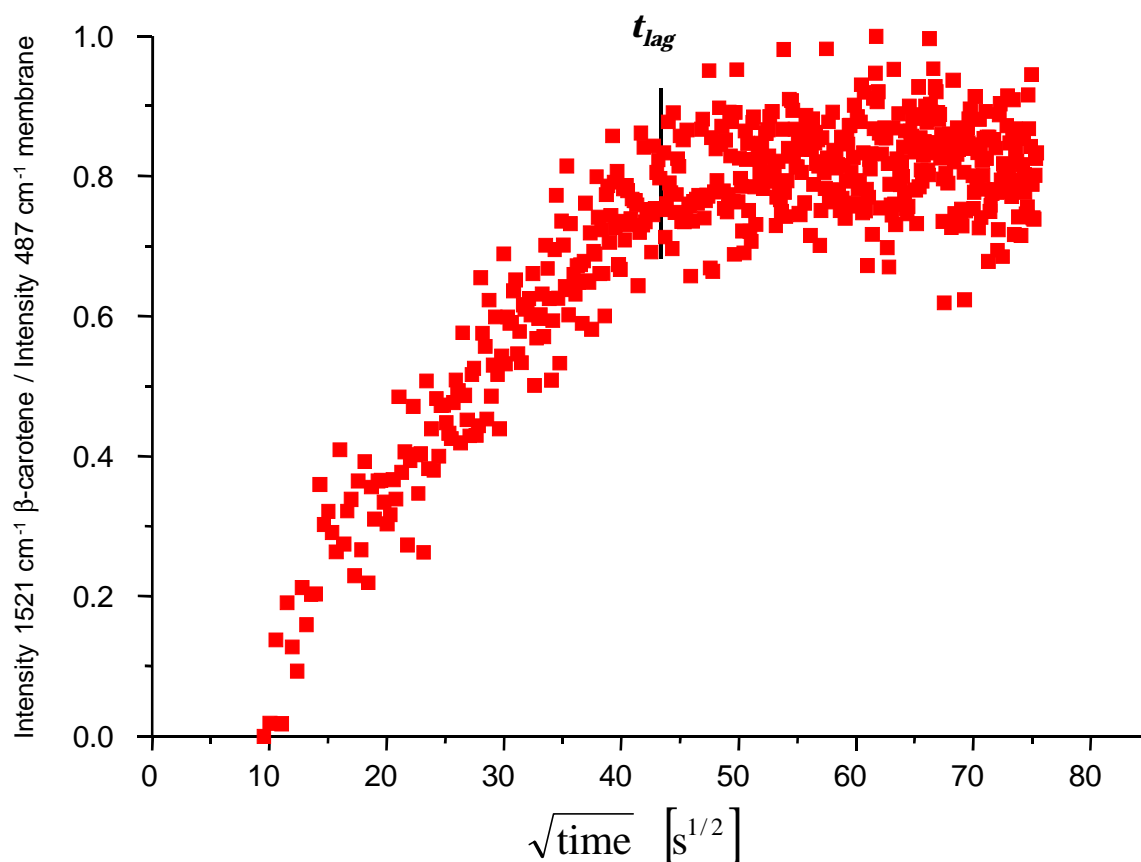


Fig. 5.2. Normalized sorption curve measured in a depth of 25 μm (for details see text).

In Fig.5.2 the intensity of this normalized peak of β -carotene recorded at a depth of 25 μm inside the membrane is plotted against the square root of diffusion time. For diffusion times up to 1600 s the concentration of β -carotene is directly proportional to the square root of the diffusion time. According to Boltzmann this holds as long as the diffusion is sorption-controlled.⁹¹ The diffusion coefficient of β -carotene can be calculated from the slope of the linear range of this curve. Within the time interval from 200 to 400 s its value at a depth of 25 μm inside the membrane is given by $1.4 \pm 0.092 \times 10^{-8} \text{ cm}^2/\text{s}$. The linear range of the curve ends when a steady state of diffusion is reached. From this time on, the lag-time t_{lag} , the concentration of β -carotene at the given depth in the membrane remains constant, there it is saturated. A uniform concentration gradient between the membrane border on the donor site and the given point inside the

membrane has been formed.

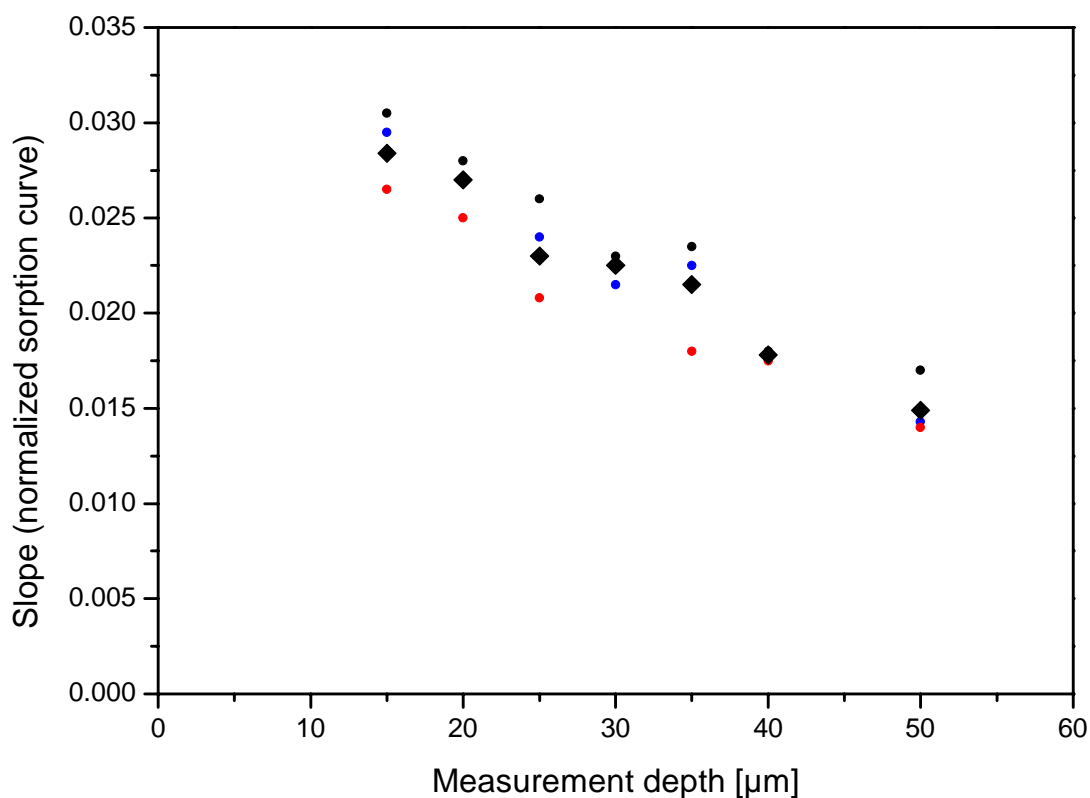


Fig. 5.3. Slope of various normalized sorption curves plotted as a function of the measurement depth (filled circles: 3 independent measurement series; filled squares: mean value of 3 independent measurements).

In Fig. 5.3 the slope of the linear range of various normalized sorption curves (see Fig. 5.2) is plotted as a function of the measurement depth. A dependency of these slope values from the measurement depths can be observed as the system has not yet reached a steady state. As soon as the diffusion through the membrane has reached its steady state this dependency can no longer be observed since a constant concentration gradient has been built up across the hole membrane.⁹² At the beginning of the diffusion process β -carotene molecules can be found only in the upper layer of the membrane directly adjacent to the donator cell containing a saturated solution of β -carotene in DMSO. The thickness of this layer is very small and the β -carotene gradient very steep. With increasing diffusion time the β -carotene molecules are getting deeper inside the membr-

ane towards the acceptor side (see Fig. 5.4). As long as no steady flux across the membrane is reached the slope of the concentration gradient at a given point inside the membrane decreases with increasing diffusion time until the slope of the gradient observed for the steady flux is reached (see Fig. 5.4).

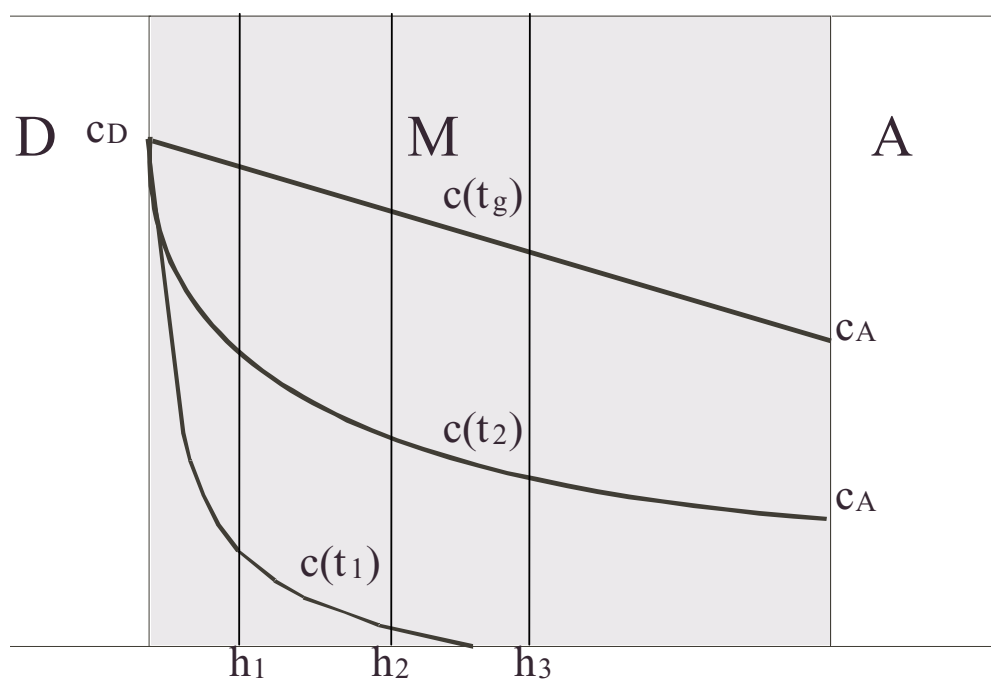


Fig. 5.4. Concentration gradient inside the membrane for various times (D = donator phase; M = membrane; A = acceptor phase; c_D = concentration of donator; c_a = concentration of acceptor; h_{1-3} = measurement points inside the membrane; $c(t_g)$ = concentration gradient at steady state conditions; $c(t_{1,2})$ = concentration gradient at time $t = 1, 2$ (with $t_1 \ll t_2 < t_g$).

Figure 5.5 shows concentration gradients of β -carotene in PDMS membranes. In seven independent test series they have been determined during permeation measurements under steady flux conditions. According to Fick's first law the amount of a substance diffusing per time unit through a membrane is proportional to its concentration gradient. As the mass flow of β -carotene through PDMS membranes is extremely low (diffusion coefficient = $1.4 \pm 0.092 \times 10^{-8} \text{ cm}^2/\text{s}$) the observed concentration gradient is very small.

Furthermore, in analogy to the high n-octanol/water partition coefficient ($\log K_{o/w} = 17.6$) the solubility of β -carotene in PDMS membranes is very high but rather poor in DMSO. When measurements are performed at points deeper inside the membrane an enlargement of the focus occurs.^{72,73} This results in a greater and more diffuse sample volume. In consequence the dispersion of the concentration values determined at higher measurement depths increases (see Fig. 5.5).

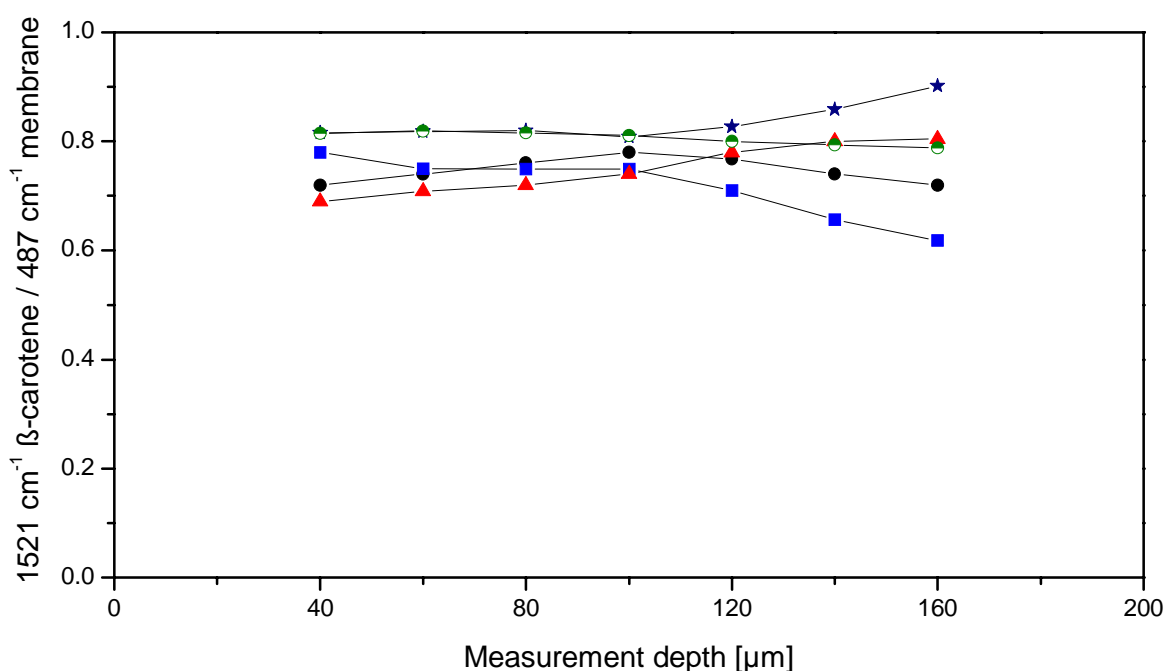


Fig. 5.5. Concentration gradient of β -carotene in PDMS membranes under steady flux conditions for seven independent test series.

5.3. Conclusion

We have applied confocal Raman spectroscopy to investigate the kinetics of diffusion processes through PDMS membranes before reaching steady state conditions. Conventional methods used so far to study diffusion processes across membranes determine rate and extent (dm/dt) by which a substance is released from the membrane under steady state conditions. The application of the confocal Raman spectroscopy offers the opportunity to observe the dynamics of a diffusion process at well-defined po-

ints inside the membrane. As shown in this chapter before reaching steady state conditions of diffusion the formation of a concentration gradient at a specific point inside the membrane can be observed. By determining changes in the intensity of characteristic peaks or even shifts of their wavenumber, changes in the concentration or the structure of the permeating substances or the membrane can be seen. As an example we investigated the diffusion of β -carotene dissolved in DMSO through a PDMS membrane. β -carotene is especially suited for this experiment since our Raman excitation laser was resonant with an electronic absorption of β -carotene. This results in a strong intensity enhancement of the observed Raman signal. Therefore even low concentrations of β -carotene can be detected. We determined the diffusion rate as a function of the measurement depth and diffusion time. We could show that at a given time before reaching a steady flux the slope of the concentration gradient, which is proportional to the rate and extent of diffusion, decreases with increasing penetration depth. In addition the concentration gradient under a steady flux has been investigated. According to the very low mass flow of β -carotene through the membrane only a small gradient can be observed. Our measurements have shown that the confocal micro Raman technique is a powerful tool to investigate the kinetics of diffusion processes within a membrane before the steady state has been reached. By utilizing the resonance Raman effect even low concentrations of the permeating substance can be detected. This offers the possibility to investigate the diffusion properties e.g. of pharmaceutical relevant molecules through membranes by using a tunable laser as Raman excitation laser and adjusting its wavelength to be resonant with an electronic absorption of the investigated molecule. In the development of new therapeutic systems the availability of membranes with well-defined permeation properties is of utmost importance. For a straightforward realization of such controlled release systems the knowledge of diffusion or permeation properties of the investigated drug through test membranes is of great importance. Confocal resonance Raman spectroscopy can help to get direct insight into the diffusion process.

6

Spectroscopic investigations of copper and iron doped B_2O_3 - Bi_2O_3 glass systems

6.1. Structural investigations of copper doped B_2O_3 - Bi_2O_3 glasses with high bismuth oxide content

6.1.1 Introduction

Glasses based on Bi_2O_3 heavy-metal oxide have wide applications in the field of glass ceramics, layers for optical and electronic devices, thermal and mechanical sensor, reflecting windows, etc..⁹³ Oxide glasses containing transition metal ions, such as Cu^+ and Cu^{2+} for cuprate glasses, are of interest due to their possible applications in memory

switching devices.⁹⁴ Because of the small field strength of Bi^{3+} ions, bismuth oxide cannot be considered as network former, however, in combination with B_2O_3 , glass formation is possible in a relatively large composition range.⁹⁵ The large glass formation region in bismuthate glasses has been attributed to the high polarizability of the Bi^{3+} cation.⁹⁶ Cordoba et al.⁹⁷ investigated the xerogel-glass transition of 0.5%CuO- SiO_2 system and reported the presence of the isolated copper ions in the amorphous SiO_2 structure. It was also found⁹⁸ that in samples containing copper, the metal is mainly dissolved in the SiO_2 network, when the thermal treatment is carried out at low temperatures.

B_2O_3 is one of the most common glass former. According to Krogh-Moe⁹⁹ the structure of vitreous B_2O_3 consists of a random network of boroxol rings and BO_3 triangles connected by B-O-B linkages. Mozzi and Warren¹⁰⁰ found that the addition of other oxides causes a progressive change of the boron atom coordination from three to four and results in the formation of various cyclic units like diborate, triborate or tetraborate groups. At low modifier content the BO_4 units are grouped to form tetraborate units. By increasing the content of other oxides in borate glasses the BO_4 units are predominantly associated with diborate groups. At higher concentrations of the modifier, the formation of BO_3 units with non-bridging atoms is reported.¹⁰¹ Various borate and bismuthate structural units present in glasses based on B_2O_3 and Bi_2O_3 are illustrated in the Appendix.

The aim of the present study was to obtain by means of Raman and infrared spectroscopy specific data regarding the local structure of copper doped B_2O_3 - Bi_2O_3 glasses, the role played by copper ions on boron and bismuthate units as well as to evidence the change of B_2O_3 and Bi_2O_3 structural units induced in these samples by the heat thermal treatment applied at 575 °C for 10 hours. The interest for the investigated glass system is determined by the presence of two network forming oxides, the classical B_2O_3 and unconventional Bi_2O_3 . At the same time both boron and bismuth are known to have more than one stable coordination, i.e. boron triangles and tetrahedra and bismuth pyramidal and octahedral units (see Appendix). Furthermore, bismuth is able to form independent interconnected network of the borate groups.¹⁰²

6.1.2. Results and discussion

According to X-ray diffraction patterns, which do not reveal any crystalline phase, the as prepared samples are amorphous from a structural point of view. After heat treatment the sample with $x = 0.625$ remains amorphous, while in those with $x \leq 0.40$ two crystalline phases were detected: $\text{Bi}_4\text{B}_2\text{O}_9$ and $\text{Bi}_{24}\text{B}_2\text{O}_{33}$. In the sample with $x = 0.40$ almost only $\text{Bi}_4\text{B}_2\text{O}_9$ crystalline phase is occurring, while in the sample with $x = 0.07$ more than 90 % is represented by the $\text{Bi}_{24}\text{B}_2\text{O}_{33}$ phase.

The vibrational Raman and infrared spectra of the investigated bismuth-borate glasses with high bismuth content are dominated by bands associated to the structural units of the heaviest cation, Bi^{3+} . The Raman peaks due to the heavy metal oxides such as Bi_2O_3 , may be classified into four main sets,¹⁰³ denoted as: (1) low wavenumber Raman modes (less than 100 cm^{-1}), (2) heavy metal ion vibrations in the range $70\text{-}160 \text{ cm}^{-1}$, (3) bridged anion modes in the intermediate $300\text{-}600 \text{ cm}^{-1}$ region, (4) non-bridging anion modes at higher wavenumbers.

The micro-Raman spectra of the untreated glasses presented in Figs. 6.1 and 6.2 show peaks associated to the last three categories of vibrations which supports the network forming character of the bismuth oxide. It was found that Bi^{3+} cations are incorporated in glass networks as deformed $[\text{BiO}_6]$ groups^{57,104-106} and that the network of the bismuth cuprate glasses is built up only of $[\text{BiO}_3]$ pyramidal units.¹⁰⁷ An evidence for the existence of $[\text{BiO}_3]$ polyhedra in the untreated glasses structure is the appearance of a band around 840 cm^{-1} in the infrared spectra.¹⁰⁸ In infrared spectra of the untreated samples (Fig. 6.3) this band can be observed only at $x = 0.07$. Therefore, we assume that Bi^{3+} cations are incorporated in $[\text{BiO}_3]$ and $[\text{BiO}_6]$ groups only at very high Bi_2O_3 content. In the micro-Raman spectrum (Fig. 6.1) at $x = 0.07$ the peak centred at 135 cm^{-1} indicates that the Bi^{3+} cations take part in the glass network as $[\text{BiO}_3]$ and $[\text{BiO}_6]$ octahedral units. The other bands and shoulders present in the Raman spectra of glass samples in the spectral range between 200 and 700 cm^{-1} are due to the bridging anion modes. The bands at 320 , 472 and 584 cm^{-1} for the sample with $x = 0.07$ can be attributed to Bi-O-Bi vibrations, while the weak shoulder at 236 cm^{-1} is due to Bi-O vib-

rations.¹⁰³ At the same concentration, $x = 0.07$, the very weak band at 859 cm^{-1} and the shoulder from 1220 cm^{-1} were assigned to the symmetric stretching vibration of the B-O-B bridges and to the stretching vibration of the terminal B-O⁻ bonds of the pyroborate groups (Fig. 6.2).^{101,102}

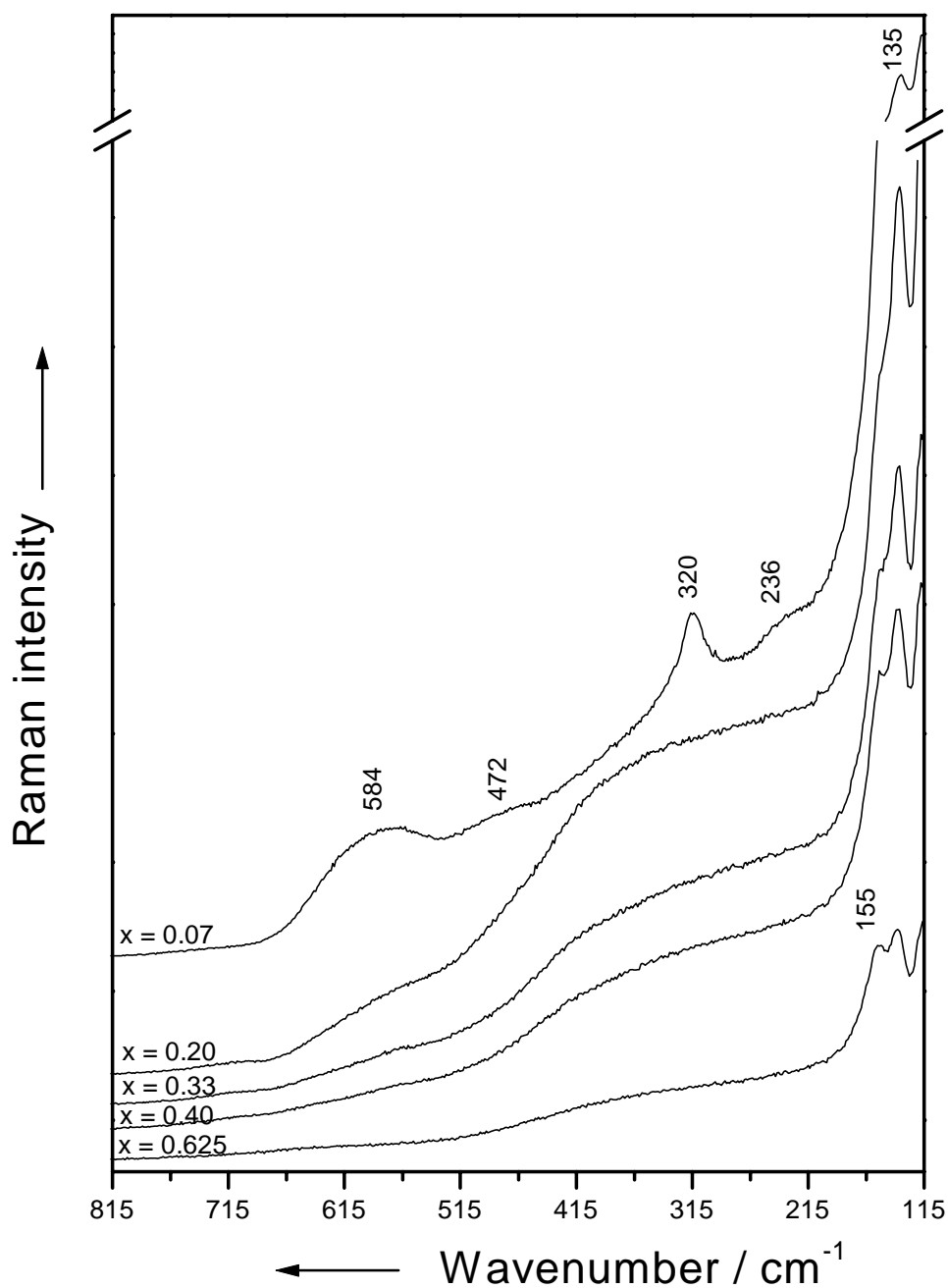


Fig. 6.1. Micro-Raman spectra of untreated $99.5\%[\text{x}\text{B}_2\text{O}_3(1-\text{x})\text{Bi}_2\text{O}_3]0.5\%\text{CuO}$ glasses in the $115\text{-}815\text{ cm}^{-1}$ spectral region.

The shoulders from 1323 and 1490 cm^{-1} appear only for very high Bi_2O_3 concentration. These two shoulders and the band around 1405 cm^{-1} can be assigned to B-O $\bar{\nu}$ vibrations of the units attached to large segments of the borate network.^{101,102} A similar behavior, a decreasing of the Raman band intensities in the 1300-1500 cm^{-1} spectral region with the increasing of the B_2O_3 content, has been observed in previous studies.^{102,109}

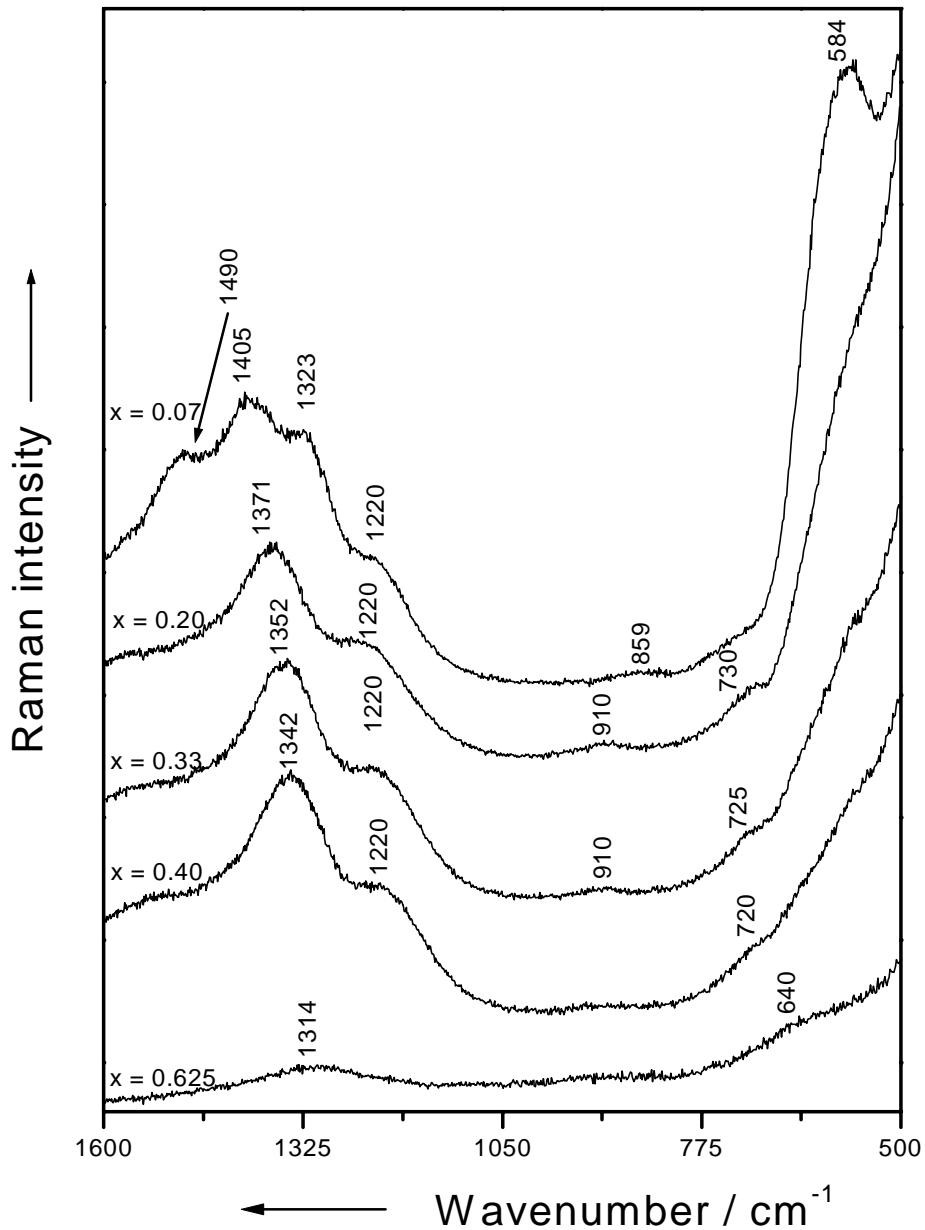


Fig. 6.2. Micro-Raman spectra of untreated 99.5% $[xB_2O_3(1-x)Bi_2O_3]0.5\%CuO$ glasses in the 500-1600 cm^{-1} spectral region.

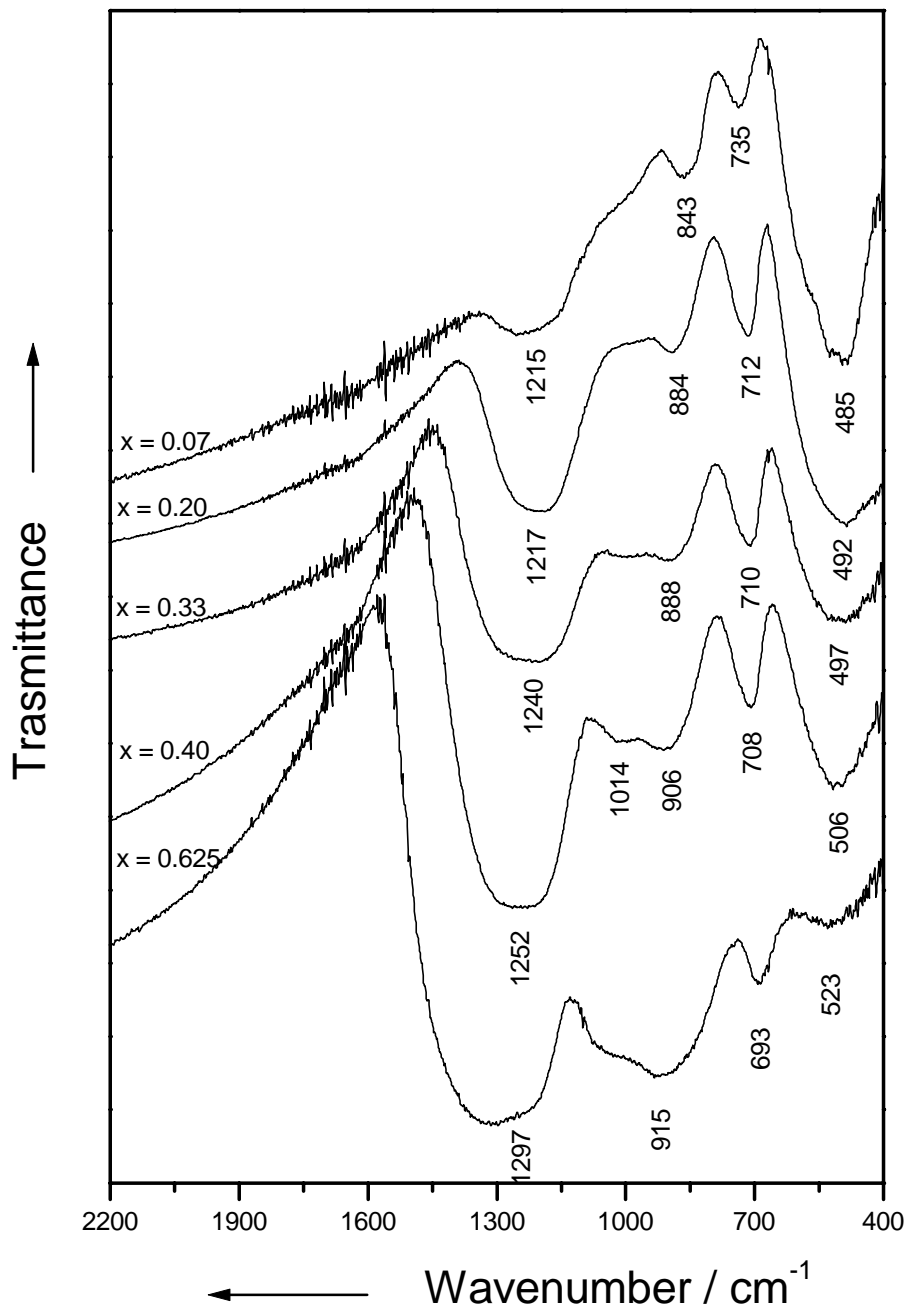


Fig. 6.3. Infrared spectra of untreated 99.5% $[xB_2O_3(1-x)Bi_2O_3]0.5\%CuO$ glasses.

In the investigated compositional range one remarks that the band from 1405 cm^{-1} exhibits a strong dependence on the Bi/B ratio. This band is strongly shifted to smaller wavenumbers as x increases (see Fig. 6.4). This dependence denotes the large structural influence of Bi_2O_3 on the B_2O_3 structure. For $x \geq 0.20$ a very small and broad band at

910 cm^{-1} , ascribed to orthoborate vibration, appears. By infrared spectral studies on $\text{Bi}_2\text{O}_3\text{-CuO}$, $\text{B}_2\text{O}_3\text{-PbO-CuO}$, $\text{Bi}_2\text{O}_3\text{-SrO-CuO}$, $\text{Bi}_2\text{O}_3\text{-SrO-CaO-CuO}$, Dimitriev and Mihailova¹⁰⁸ have related the shift of the band from 485 to 523 cm^{-1} to the change of the local symmetry in $[\text{BiO}_6]$ polyhedra, as the Bi_2O_3 content decreases. A similar effect due to the distortion of the bismuth polyhedra is observed in our infrared spectra (Fig. 6.3) and it is confirmed by the micro-Raman spectra (Fig. 6.1), where the mentioned distortion of the $[\text{BiO}_6]$ groups is revealed by the evolution of a band recorded at 155 cm^{-1} , which appears only as a shoulder in spectra of the samples with high bismuth content.

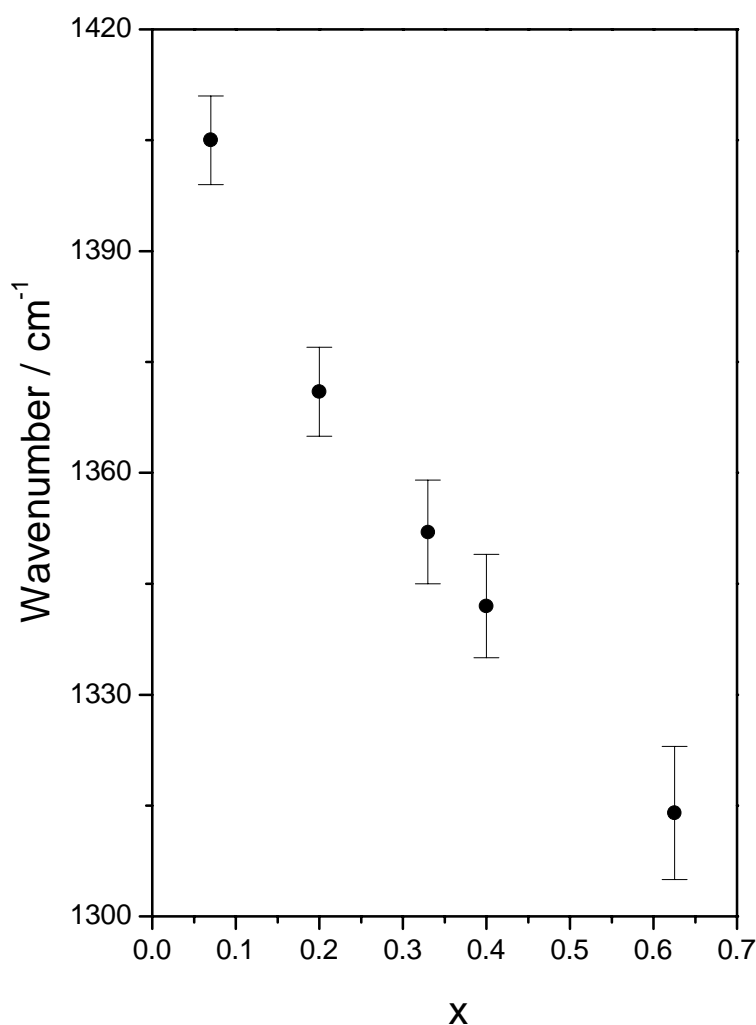


Fig. 6.4. The shift of micro-Raman band position of B-O^- vibration in function of B_2O_3 content for $99.5\%[\text{x}\text{B}_2\text{O}_3(1-\text{x})\text{Bi}_2\text{O}_3]0.5\%\text{CuO}$ glasses.

It is known¹⁰² that the width of the Raman bands in disordered materials is a measure of the disorder in the structure. Therefore, we can conclude that in the composition range with lower Bi₂O₃ content, where the bands are much larger, the disorder degree in the vitreous structure of the bismuth-borate glasses is much higher. The peaks existing at 135 and 155 cm⁻¹ evidence the presence of Bi³⁺ ions in the glass network. Having in view that the bismuth group vibrations appear at significantly smaller wavenumbers in comparison with the boron units vibrations, we can assume that in the 120-650 cm⁻¹ spectral region of the Raman spectra, only bismuth unit vibrations as bridged anion and angularly cation-anion-cation constrained modes appear. Thus, the broad shoulders centred around 390 and 580 cm⁻¹ are given by Bi-O and Bi-O-Bi vibrations in distorted linked [BiO₆] polyhedra.¹⁰³ The new weak shoulder around 730 cm⁻¹ could be assigned to chain metaborate group vibration.¹⁰⁹

The band at 735 cm⁻¹, present in the spectra of the untreated sample with $x = 0.07$, can be observed in the infrared spectra at all concentrations (Fig. 6.3). This band shifts to 693 cm⁻¹ for $x = 0.625$ and is assigned to B-O-B bending vibrations.¹¹⁰ The infrared band that appears at 884 cm⁻¹, for $x = 0.20$, is attributed to BO₃ triangular unit vibrations.¹¹⁰ At all concentrations, the infrared spectra of the untreated samples show in the spectral range between 1200 and 1500 cm⁻¹ bands assigned to the vibration of the B-O⁻ bonds from isolated pyroborate groups.¹¹⁰ Having in view that these bands become more intense and broader as the Bi₂O₃ content decreases we suppose that other B-O or B-O-B vibrations are also involved in this spectral region.

The features present in the micro-Raman and infrared spectra of the heat-treated samples (Figs. 6.5-6.7) for several Bi/B ratios, $0.07 \leq x \leq 0.33$, are reflecting the crystalline structure of these samples. The micro-Raman spectra of the treated samples (Fig. 6.5 and 6.6) for $x \leq 0.33$ consist of distinguished bands, most of them arising from the same vibration as those identified in the spectra of the untreated samples. As we already mentioned for the untreated glasses, the Bi³⁺ cations are usually incorporated in the glass network as [BiO₆] groups and the presence of a band around 843 cm⁻¹ in the infrared spectra shows the existence of the [BiO₃] polyhedra.^{57,104-107} Due to the fact that this band can be also observed in the infrared spectra of heat-treated samples (Fig. 6.7)

for $x \leq 0.33$, we have considered that both $[\text{BiO}_6]$ and $[\text{BiO}_3]$ groups built up the structure at all these concentrations.

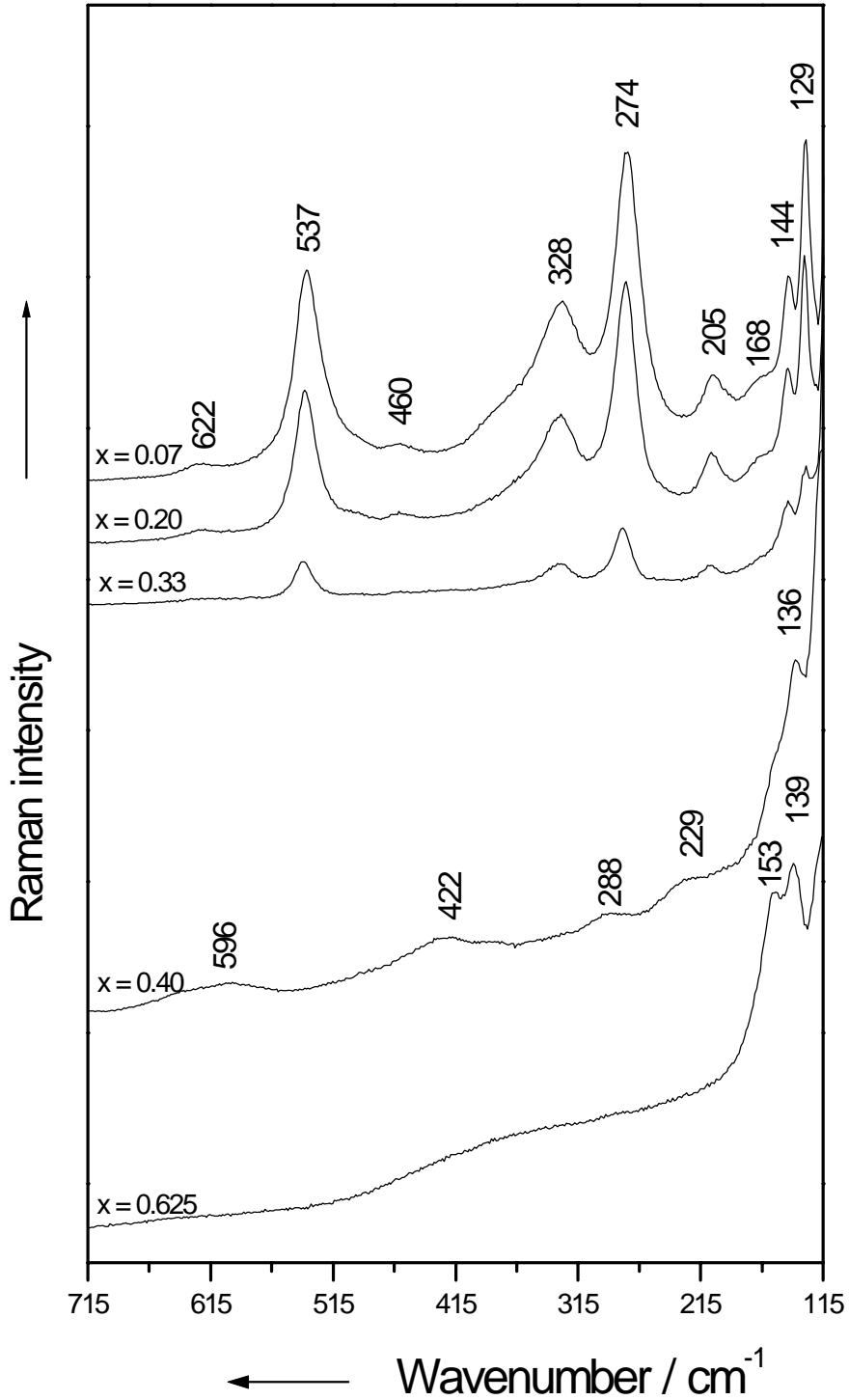


Fig. 6.5. Micro-Raman spectra of heat-treated $99.5\%[xB_2O_3(1-x)Bi_2O_3]0.5\%CuO$ glasses in the $115-715\text{ cm}^{-1}$ spectral range.

The new intense Raman bands at 144, 205, 274 and 537 cm^{-1} are related with the well developed crystalline phase $\text{Bi}_{24}\text{B}_2\text{O}_{39}$ that is present in the treated samples with $x \leq 0.33$. The first two bands indicate that Bi^{3+} cations are incorporated in the sample structure as $[\text{BiO}_3]$ pyramidal and $[\text{BiO}_6]$ octahedral units, while the last two ones are due to Bi-O vibrations.¹⁰³ Their high intensities are caused by the strong polarization effect given by the bismuth ions, which are highly polarizable.

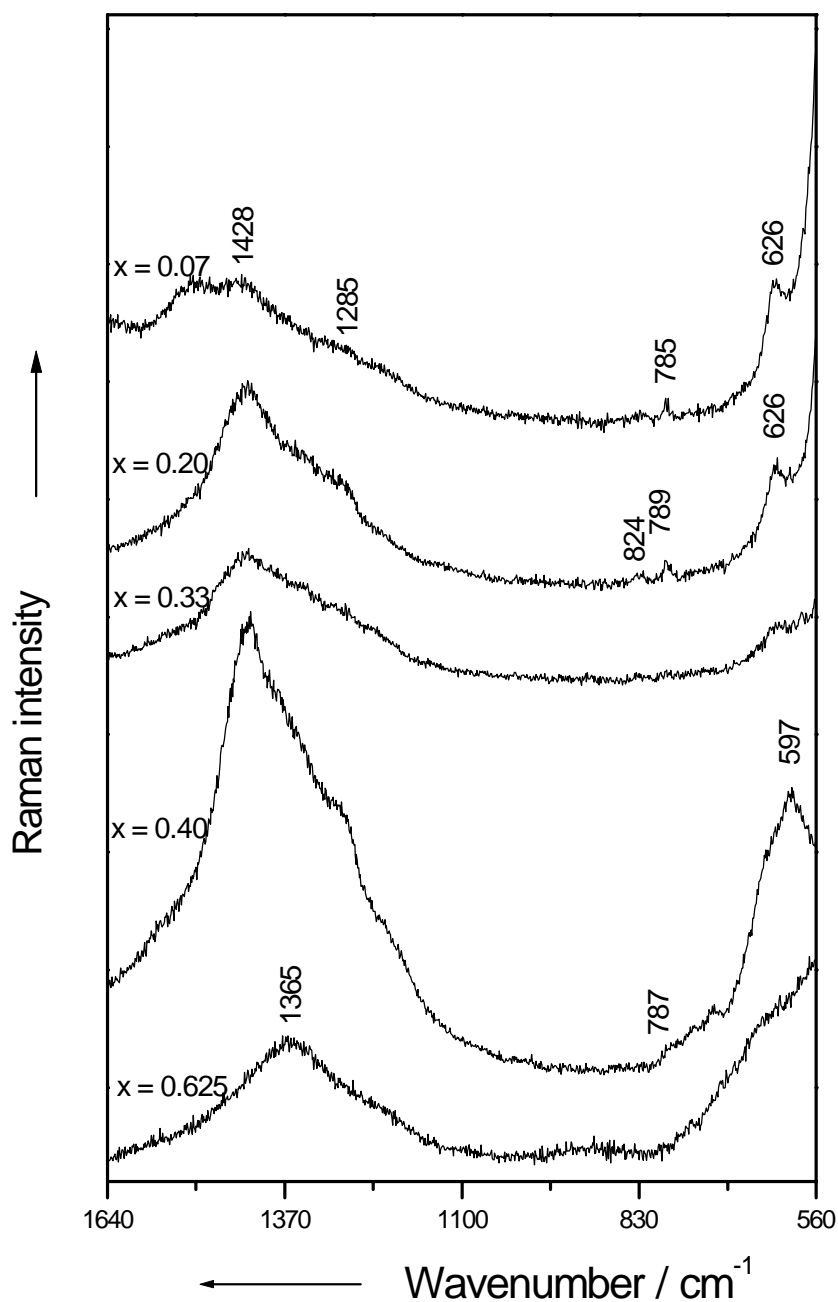


Fig. 6.6. Micro-Raman spectra of heat-treated $99.5\%[xB_2O_3(1-x)Bi_2O_3]0.5\%CuO$ glasses in the $560\text{-}1640\text{ cm}^{-1}$ spectral range.

A careful analysis of the micro-Raman spectra recorded for the samples with $x = 0.07$ before and after heat treatment (Figs. 6.1 and 6.5) suggests that in untreated samples germs of $\text{Bi}_{24}\text{B}_2\text{O}_{39}$ crystalline phase are also developed but these are small enough to become undetected by X-ray diffraction.

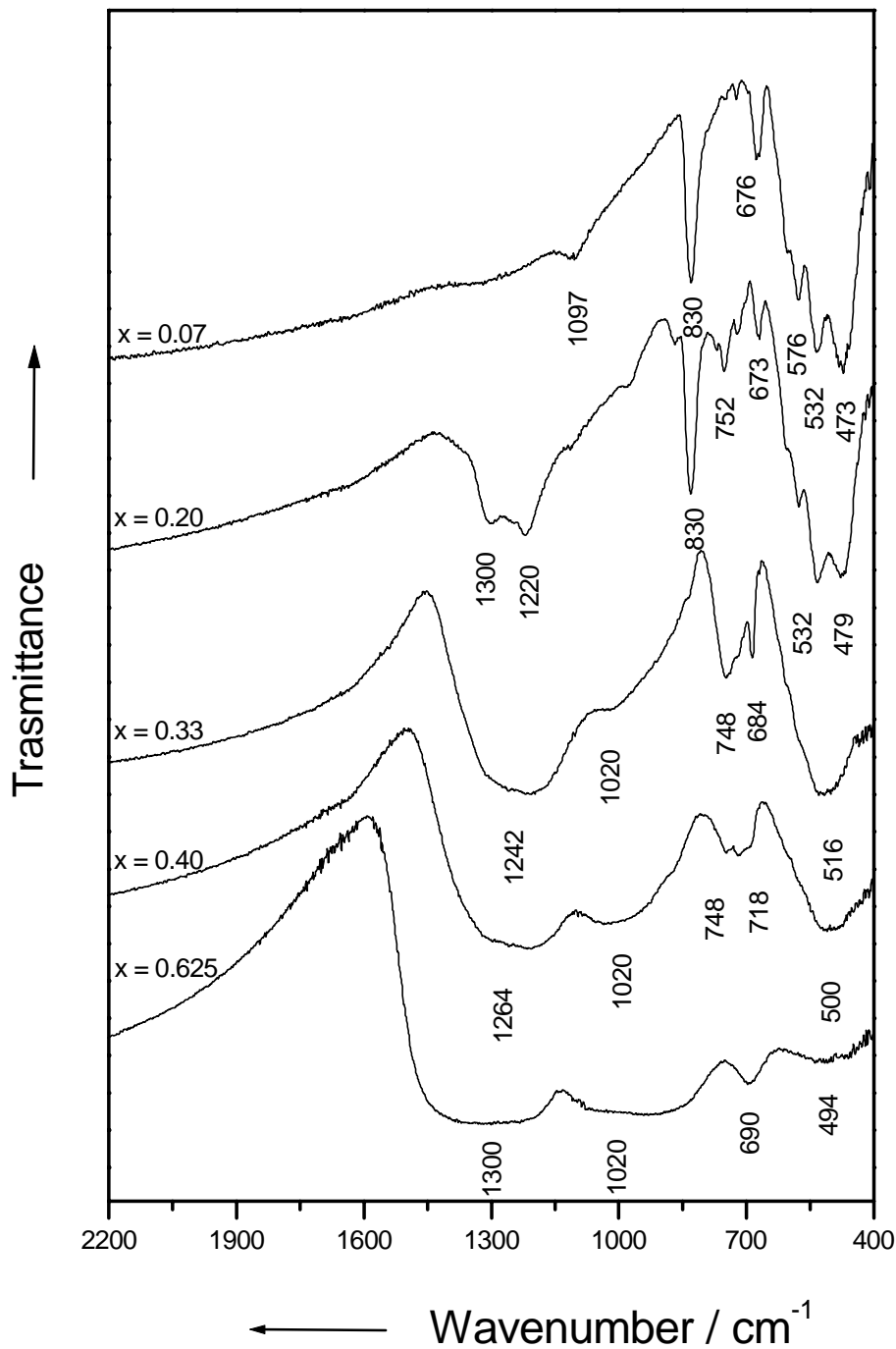


Fig. 6.7. Infrared spectra of heat-treated $99.5\%[\text{x}\text{B}_2\text{O}_3(1-x)\text{Bi}_2\text{O}_3]0.5\%\text{CuO}$ glasses.

For $x \geq 0.40$ the bismuth occurs only as six coordinated. In this case the $[\text{BiO}_6]$ polyhedra are still very distorted, as evidenced both in micro-Raman and infrared spectra (Figs. 6.5-6.7) by the broadening of all bands and their strong shift. The distortion of the $[\text{BiO}_6]$ polyhedra as boron content increases ($x \geq 0.33$), even in the heat treated samples, is reflected by the replacing of the infrared bands from 479 and 532 cm^{-1} with a band centred around 516 cm^{-1} . The last band can be considered like the convolution of the previous two bands. Concerning the boron atoms, the chain metaborate group that gives the band around 626 cm^{-1} appears in the Raman spectra already at $x = 0.07$ and proves the existence of a much more linked boron-oxygen structure than in untreated glass sample. The BO_4 unit vibrations¹¹⁰ are observable for all heat-treated samples in the spectral range between 900 and 1100 cm^{-1} of the infrared spectra (Fig. 6.7). The appearance of a breathing vibration of rings containing both BO_3 triangles and BO_4 tetrahedra^{101,109} as a very small Raman band around 785 cm^{-1} at $x = 0.07$ (Fig. 6.6) confirms our assumption that even for very high Bi_2O_3 content, the boron atoms in the treated samples structure are three and four coordinated. This result is in agreement with recent NMR data.¹¹¹ In the infrared spectra of the treated samples, the band at 748 cm^{-1} appears only for $x \leq 0.40$ and presents an increase in intensity at $x = 0.33$. This band can be assigned to the B-O-B bending vibration.¹¹⁰ At all concentrations, both micro-Raman and infrared spectra of the treated samples (Figs. 6.6 and 6.7) show in the range 1200-1500 cm^{-1} bands assigned to vibrations of the B-O⁻ bonds from borate and isolated pyroborate groups. As we already mentioned in the case of the untreated samples, the increase in intensities and the broadening of the infrared bands in the 1200-1500 cm^{-1} spectral region with the decreasing of the Bi_2O_3 content could be a consequence of the presence of other vibrations in this spectral range. In the micro-Raman spectra of the heat-treated samples (Fig. 6.6), the bands that arise in the above mentioned spectral region and are assigned to B-O⁻ vibrations of the units attached to large segments of the borate network^{101,102} increase appreciably in intensity at $x = 0.40$, when a high disorder degree dominates the structure. At the same concentration the increase in intensity and the broadening of the Raman band around 600 cm^{-1} can be assigned to the new formed Bi-O⁻ vibrations.¹⁰³ All these much larger bands as well as the behavior of the B-O-B bending vibrations from the spectra of the samples with $x = 0.33$ and 0.40 (Figs. 6.6 and 6.7) show that the crystalline phase

$\text{Bi}_4\text{B}_2\text{O}_9$, preponderantly for these samples, is more distorted and less ordered than $\text{Bi}_{24}\text{B}_2\text{O}_{39}$ phase, particularly for the samples with higher bismuth content.

As it was already mentioned, the Bi^{3+} cations are usually incorporated in the glass network as deformed $[\text{BiO}_6]$ groups, while only the $[\text{BiO}_3]$ polyhedra built up the network of the bismuth cuprate glasses.¹⁰⁷ Therefore, we assume that in the investigated glass system, despite the fact that the CuO content is very small, the presence of copper ions influences the bismuth structural units favourizing the formation of $[\text{BiO}_3]$ units for untreated glasses with $x = 0.07$ and for treated glasses with $x \leq 0.33$.⁵⁵

6.1.3. Conclusion

Raman and infrared spectral investigations of $99.5\%[xB_2O_3(1-x)\text{Bi}_2O_3]0.5\%\text{CuO}$ system evidence that Bi^{3+} cations are incorporated in the glass network as $[\text{BiO}_3]$ pyramidal and $[\text{BiO}_6]$ octahedral units for $x = 0.07$ and as distorted $[\text{BiO}_6]$ polyhedra for $0.20 \leq x \leq 0.625$. Raman and infrared spectra of samples after heat treatment show first of all that the glass stability is decreasing as bismuth content increases. After 10 hours heat treatment at 575°C , only the sample with highest boron content, $x = 0.625$, remains non-crystalline while all the others partially crystallize. The presence of copper ions influences the bismuth surrounding, favourizing the formation of $[\text{BiO}_3]$ units for untreated glasses with $x = 0.07$ and for treated samples with $x \leq 0.33$. The boron atoms in the heat-treated samples are three and four coordinated even for very high Bi_2O_3 content. On the other hand, a strong disordering effect of Bi_2O_3 on the vitreous B_2O_3 network is evidenced.

6.2. Spectroscopic investigations of highly iron doped B_2O_3 - Bi_2O_3 glasses

6.2.1 Introduction

Raman and infrared spectroscopy have proven to be powerful and effective tools for characterizing the structure of local arrangements in glasses.¹¹²⁻¹¹⁴ Glasses containing bismuth have received increased attention due to their manifold possible applications. Recently, optical Kerr shutter (OKS) switching and degenerated four-wave mixing experiments have been performed on glasses based on Bi_2O_3 - B_2O_3 using femtosecond lasers and it was found that these glasses exhibit an ultrafast response in OKS operation. Furthermore, it was indicated that erbium doped bismuth based glass is suitable for broadband amplifiers and highly doped short length fiber applications for metro use.¹¹⁵ It was also reported that heavy metal oxide glasses containing bismuth have been investigated for possible use in scintillation detectors for high-energy physics and that the large polarizability of bismuth makes it suitable for possible non-linear optical uses and environmental guide-lines.¹¹⁶ X-ray and infrared studies on B_2O_3 - Bi_2O_3 conventional glass have shown that Bi^{3+} ions participate in the network structure above 45 m% Bi_2O_3 .¹¹⁷ Dumbaugh¹¹⁸ has investigated non-conventional glasses using Bi_2O_3 as the basis of the glass network of multi-component systems. It was observed that the addition of Th, Cd, Ba, Zn, and Fe oxides results in a large glass formation domain.

Borate glasses have been the subject of intense structural studies by various physical and chemical methods including Raman and infrared spectroscopy, Brillouin experiments, NMR and neutron scattering investigations.^{55,119-123} It was reported that the addition of a network modifier in borate glasses could produce the conversion of the triangular BO_3 structural units to BO_4 tetrahedra with a coordination number of four or to the formation of non-bridging oxygen atoms.^{55,121} In fact, these BO_4 structural units are incorporated in more complex cyclic groups such as triborate B_3O_7 , di-triborate B_3O_8 , metaborate B_3O_9 and more complicated units (see Appendix). In a relative recent study optical and physical properties of bismuth borate glasses over wide compositional

range from 0 to 88 mol % Bi_2O_3 have been investigated and an opening of the glasses structure with the increase of the Bi_2O_3 concentration has been observed.¹¹⁴

Because iron is frequently present in trace amounts as an impurity introduced with the raw materials, various studies have been carried out to establish the environments of Fe^{2+} and Fe^{3+} ions, mostly at the few percent level in different glasses.¹²⁴⁻¹²⁶ It was supposed that, at low concentrations, the ions act as modifiers similar to the alkali metals or alkaline earths.¹²⁴ In order to find new applications of the doped Bi_2O_3 - B_2O_3 glasses a better understanding of their structure becomes necessary.

In this section Raman and infrared spectroscopy have been applied to the vibrational characterisation of the local structure of $95\%[\text{x}\text{B}_2\text{O}_3(1-\text{x})\text{Bi}_2\text{O}_3]5\%\text{Fe}_2\text{O}_3$ glasses. Our interest was to find out if the B_2O_3 and Bi_2O_3 matrices are influenced by the iron dopant and to evidence how B_2O_3 and Bi_2O_3 structural units are affected by the thermal treatment applied at 575 °C for 10 hours.

6.2.2. Results and discussion

According to X-ray diffraction analysis the as prepared samples are amorphous from a structural point of view. After heat treatment only samples with high bismuth content ($x \leq 0.20$) become crystalline. In the compositional range with high bismuth content at least two crystalline phases are expected to be developed, $\text{Bi}_4\text{B}_2\text{O}_9$ and $\text{Bi}_{24}\text{B}_2\text{O}_{39}$, however, in samples with $x \leq 0.20$ only the last one has been observed. The prepared sample with $x = 0.33$, having the composition corresponding to the $\text{Bi}_4\text{B}_2\text{O}_9$ phase, remained non-crystalline after 10 hours heat treatment at 575 °C, even though in bismuth-borate glasses from the same compositional range, but with low transitional metal content this crystalline phase has been developed after a similar heat treatment. These results show the stabilizing effect of iron on the bismuth-borate glass matrices in this relatively high doping content.

In order to identify clearly all structural changes, which appear at different compositions of the matrices, we separately analysed the infrared and Raman spectra of the samples with $x \leq 0.20$ (high Bi_2O_3 content) and $x \geq 0.30$, respectively.

(a) Untreated samples with $x \leq 0.20$

It was shown that Bi_2O_3 appears in the bismuth-borate glass networks as deformed $[\text{BiO}_6]$ groups,^{57,104} both $[\text{BiO}_6]$ and $[\text{BiO}_3]$ polyhedra^{55,127} or only as $[\text{BiO}_3]$ pyramidal units.¹⁰⁷ The most important condition for the existence of $[\text{BiO}_3]$ polyhedra is the presence of a band at 830 cm^{-1} in the infrared spectra.¹⁰⁴ The absence of this band in the infrared spectra of the untreated glasses (Fig. 6.8) proves that only $[\text{BiO}_6]$ octahedra build up the bismuthate structure of these samples.

For $x \leq 0.20$ all Raman spectra (Fig. 6.9) show peaks associated to the heavy metal ions vibration in the spectral range between 70 and 160 cm^{-1} , bridged anion modes in the $300\text{--}600 \text{ cm}^{-1}$ spectral range and non-bridging anion modes at higher wavenumbers¹⁰³ which supports the network forming character of bismuth. The peak at 82 cm^{-1} , clearly related to the heavy metal as Miller et al.¹²⁸ have demonstrated in a series of glasses containing different metal oxides, indicates more a “molecular-like” origin than an “acoustic-like” nature, because its position does not depend on the composition, and its intensity increases in the high bismuth content region. In the micro-Raman spectra for $x \leq 0.20$ (Fig. 6.9), the peak centred at 123 cm^{-1} and the shoulder at 152 cm^{-1} indicate the presence of the Bi^{3+} cations as $[\text{BiO}_6]$ octahedral units, while the bands at 262 and 516 cm^{-1} and the shoulder at 328 cm^{-1} are due to the symmetric stretching anion motion in angularly constrained cation-anion-cation configurations in $[\text{BiO}_6]$ polyhedra.¹⁰³ At these concentrations a large influence of the Bi_2O_3 on the B_2O_3 structure is evidenced by the missing of the isolated boron group vibrations in the $1200\text{--}1400 \text{ cm}^{-1}$ spectral range. The very weak shoulder around 620 cm^{-1} could be attributed to both the Bi-O stretching vibration (i.e. vibration of non-bridging oxygen) of the $[\text{BiO}_6]$ octahedral units¹⁰⁶ and to the metaborate vibration (chain and ring type).^{102,109} In this compositional range no other Raman bands given by the boron or iron unit vibrations were observed.

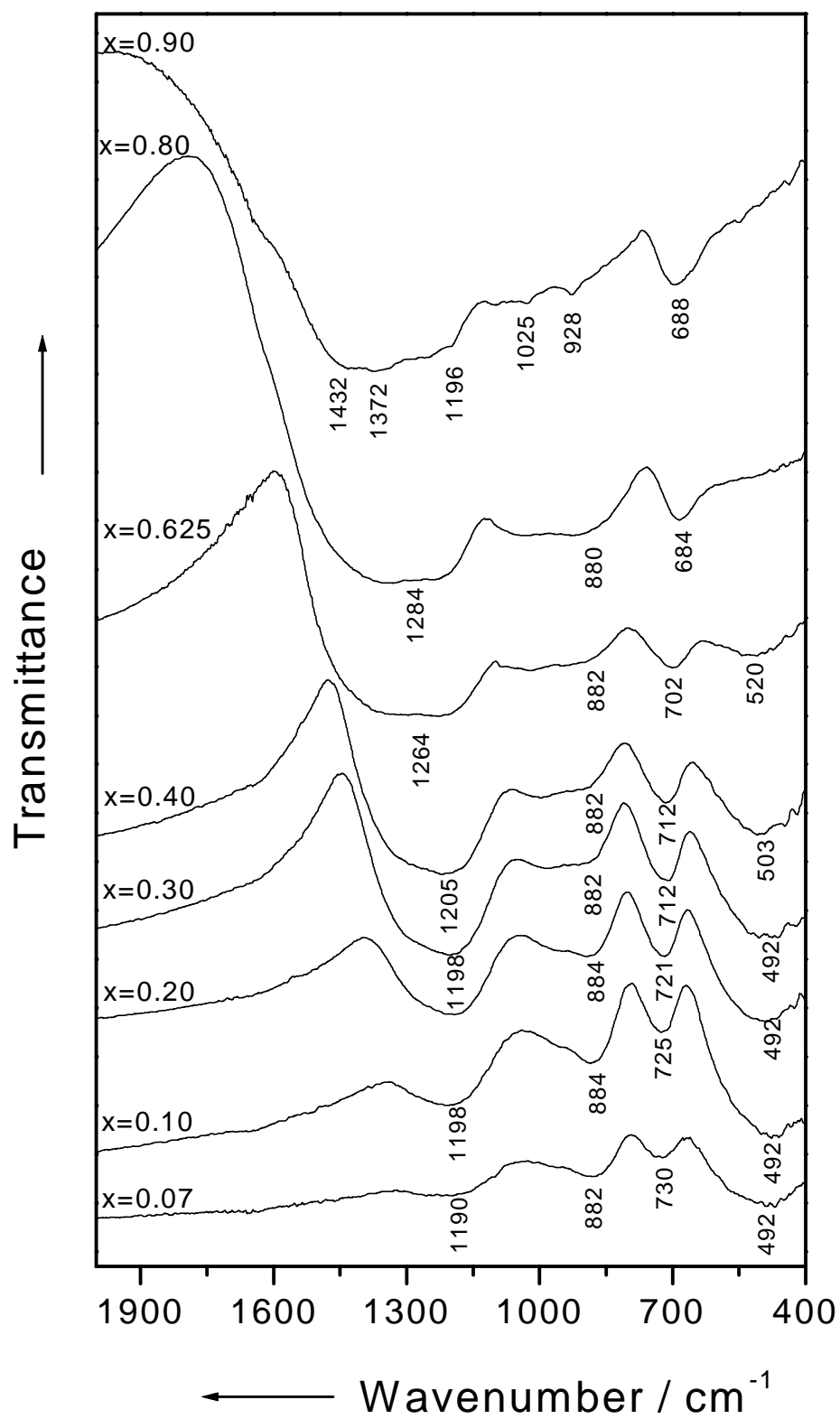


Fig. 6.8. Infrared spectra of untreated $95\%[xB_2O_3(1-x)Bi_2O_3]5\%Fe_2O_3$ glasses.

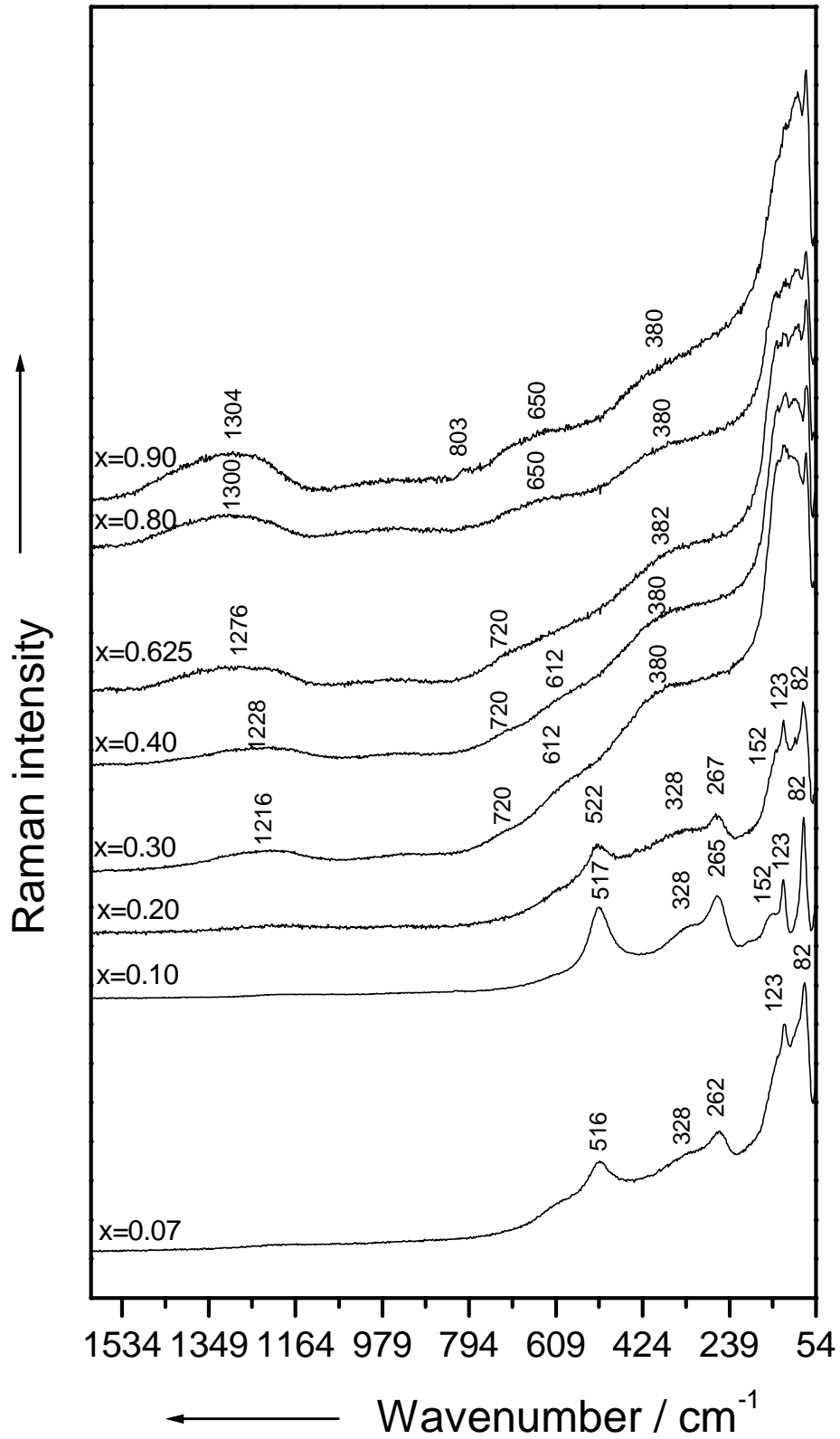


Fig. 6.9. Micro-Raman spectra of untreated 95% $[xB_2O_3(1-x)Bi_2O_3]$ 5% Fe_2O_3 glasses.

The infrared spectral range around 480 cm^{-1} (Fig. 6.8) is typical for the normal vibrations of $[\text{BiO}_6]$ groups.¹⁰⁵ The infrared band at 730 cm^{-1} due to a bond-bending motion of the B-O-B groups within the network¹¹⁰ is shifted to smaller wavenumbers with the decreasing of Bi_2O_3 content. This shift of the boron group vibrations proofs again the influence of the Bi_2O_3 on the formed B_2O_3 structure in these glasses. The weak infrared bands, which appear in the $800\text{-}1000\text{ cm}^{-1}$ spectral region, are most probably due to BO_3 or isolated diborate group vibrations. All infrared spectra for $x \leq 0.20$ present small bands around 1198 cm^{-1} , which increase in intensity as the Bi_2O_3 content decreases and were assigned to the stretching vibration of the B-O bond.¹¹⁰

(b) Untreated samples with $x \geq 0.30$

As we have already mentioned in the previous section the width of the Raman bands in disordered materials is a measure of the disorder in the structure.¹⁰² Having in view that in the compositional range with B_2O_3 content larger than 0.20 the Raman bands become broader (Fig. 6.9), we can conclude that the disorder degree in the vitreous structure of the bismuth-borate glasses increases. The Raman bands, which show the presence of the Bi^{3+} cations as $[\text{BiO}_6]$ octahedral units, raised in the $50\text{-}180\text{ cm}^{-1}$ spectral range, but the increasing of their half-width in comparison to the half-width of the corresponding bands for $x \leq 0.20$ make them, due to their convolution, not clearly distinguishable. The broadening of the bands and their shifts to higher wavenumbers, for $x \geq 0.30$, is a consequence of the appearance of highly distorted $[\text{BiO}_6]$ polyhedra. Thus, beginning with $x = 0.30$ a strong shift and a broadening of the shoulder at 380 cm^{-1} (328 cm^{-1} , at $x = 0.20$) given by Bi-O-Bi vibrations of the distorted $[\text{BiO}_6]$ octahedral units can be observed. The weak Raman shoulder at 620 cm^{-1} , which could be attributed to both the vibration of the Bi-O⁻ non-bridging oxygen¹⁰⁶ as well as to the metaborate vibration (ring and chain type)^{102,109}, increases in intensity as the Bi_2O_3 content decreases. One can see from Fig. 6.9 that beginning with $x = 0.30$ boron units vibrations appear as shoulders and bands around 720 and 1216 cm^{-1} , respectively. The shoulders are due to metaborate group vibrations, while the bands from the high wavenumber region are attributed to B-O⁻ vibrations, indicating the presence of non-bridging oxygen.^{102,109} In the investigated compositional range one can remark that the band at 1216 cm^{-1} exhibits

a strong dependence on the Bi/B ratio. This band is strongly shifted to higher wavenumbers as x increases. At $x = 0.90$ a new very weak Raman band arises at 803 cm^{-1} which is assigned to the symmetric breathing vibration of the boroxol rings.^{102,109} The appearance of this band indicates a much more linked boron structure in the glasses with low bismuth content.

The shift of the band from 492 to 520 cm^{-1} observed in the infrared spectra (Fig. 6.8) for $0.30 \leq x \leq 0.625$ is related to the change of the local symmetry in $[\text{BiO}_6]$ polyhedra.¹⁰⁴ Therefore, it can be emphasized again that bismuthate groups appear in the untreated sample with $x \geq 0.30$ as distorted $[\text{BiO}_6]$ polyhedra. For $x \geq 0.80$ the infrared band centred at 520 cm^{-1} disappears, a better linkage of the boron structural units occurring. The influence of the distorted $[\text{BiO}_6]$ polyhedra on the B_2O_3 structure is further evidenced by the shift of the infrared bands due to bending vibrations from 721 ($x = 0.20$) to 712 cm^{-1} ($x = 0.30$) and from 702 ($x = 0.625$) to 688 cm^{-1} ($x = 0.90$), respectively. The formation of a higher number of linked boron units is supported by the small increase of the infrared band intensities given by pentaborate group vibrations in the $900\text{-}1100\text{ cm}^{-1}$ spectral range¹¹⁰, beginning with $x = 0.30$. The intensity of the infrared band around 1198 cm^{-1} assigned to the B-O stretching vibration increases as the Bi_2O_3 content becomes smaller. At $x = 0.90$, the presence of the boroxol units is also evidenced in the infrared spectrum (Fig. 6.8) by the appearance of a shoulder at about 1432 cm^{-1} as it was related in a previous study.¹¹⁰

Taking into account the weak intensity of the infrared bands given by BO_3 and BO_4 units, the strong shift of the infrared B-O-B bending vibration and the very weak Raman intensity of the bands assigned to boroxol unit vibrations, which represent an important feature of the vitreous B_2O_3 , we can affirm that the distorted $[\text{BiO}_6]$ polyhedra induce a high influence on the boron network in the glass samples.

In a previous study⁵⁷ the influence of the Fe_2O_3 content on the bismuth-borate matrices in the $99.5\%[x\text{B}_2\text{O}_3(1-x)\text{Bi}_2\text{O}_3]0.5\%\text{Fe}_2\text{O}_3$ glasses was investigated by means of FT-Raman spectroscopy. By comparing the Raman spectra of the present untreated samples ($5\%\text{Fe}_2\text{O}_3$) with those of the previously studied glasses ($0.5\%\text{Fe}_2\text{O}_3$) at the correspondi-

ng concentrations one can see that with increasing of the Fe_2O_3 content some new bands appear, while others, attributed to Bi-O-Bi vibrations, present a decrease in half-width, especially for $x = 0.20$ (Figs. 6.9 and 6.10).

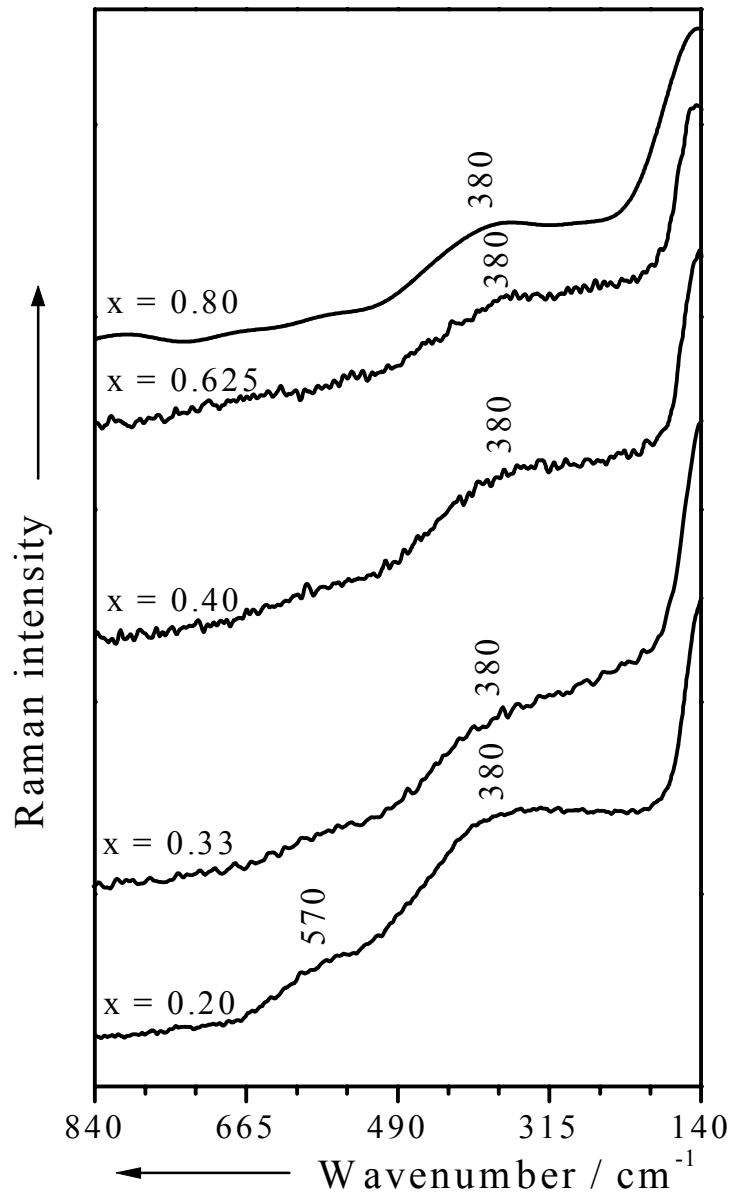


Fig. 6.10. FT-Raman spectra of $99.5\%[x\text{B}_2\text{O}_3(1-x)\text{Bi}_2\text{O}_3]0.5\%\text{Fe}_2\text{O}_3$ glasses.

This result can be interpreted as the influence of the Fe_2O_3 on the structure of bismuth-borate matrices, a more ordered bismuthate structure occurring in the compositional region with relatively high bismuth content ($x = 0.20$).

(c) Treated samples with $x \leq 0.20$

When analysing the Raman and infrared spectra of these samples one has to keep in mind that they are crystalline and $\text{Bi}_{24}\text{B}_2\text{O}_{39}$ is the only crystalline phase identified. Therefore, we expected that the spectra of these three samples to be very similar and this is indeed the case.

As already mentioned a precondition for the existence of the BiO_3 polyhedra in the Bi_2O_3 glass structure is the presence in the infrared spectrum of a band at 830 cm^{-1} . This band is related to the symmetrical stretching vibration of the Bi-O bonds in the $[\text{BiO}_3]$ groups.¹⁰⁴ A similar band along with two others at 600 and 470 cm^{-1} were also observed by Zheng et. al.¹²⁷ in the spectra of Bi-Ca-Sr-O glasses and the conclusion that both $[\text{BiO}_3]$ and $[\text{BiO}_6]$ groups exist in these glasses has been drawn. Taking into account that all above-mentioned features are present in the infrared spectra of the heat-treated samples (Fig. 6.11) in the analysed compositional range and most of the Raman bands appear at approximately the same wavenumbers as in the untreated Raman spectra for the corresponding concentrations (Figs. 6.9 and 6.11) we conclude that Bi^{3+} cations are present in the treated sample as $[\text{BiO}_3]$ and $[\text{BiO}_6]$ polyhedra, respectively. While the infrared bands at 830 and 470 cm^{-1} are due to totally symmetric stretching and bending vibrations, the bands that arise in the $530\text{-}620\text{ cm}^{-1}$ spectral range are assigned to doubly degenerate stretching vibrations of $[\text{BiO}_3]$ and $[\text{BiO}_6]$ polyhedra.¹⁰⁷ The weak band around 1200 cm^{-1} is attributed to the stretching vibration of the B-O bond and the band centred at 1400 cm^{-1} is given by B-O^- vibrations.¹¹⁰ The appearance of the latter band indicates the presence of the non-bridging oxygens, most probably in isolated pyroborate and orthoborate groups.

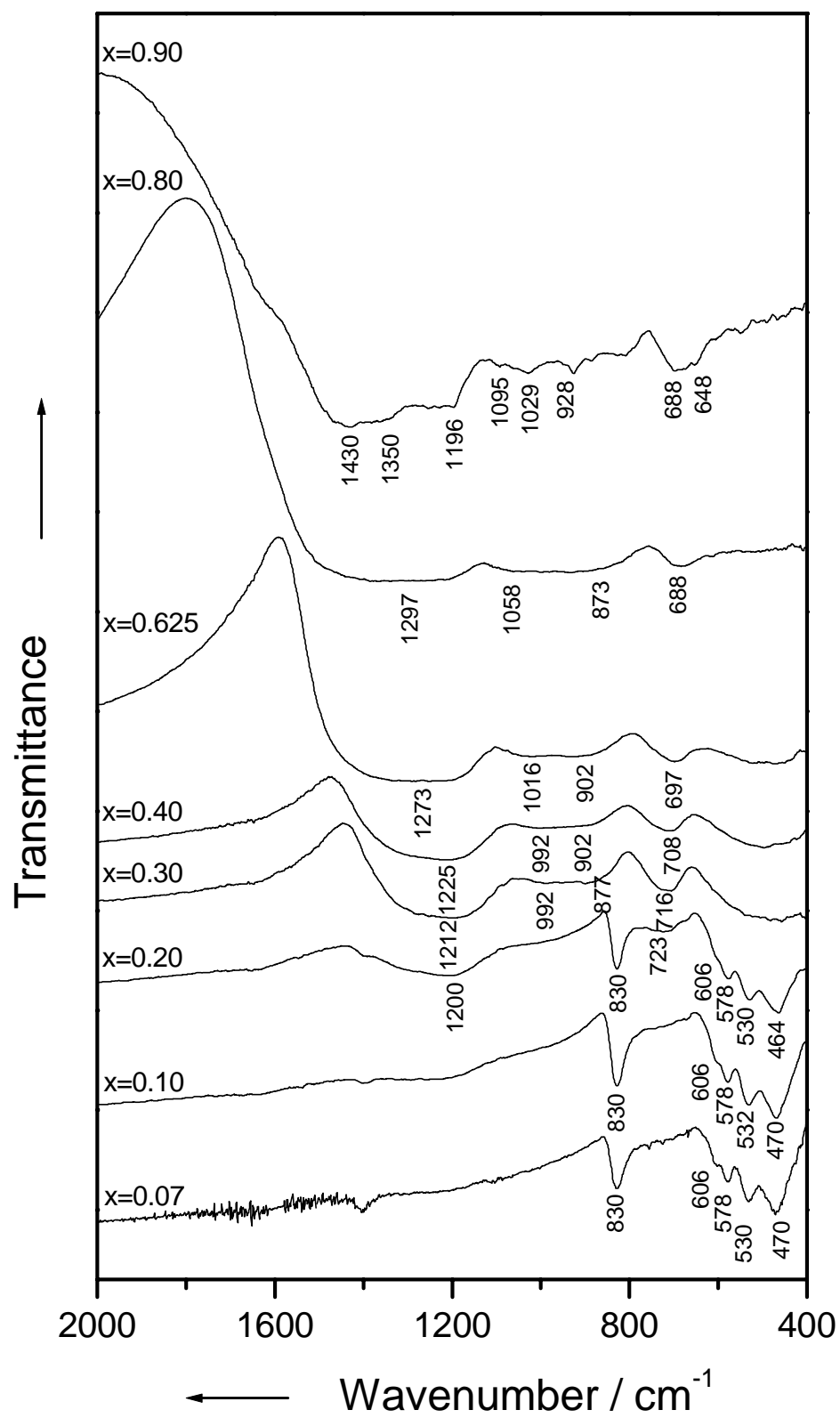


Fig. 6.11. Infrared spectra of heat-treated $95\%[xB_2O_3(1-x)Bi_2O_3]5\%Fe_2O_3$ glasses.

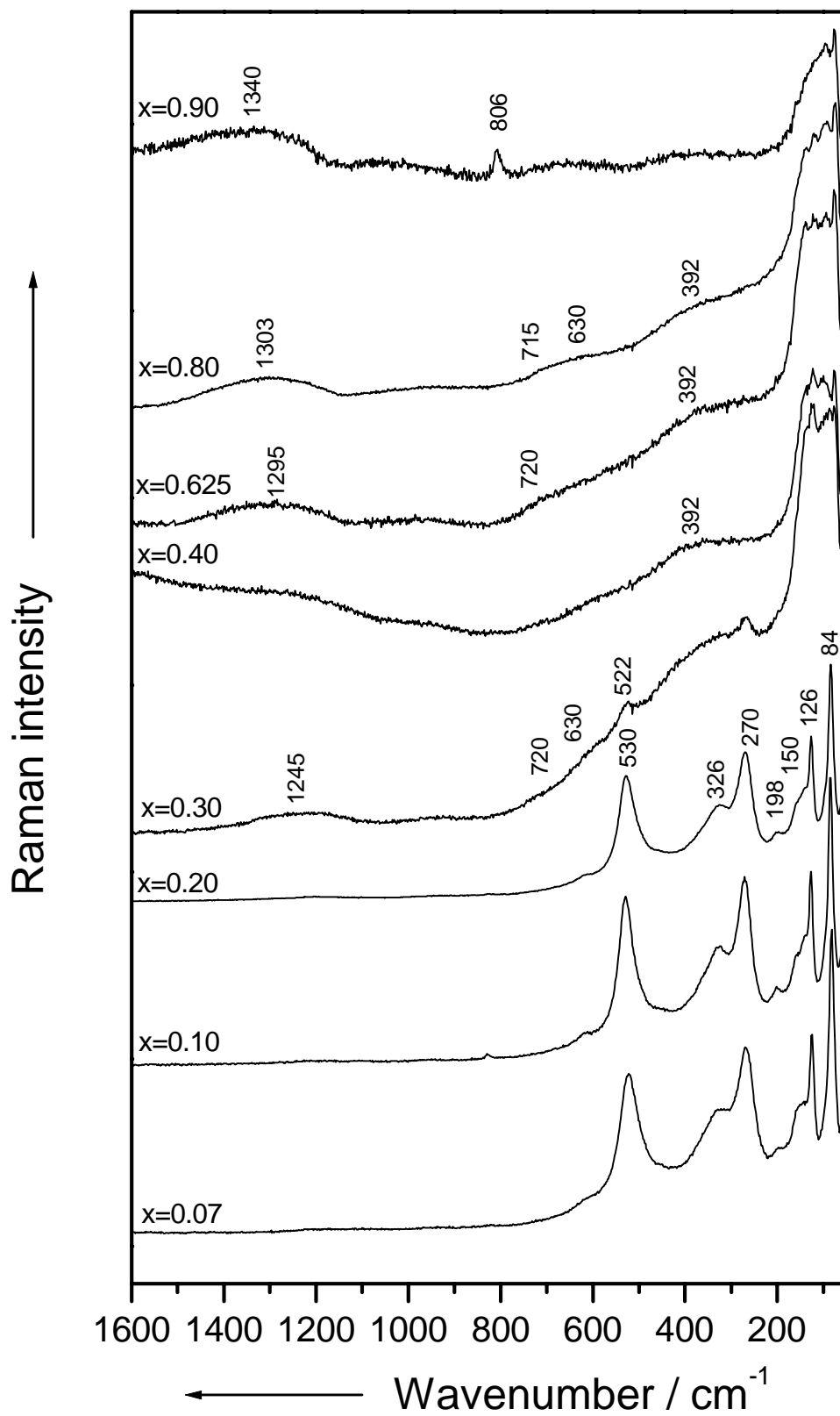


Fig. 6.12. Micro-Raman spectra of heat-treated $95\%[xB_2O_3(1-x)Bi_2O_3]5\%Fe_2O_3$ glasses

The micro-Raman spectra of the heat-treated samples (Fig. 6.12) are very similar with those of the untreated glasses. However, we should note that a new weak band at 198 cm^{-1} due to Bi-O-Bi vibration in $[\text{BiO}_3]$ and $[\text{BiO}_6]$ polyhedra appears.¹⁰³ All other Raman bands and shoulders at 84 , 126 and 150 cm^{-1} , which denote the presence of the Bi^{3+} cations as $[\text{BiO}_3]$ and $[\text{BiO}_6]$ polyhedra,¹⁰³ as well as the bands given by Bi-O-Bi stretching vibrations in the spectral range between 300 and 600 cm^{-1} appear at approximately the same position compared to the Raman bands of the untreated samples at the corresponding concentrations. One exception can be observed for the band centred at 530 cm^{-1} which is attributed to the Bi-O-Bi stretching vibration.¹⁰³ The shift from 516 cm^{-1} (untreated glass) to 530 cm^{-1} (treated sample) could be a consequence of the fact that in comparison to the untreated glass, where the Bi-O-Bi belong to the connected $[\text{BiO}_6]$ polyhedra, in the heat-treated sample the Bi-O-Bi could belong either to connected $[\text{BiO}_3]$ pyramidal units or to $[\text{BiO}_3]$ linked to $[\text{BiO}_6]$ polyhedra. This hypothesis is supported by the presence of this band at approximately the same value, 522 cm^{-1} , in the Raman spectrum for the sample with $x = 0.30$, where only $[\text{BiO}_6]$ polyhedra built up the bismuth oxide structure, as it was observed in the Raman spectrum of untreated glass for $x \leq 0.20$. The weak Raman shoulders arising around 620 cm^{-1} , could be assigned to both the vibration of the BiO^- non-bridging oxygen¹⁰⁶ as well as to the metaborate vibration (ring and chain type).^{101,102,109}

The decreasing of the half widths of the Raman bands of the treated samples in comparison to the corresponding half widths of the Raman bands of the untreated glasses denotes the influence of the thermal treatment, which favours the formation of a more ordered bismuthate structure.

(d) Treated samples with $x \geq 0.30$

The absence of the infrared band at 830 cm^{-1} in the infrared spectra of the treated samples in this compositional range (Fig. 6.11) shows that only $[\text{BiO}_6]$ octahedral units built up the bismuth structure. Beginning with $x = 0.30$ all infrared bands from 400 to 620 cm^{-1} are convoluted as a single very broad band. These changes can be interpreted as a strong distortion of the $[\text{BiO}_6]$ polyhedra. The increase in intensity of the band at

716 cm^{-1} assigned to the B-O-B bending vibration as the Bi_2O_3 concentration decreases evidences the formation of a much more linked boron structure. The strong shift to smaller wavenumbers of this infrared band with decreasing of the Bi_2O_3 content, for $x \leq 0.80$, demonstrates the strong influence of the bismuthate groups on the boron network structures even after heat treatment. Because no supplementary shift of this band can be observed at higher B_2O_3 concentrations ($x = 0.90$), and a new infrared band at 648 cm^{-1} due to a vibration in pentaborate group appears, we suppose that at this concentration a linkage of the boron structure occurs. The weak infrared bands present in the spectral region between 800 and 1000 cm^{-1} are most probably due to vibrations in three and four coordinated boron units structure.¹¹⁰ Beginning with $x = 0.40$ small infrared bands around 1225 cm^{-1} assigned to the stretching vibration of the B-O bond¹¹⁰ are observed. The presence of a more linked boron structure at $x = 0.90$ is further evidenced by the appearance of a better defined infrared band centred at 1430 cm^{-1} which is attributed to boroxol units vibrations.¹¹⁰

In the Raman spectra of heat-treated samples for $x \geq 0.30$ (Fig. 6.12) the presence of the wide bands demonstrates the existence of a higher disorder degree in the structure of the bismuth-borate glasses. The bands that indicate the presence of the Bi^{3+} cations as $[\text{BiO}_6]$ octahedral units can be again observed in the Raman spectra of treated samples in the 50-180 cm^{-1} spectral range. The broadening of the bands and the shift to higher wavenumbers of the band centred at 326 cm^{-1} , for samples with $x \leq 0.20$, evidence the appearance of highly distorted $[\text{BiO}_6]$ polyhedra. As it was already mentioned the position and the shape of the Raman bands of the heat-treated samples are very similar with those of the untreated glasses at the same concentrations. However, it should be noted that at very small Bi_2O_3 content, $x = 0.90$, while bands given by bismuthate groups diminish substantially, the Bi-O-Bi vibration even disappearing, a stronger linkage of the boron structure occurs.⁵⁶ This assumption is better evidenced by the increasing of the boroxol units vibrations reflected by the band centred at 806 cm^{-1} , in the Raman spectrum of the treated sample compared to the corresponding Raman spectrum of the untreated glass at the above-mentioned concentration.

6.2.3. Conclusion

By analysing Raman and infrared spectra of 95% $[xB_2O_3(1-x)Bi_2O_3]5\%Fe_2O_3$ system it was found that Bi^{3+} cations are incorporated in the untreated glass network as $[BiO_6]$ polyhedra, in the heat-treated samples with $x \leq 0.20$ as $[BiO_3]$ pyramidal and $[BiO_6]$ octahedral units and as distorted $[BiO_6]$ polyhedra for $x > 0.20$. The spectra of the heat-treated samples evidence that the glass stability is decreasing as the bismuth concentration increases. After 10 hours heat treatment at 575 °C, only the sample with highest boron content, $x > 0.20$, remains non-crystalline while all the others crystallize. It is remarkable that only the $Bi_{24}B_2O_{39}$ crystalline phase is formed that points out that the relatively high iron doped content stabilizes the glass network in the compositional region corresponding to the $Bi_4B_2O_9$ phase. The influence of the boron network on the bismuth structural units in the heat-treated samples with high B_2O_3 concentration ($x = 0.90$) is increased and is evidenced by the disappearing of the Bi-O-Bi Raman vibrations. On the other hand, a strong disordering effect of Bi_2O_3 on the vitreous B_2O_3 network occurs.

In comparison to previous studies on bismuth-borate glasses doped with 0.5% Fe_2O_3 the results obtained in the present study show that the higher iron content (5% Fe_2O_3) strongly influences the structure of the bismuth-borate matrices, determining a more ordered bismuth vicinity, and stabilizing the glass network in the compositional region with relatively high bismuth concentration ($x = 0.20$).

7

Summary/Zusammenfassung

7.1. Summary

The presented work consists of two major parts. The first one (chapters 4 and 5) contains theoretical and experimental applications of confocal micro-Raman spectroscopy on hybrid polymer coatings and PDMS membranes. The spatial dimensions of the focus inside the coated sample have been investigated, which lead to a better understanding of the physical phenomena occurring in such samples. The same spectroscopic technique has also been used to determine the diffusion properties of β -carotene across PDMS membranes. These investigations are extremely important since for the development of controlled drug release systems the knowledge and control of diffusion properties of the investigated membrane are of utmost relevance.

The second part (chapter 6) presents structural investigations of copper and iron doped B_2O_3 - Bi_2O_3 glass systems obtained by means of infrared absorption and Raman spectroscopy. The local structure of the glasses, before and after thermal treatment, has been determined, demonstrating the great capability of these techniques in structural analysis of amorphous and partially crystallized materials. The conclusions drawn from the above mentioned studies are summarized in the next paragraphs.

In chapter 4 a detailed analysis based on ray tracing has been applied in order to compute the confocal micro-Raman response profile at different depths inside of two different coated samples, of 6.2 and 20.2 μm thickness. By considering the spherical aberrations induced by the presence of the air/coating interface, a focus lengthening has been evidenced. The agreement between theoretical and experimental data was fairly good. Furthermore, a theoretical approach that considers both the effects of refraction and diffraction on the focus lengthening on confocal micro-Raman experiments has been developed. A calculation of the confocal micro-Raman response profile as a function of the apparent focal point Δ , numerical aperture and magnification of the objective (NA , Γ_0), refractive index of the sample n , and the characteristics of the pinhole and the laser beam (R_a , R_0) for different z_m^l levels into the sample has been performed. By applying the developed theoretical model a good agreement between theoretical and experimental data was observed. According to this approach, the lengthening of the focus deeper into the sample becomes less pronounced as compared to the case when only the refraction effect is considered. The intensity of the Raman response given by the substrate is already increased in the neighborhood of the substrate level, preventing thus a sharp discrimination. It was also shown that a better discrimination of the confocal Raman response proceeding from different levels along the optical axis could be obtained, if the thickness of the coating is smaller. By taking into account both the diffraction and refraction effects a shortening of the focal length is obtained in comparison to the model, where only the refraction was considered, thus an improvement of the agreement between the experimental and theoretical data, particularly at the coating/substrate interface being obtained.

Confocal Raman spectroscopy has been applied to investigate the kinetics of diffusion processes through PDMS membranes before reaching steady state conditions and have been presented in chapter 5. Conventional methods used so far to study diffusion processes across membranes determine rate and extent (dm/dt) by which a substance is released from the membrane under steady state conditions. By applying confocal micro-Raman spectroscopy the dynamics of a diffusion process at well-defined points inside the membrane can be monitored. As shown in this chapter before reaching steady state conditions of diffusion the formation of a concentration gradient at a specific point inside the membrane can be observed. By determining changes in the intensity of characteristic peaks or even shifts of their wavenumber, changes in the concentration or the structure of the permeating substances or the membrane respectively can be seen. As an example we investigated the diffusion of β -carotene dissolved in DMSO through a PDMS membrane. β -carotene is especially suited for this experiment since our Raman excitation laser was resonant with an electronic absorption of β -carotene. This leads to a strong intensity enhancement of the observed Raman signal, and offers the possibility to detect even low concentrations of β -carotene. In this chapter, the diffusion rate as a function of the measurement depth and diffusion time within a membrane, before the steady state has been reached, was determined. We could show that at a given time before reaching a steady flux the slope of the concentration gradient, which is proportional to the rate and extent of diffusion, decreases with increasing penetration depth. The concentration gradient under a steady flux has been additionally investigated. According to the very low mass flow of β -carotene through the membrane only a small gradient can be observed. The measurements presented in this chapter have shown that confocal resonant micro-Raman technique is a powerful tool to investigate the kinetics of diffusion processes within a membrane before the steady state has been reached. It was further shown that by utilising the resonance Raman effect even low concentrations of the permeating substance can be detected. This offers the possibility to investigate the diffusion properties e.g. of pharmaceutically relevant molecules through membranes by using a dye laser as Raman excitation laser and adjusting its wavelength to be resonant with an electronic absorption of the investigated molecule.

In chapter 6 Raman and infrared spectral investigations of 99.5% $[xB_2O_3(1-x)Bi_2O_3]0.5\%CuO$ and 95% $[xB_2O_3(1-x)Bi_2O_3]5\%Fe_2O_3$ systems have been performed. It was evidenced that Bi^{3+} cations are incorporated in the untreated glass network of the first system as $[BiO_3]$ pyramidal and $[BiO_6]$ octahedral units for $x = 0.07$ and as distorted $[BiO_6]$ polyhedra for $0.20 \leq x \leq 0.625$, while in the other one they take part in the glass network only as $[BiO_6]$ polyhedra. Raman and infrared spectra of samples after heat treatment show first of all that the glass stability is decreasing as bismuth content increases. After 10 hours heat treatment at 575 °C, applied to the 99.5% $[xB_2O_3(1-x)Bi_2O_3]0.5\%CuO$ glass system only the sample with highest boron content, $x = 0.625$, remains non-crystalline while all the others partially crystallize. A similar structural behavior was also observed for the second system but in this case the sample remains non-crystalline for $x > 0.20$. For the latter system it is remarkable that only the $Bi_{24}B_2O_{39}$ crystalline phase is formed that points out the relatively high iron doped content stabilizes the glass network in the compositional region corresponding to the $Bi_4B_2O_9$ phase. A close analysis of the Raman and infrared spectra of the 99.5% $[xB_2O_3(1-x)Bi_2O_3]0.5\%CuO$ system revealed that the presence of copper ions has an influence on bismuth surrounding, favourizing the formation of $[BiO_3]$ units for untreated glasses with $x = 0.07$ and for treated samples with $x \leq 0.33$. The boron atoms in the heat-treated samples are three and four coordinated even for very high Bi_2O_3 content. From Raman and infrared spectra of the untreated 95% $[xB_2O_3(1-x)Bi_2O_3]5\%Fe_2O_3$ glasses it was found that in comparison to previous studies on iron doped bismuth-borate glasses with a content of 0.5% Fe_2O_3 the results obtained in the present study show that the higher iron content (5% Fe_2O_3) strongly influences the structure of the bismuth-borate matrices determining a more ordered bismuth vicinity and stabilizing the glass network in the compositional region with relatively high bismuth content ($x = 0.20$). The influence of the boron network on the bismuth structural units in the heat-treated samples with high B_2O_3 content ($x = 0.90$) is increased and is evidenced by the disappearing of the Bi-O-Bi Raman vibrations. In both heat-treated systems a strong disordering effect of Bi_2O_3 on the vitreous B_2O_3 network occurs.

7.2. Zusammenfassung

Die vorliegende Arbeit besteht aus zwei Teilen. Der erste Teil (Kapitel 4 und 5) beschäftigt sich mit theoretischen und experimentellen Untersuchungen der konfokalen Mikro-Raman-Spektroskopie hybrider Polymer-Schichten und PDMS-Membranen. Dabei wurden besonders die Dimensionen des Fokus in den Proben untersucht, um so einen tieferen Einblick in die bei solchen Messungen auftretenden physikalischen Phänomene zu erhalten. Desweiteren wurden die Diffusion von β -Carotin durch PDMS-Membranen mittels der konfokalen Mikro-Raman-Spektroskopie untersucht. Derartige Untersuchungen sind extrem wichtig für die Entwicklung neuer Applikationssysteme zur kontrollierten Wirkstofffreisetzung. Im zweiten Teil der vorliegenden Arbeit (Kapitel 6) werden strukturelle Untersuchungen an Kupfer- und Eisen-dotierten B_2O_3 - Bi_2O_3 Glas-Systemen mittels Infrarot- und Raman-Spektroskopie präsentiert. Die experimentellen und theoretischen Ergebnisse, die in den vorhergehenden Kapiteln beschrieben und diskutiert wurden, sollen im folgenden zusammengefasst werden.

In Kapitel 4 wurde zur Berechnung des konfokalen Mikro-Raman-Response-Profiles für verschiedene Eindringtiefen innerhalb zweier unterschiedlich beschichteter Proben mit $6,2 \mu\text{m}$ bzw. $20,2 \mu\text{m}$ Schichtdicke eine auf Strahlverfolgung basierende Analyse durchgeführt, wobei die sphärische Aberration, die an der Luft/Beschichtungsgrenzfläche entsteht, mit berücksichtigt wurde. Dabei konnte eine Fokusverlängerung festgestellt werden. Die theoretischen Ergebnisse wurden mit den experimentellen Daten verglichen, und es wurde eine gute Übereinstimmung festgestellt. Außerdem wurde ein theoretischer Ansatz entwickelt, der den Einfluss von Brechung und Beugung auf die Fokusverlängerung bei konfokalen Mikro-Raman-Experimenten beschreibt. Eine Berechnung des Raman-Response-Profiles als Funktion des scheinbaren Brennpunktes Δ , der numerischen Apertur und der Vergrößerung des Mikroskopobjektivs (NA, Γ_0) , des Brechungsindex der Probe n und der Eigenschaften der konfokalen Apertur und des Laserstrahls (R_d, R_0) wurde für verschiedene Ebenen z_m^l innerhalb der Probe durchgeführt. Die theoretischen Ergebnisse stimmen mit den expe-

rimentellen Daten überein. Bei diesem Ansatz ist die Fokusverlängerung bei größerer Eindringtiefe weniger ausgeprägt, verglichen mit dem Fall, dass nur Brechungseffekte berücksichtigt werden. Die Intensität des konfokalen Mikro-Raman-Responses des Substrates wird bereits in der Nähe der Substratebene erhöht und folglich eine scharfe Unterscheidung verhindert. Es wurde ebenfalls gezeigt, dass eine bessere Unterscheidung des konfokalen Raman-Responses, der von unterschiedlichen Ebenen entlang der optischen Achse ausgeht, erreicht werden kann, wenn die Dicke der Beschichtung klein ist. Im Vergleich zu dem Modell, das nur den Brechungseffekt in Betracht zieht, wird eine Verkürzung der Fokusslänge erreicht, wenn Brechungs- und Beugungseffekte betrachtet werden, was die Übereinstimmung zwischen experimentellen und theoretischen Daten verbessert, besonders an der Beschichtung/Substrat-Grenzfläche.

Als neue Möglichkeit zur Untersuchung der Diffusionskinetik vor Erreichen des stationären Zustands in PDMS-Membranen wurde die konfokale Raman-Spektroskopie eingesetzt und in Kapitel 5 dargestellt. Mit den bisher bekannten Methoden ist es nur möglich, Diffusionsvorgänge über die Membran als Ganzes im stationären Zustand zu beobachten. Bei der Raman-Spektroskopie wird das Probensystem während der Messung weder zerstört noch verändert. Weiterhin ist es möglich, durch das gekoppelte konfokale Mikroskopobjektiv an einem bestimmten Punkt innerhalb der Membran zu messen. Damit können nun dynamische Vorgänge wie der Aufbau eines Konzentrationsgradienten vor Erreichen des stationären Zustandes an einem bestimmten Punkt in einer Membran über einen längeren Zeitraum gemessen werden. Anhand von Intensitätsänderungen charakteristischer Peaks oder der Verschiebung von Banden werden Konzentrations- und Strukturänderungen der Membran und der permeierenden Moleküle sichtbar. Die Untersuchungen wurden am Beispiel der Diffusion einer β -Carotin/DMSO Lösung in PDMS-Membranen durchgeführt. β -Carotin ist für diese Raman-spektroskopischen Untersuchungen besonders gut geeignet, da durch Einstrahlung des Anregungslichtes in die Absorptionsbande bei 514 nm eine Resonanzverstärkung auftritt. Dies ergibt eine starke Intensitätsverstärkung des beobachteten Ramansignals. Folglich kann man auch sehr niedrige Konzentrationen der permeierenden Moleküle nachweisen. Zunächst wurden mit der konfokalen Raman-Spektros-

kopie Untersuchungen der Diffusionskinetik vor Erreichen des stationären Zustandes durchgeführt. Hierbei konnte die Diffusionsgeschwindigkeit in Abhängigkeit von der Messtiefe und der Messzeit ermittelt werden. In diesem Kapitel wurde gezeigt, dass die Steigung des Konzentrationsgradienten, d. h. dass die Diffusionsgeschwindigkeit, vor Erreichen des stationären Flusses in einem gegebenen Zeitintervall mit zunehmender Messtiefe kontinuierlich abnimmt. Es wurde zusätzlich der Konzentrationsgradient im stationären Fluss von β -Carotin in PDMS-Membranen untersucht. Aufgrund des geringen Massenstroms von β -Carotin durch die Membran ist der Gradient nur sehr klein. Die Untersuchungen mit der konfokalen Resonanz-Mikro-Raman-Spektroskopie zeigten, dass diese Methode geeignet ist, Diffusionskinetiken im nicht stationären Zustand innerhalb der Membranen zu beobachten. Die Ausnutzung des Resonanz-Raman-Effekts erlaubt es, die Diffusionseigenschaften z.B. pharmazeutisch relevanter Moleküle durch Membranen zu untersuchen, indem man durchstimmbare Laser als Anregungsquelle verwendet und die Wellenlänge in Resonanz zur elektronischen Absorption der diffundierenden Moleküle wählt.

Im Kapitel 6 wurden Raman- und Infrarot-spektroskopische Untersuchungen der Systeme $99,5\% [x\text{BO}_3(1-x)\text{Bi}_2\text{O}_3]0,5\%\text{CuO}$ und $95\% [xB_2\text{O}_3(1-x)\text{Bi}_2\text{O}_3]5\%\text{Fe}_2\text{O}_3$ durchgeführt. Es wurde gezeigt, dass Bi^{3+} -Kationen in das unbehandelte Glas-Netzwerk des ersten Systems für $x = 0,07$ als pyramidale $[\text{BiO}_3]$ - und octaedraedrische $[\text{BiO}_6]$ -Einheiten und für $0,20 \leq x \leq 0,625$ als verzerrte $[\text{BiO}_6]$ -Polyeder eingebaut werden, während sie im zweiten System nur als $[\text{BiO}_6]$ -Polyeder vorliegen. Raman- und Infrarot-Spektren der Proben nach Wärmebehandlung zeigen zunächst, dass sich die Glasstabilität verringert, wenn der Bismutgehalt zunimmt. Nach zehnstündiger Wärmebehandlung des Glassystems $99,5\% [xB_2\text{O}_3(1-x)\text{Bi}_2\text{O}_3]0,5\%\text{CuO}$ bei $575\text{ }^\circ\text{C}$ bleibt nur die Probe mit höchstem Borgehalt, $x = 0,625$, nichtkristallin, während alle anderen teilweise kristallisieren. Ein ähnliches strukturelles Verhalten wurde auch für das zweite System beobachtet, aber in diesem Fall sind die Proben für $x > 0,20$ nichtkristallin. Für letzteres System ist es bemerkenswert, dass nur eine $\text{Bi}_{24}\text{B}_2\text{O}_{39}$ -kristalline Phase gebildet wurde, was darauf hinweist, dass der relativ hohe Gehalt an Eisen-Dotierung das Glas-Netzwerk in der Zustandsregion der $\text{Bi}_4\text{B}_2\text{O}_9$ -Phase stabilisiert. Eine genaue Analyse von Raman- und Infrarot-Spektrum des $99,5\% [x\text{BO}_3$

(1-x)Bi₂O₃]0,5%CuO Systems zeigte, dass das Vorhandensein von Kupfer-Ionen die Bismut-Umgebung in der Weise beeinflusst, dass die Anordnung als [BiO₃]-Einheiten für unbehandeltes Glas mit $x = 0,07$ und für behandelte Proben mit $x \leq 0,33$ bevorzugt wird. Die Boratome in den wärmebehandelten Proben sind dreifach und vierfach koordiniert, sogar bei sehr hohem Gehalt an Bi₂O₃. Aus Raman- und Infrarot-Spektren von unbehandeltem 95% [xB₂O₃(1-x)Bi₂O₃]5%Fe₂O₃-Glas wurde im Vergleich zu vorhergehenden Studien an Eisen dotierten Bismut-Borat Gläsern mit einem Gehalt von nur 0,5% Fe₂O₃ geschlossen, dass der höhere Eisen-Gehalt (5% Fe₂O₃) die Struktur der Bismut-Borat Matrix stark beeinflusst, so dass in der Nachbarschaft von Bismut eine größere Ordnung festzustellen ist und das Glas-Netzwerk in einer Zustandsregion mit relativ hohem Bismut-Gehalt ($x = 0,20$) stabilisiert wird. Der Einfluss des Bor-Netzes auf die strukturellen Einheiten des Bismuts in den wärmebehandelten Proben mit hohem B₂O₃-Gehalt ($x = 0,90$) wird erhöht, was das Verschwinden der Bi-O-Bi-Ramanschwingungen beweist. In beiden wärmebehandelten Systemen tritt ein starker Störeffekt durch Bi₂O₃ im B₂O₃ Glas-Netzwerk auf.

References

- [1] W. Herschel, *Phil. Trans. Roy. Soc.*, **90**, 284 (1800).
- [2] P. R. Griffiths, J. A. de Haseth, *Fourier transform Infrared spectroscopy*, in: *Chemical Analysis*, Vol. 83, P. J. Elving, J. D. Winefordner, I. M. Kolthoff (eds.), John Wiley&Sons, New York (1986).
- [3] F. A. Miller, *Anal. Chem.*, **64**, 825 A (1992).
- [4] P. A. Wilks, *Anal. Chem.*, **64**, 833 A (1992).
- [5] P. R. Griffiths, *Anal. Chem.*, **64**, 868 A (1992).
- [6] N. Sheppard, *Anal. Chem.*, **64**, 877 A (1992).
- [7] A. O. Beckman, *Anal. Chem.*, **49**, 8280 A (1977).
- [8] C. V. Raman, K. S. Krishnan, *Nature*, **121**, 501 (1928).
- [9] A. G. Smekal, *Naturwissenschaften*, **11**, 873 (1923).
- [10] G. D. Landsberg, L. I. Mandelstam, *Naturwissenschaften*, **16**, 557 (1928).
- [11] G. Placzek, *Rygleigh Streuung und Ramaneffekt*, in: *Handbuch der Radiologie*, Vol. 6, G. Marx (ed.), Akad. Verlagsgesellschaft, Leipzig (1934).
- [12] K. W. F. Kohlrausch, *Der Smekal-Raman –Effekt*, in: *Struktur und Eigenschaften der Materie*, Vol. XIX, Springer Verlag, Berlin (1938).
- [13] K. W. Kohlrausch, *Ramanspektren*, in: *Hand- und Jahrbuch der Chemischen Physik*, Vol. 9, Part. VI, Akad. Verlagsgesellschaft, Leipzig (1943).
- [14] J. Brandmüller, H. Moser, *Einführung in die Ramanspektroskopie*, Dr. Dietrich Steinkopff Verlag, Darmstadt (1962).

References

- [15] T. R. Gilson, P. J. Hendra, *Laser Raman spectroscopy*, Wiley-Interscience, London (1970).
- [16] P. Hendra, C. Jones, G. Warnes, *Fourier Transform Raman Spectroscopy*, Ellis-Horwood, New York (1991).
- [17] D. A. Long, *Raman Spectroscopy*, McGraw Hill, New York (1977).
- [18] C. E. Hathaway, *Raman Instrumentation and Techniques*, in: *The Raman Effect*, Vol. 1, A. Anderson, M. Dekker Inc., New York (1971).
- [19] P. M. Fredericks, *Depth Profiling by Microspectroscopy*, in: *Handbook of Vibrational Spectroscopy: Theory and Instrumentation*, Vol. 2, J. M. Chalmers, P. R. Griffiths (eds.), John Wiley&Sons, Chichester (2002).
- [20] M. Delhaye, P. Dhamelinourt, *J. Raman Spectrosc.*, **3**, 33 (1975).
- [21] J. M. Delaye, *Current opinion in Solid State and Materials Science*, **5**, 451 (2001).
- [22] B. Schrader, *Infrared and Raman Spectroscopy: Methods and applications*, VCH Verlagsgesellschaft, Weinheim (1995).
- [23] P. M. Morse, *Phys. Rev.*, **34**, 57 (1929).
- [24] A. I. Kitaigorodski, *Molecular Crystals and Molecules*, Academic Press, New York (1973).
- [25] A. J. Pertsin, A. I. Kitaigorodski, *The atom-atom potential method*, Springer, Berlin (1987).
- [26] E. B. Wilson, J. C. Decius, P. C. Cross, *Molecular Vibrations, The Theory of Infrared and Raman Vibrational Spectra*, McGraw-Hill, New York (1955).
- [27] S. Califano, *Vibrational States*, John Wiley & Sons, New York London (1976).
- [28] P. Dhamelinourt, *Raman Microscopy*, in: *Handbook of Vibrational Spectroscopy: Theory and Instrumentation*, Vol. 2, J. M. Chalmers, P. R. Griffiths (eds.), John Wiley&Sons, Chichester (2002).
- [29] T. Wilson, C. Sheppard, *Theory and Practice of Scanning Optical Microscopy*, Academic Press, London (1984).
- [30] T. Wilson, *Confocal Microscopy*, Academic Press, London (1990).
- [31] J. Brakenhoff, H. T. Van Der Voort, N. Nanninga, *Anal. Chem. Acta*, **163**, 213

References

- (1984).
- [32] C. Sheppard, *J. Phys. D*, **19**, 2077 (1986).
- [33] J. Behringer, *Raman Spectroscopy: Theory and Practice*, Vol. 1, Szymanski HA (ed.) Raman Spectroscopy, Plenum, New York, (1967).
- [34] J. Tang, A. C. Albrecht, *Developments in the theories of vibrational Raman intensities*, Szymanski HA, Plenum, New York (1970).
- [35] J. Behringer, *Molecular Spectroscopy*, Vol. 2, R. F. Barrow, D. A. Long, D. J. Millen (eds.) The Chemical Society, London (1974).
- [36] J. Behringer, *Molecular Spectroscopy*, Vol 3, R. F. Barrow, D. A. Long, D. J. Millen (eds.) The Chemical Society, London (1975).
- [37] T. G. Spiro, T. M. Loehr, *Advances in Infrared and Raman Spectroscopy*, Vol 1, R. J. H. Clark, R. E. Hester (eds.), Heyden and Son, New York (1975).
- [38] R. J. H. Clark, *Advances in Infrared and Raman Spectroscopy*, Vol. 1, R. J. H. Clark, R. E. Hester (eds.), Heyden, London (1975).
- [39] W. Richter, *Solid State Physics*, Vol. 78, G. Höhler (ed.), Springer Tracts in Modern Physics, Springer, Berlin (1976).
- [40] W. Kiefer, *Recent Techniques in Raman Spectroscopy*, In: *Advances in Infrared and Raman Spectroscopy*, Vol. 3, R. J. H. Clark, R. E. Hester (eds.), Heyden, London (1977).
- [41] D. L. Rousseau, J. M. Friedman, P. F. Williams, *Raman Spectroscopy of Gases and Liquids*, Vol. 11, A. Weber (ed.), Topics in Current Physics, Springer, Berlin (1979).
- [42] P. R. Carey, V. R. Salares, *Raman and resonance Raman studies of biological systems*, In: *Advances in Infrared and Raman Spectroscopy*, R. J. H. Clark, R. E. Hester (eds.), Heyden and Son, London (1980).
- [43] D. N. Batchelder, D. Bloor, *Advances in Infrared and Raman Spectroscopy*, Vol. 11, R. J. H. Clark, R. E. Hester (eds.), Heyden, London (1984).
- [44] D. Lee, A. C. Albrecht, *Advances in Infrared and Raman Spectroscopy*, Vol. 12, R. J. H. Clark, R. E. Hester (eds.), Heyden, London (1985).
- [45] T. G. Spiro, *Biological Applications of Raman Spectroscopy*, Vol. 2, Wiley, New

References

- York (1987).
- [46] A. B. Myeres, R. A. Mathies, *Biological Applications of Raman Spectroscopy*, Vol. 2, Wiley, New York (1987).
- [47] B. S. Hudson, L. M. Markhan, *J. Raman Spectrosc.*, **29**, 480 (1998).
- [48] A. Weber, D. E. Jennings, J. W. Brault, *High resolution Raman spectroscopy of gases with a Fourier transform spectrometer*, Proceedings IXth International Conference on Raman Spectroscopy, Tokyo, pp. 58-61 (1984).
- [49] D. E. Jennings, A. Weber, J. W. Brault, *Raman spectroscopy of gases with a Fourier transform spectrometer: The spectrum of D₂*, *Appl. Optics*, **25**, 284 (1986).
- [50] D. B. Chase, J. F. Rabolt, *Fourier Transform Raman spectroscopy: From concept to experiment*, In: D. B. Chase, J. F. Rabolt (eds.), *Fourier Transform Raman spectroscopy*, San Diego, Academic Press (1994).
- [51] G. W. Chantry, H. A. Gebbie, C. Helsum, *Interferometric Raman spectroscopy using infrared excitation*, *Nature* **203**, 1052 (1964).
- [52] T. Hirschfeld, B. Chase, *Appl. Spectrosc.*, **40**, 133 (1986).
- [53] U. Posset, M. Lankers, W. Kiefer, H. Steins, G. Schottner, *Appl. Spectrosc.*, **47**, 1600 (1993).
- [54] B. Weh, *Permeationseigenschaften von Polydimethylsiloxan-Membranen in Abhängigkeit von der Netzbogenlänge*, *Dissertation*, Universität Würzburg, (2002).
- [55] L. Baia, R. Stefan, W. Kiefer, J. Popp, S. Simon, *J. Non-Cryst. Solids*, **303**, 379 (2002).
- [56] L. Baia, R. Stefan, J. Popp, S. Simon, W. Kiefer, *J. Non-Cryst. Solids*, submitted.
- [57] L. Baia, D. Maniu, T. Iliescu, S. Simon, S. Schlücker, W. Kiefer, *Asian J. Physics*, **9**, (1) 51 (2000).
- [58] N. J. Overall, *Appl. Spectrosc.*, **54** (6), 773 (2000).
- [59] G. Rosasco, *Raman Microprobe Spectroscopy*, in *Advances in IR and Raman Spectroscopy*, Vol. 7, Chap. 4, R. Clark and R. Hester (eds.), Heydon, London (1980).

References

- [60] D. J. Gardiner, M. Bowden, P. R. Graves, *Phil. Trans. Roy. Soc., Lond.* **A320**, 295 (1986).
- [61] G. J. Puppels, W. Colier, J. H. F. Olminkhof, F. F. H. de Mul, J. Greve, *J. Raman Spectrosc.*, **22**, 217 (1991).
- [62] R. Tabaksblat, R. J. Maier, B. J. Kip, *Appl. Spectrosc.*, **46**, 60 (1992).
- [63] K. P. J. Williams, G. D. Pitt, D. N. Batchelder, B. J. Kip, *Appl. Spectrosc.*, **48**, 232 (1994).
- [64] S. Hajatdoost, J. Yarwood, *Appl. Spectrosc.*, **50**, 558 (1996).
- [65] S. Hajatdoost, J. Yarwood, *Appl. Spectrosc.*, **51**, 1784 (1997).
- [66] N. J. Everall, *Appl. Spectrosc.*, **52**, 1498 (1998).
- [67] L. Markwort, B. Kip, E. da Silva, B. Roussel, *Appl. Spectrosc.*, **49**, 1411 (1995).
- [68] N. J. Everall, *Appl. Spectrosc.*, **54** (10), 1515 (2000).
- [69] K. J. Baldwin, D. Batchelder, *Appl. Spectrosc.*, **55**, 5 (2001).
- [70] S. Amenlinckx, D. van Dyck, J. van Landuyt, G. van Tendeloo, *Handbook of Microscopy, Applications in Material Science, Solid State Physics and Chemistry Methods I*, VCH Weinheim (1997), pp. 55-69.
- [71] B. Matsumoto, *Cell Biological Applications of confocal Microscopy*, Academic Press INC (1993), pp. 62-64.
- [72] L. Baia, K. Gigant, U. Posset, G. Schottner, W. Kiefer, J. Popp, *Appl. Spectrosc.*, **56** (4), 536 (2002).
- [73] L. Baia, K. Gigant, U. Posset, R. Petry, G. Schottner, W. Kiefer, J. Popp, *Vib. Spectrosc.*, **29**, 245 (2002).
- [74] L. Baia, K. Gigant, U. Posset, G. Schottner, W. Kiefer, J. Popp, *Proceedings of XVIII-th International Conference on Raman spectroscopy*, John Wiley&Sons, Budapest (2002).
- [75] R. A. Zaffaroni, *Medicinal Research Reviews*, **1** (4), 373 (1981); A. Zaffaroni, *Annals of the New York Academy of Sciences*, **618**, 405 (1991); A. Zaffaroni, *Drug metabolism reviews*, **8** (2), 191 (1978).
- [76] S. J. Desai, W. I. Higuchi, A. P. Simonelli, *J. Pharmaceutical Science*, **54**,

References

- 1495 (1995).
- [77] K. E. Pomanteer, *Rubber Chemistry and Technology*, **61**, 470 (1988).
- [78] G. F. Gregory, *British Journal of oral and maxillofacial surgery*, **33**, 180 (1995).
- [79] P. C. Schmidt, *Pharmazeutische Zeitung*, **146**, 2092 (2001).
- [80] K. W. Leong, *American Society for testing and Materials (ASTM): Standardization News*, **14**, 50 (1986).
- [81] F. Kydonieus, *Controlled Release Technologies - Fundamental Concepts of Controlled Release* (1980).
- [82] B. Mattsson, H. Ericson, L. M. Torell, F. Sundholm, *J. Polym. Sci. Part A Polym. Chem.*, **37**, 3317 (1999).
- [83] B. Mattsson, H. Ericson, L. M. Torell, F. Sundholm, *Electrochimica Acta*, **45**, 1405 (2000).
- [84] P. Tomba, J. M. Carella, J. M. Pastor, M. R. Fernández, *Macromol., Rapid Commun.*, **19**, 413(1998).
- [85] J. Sacristán, C. Mijangos, H. Reinecke, S. Spells, J. Yarwood, *Macromolecules*, **33**, 6134 (2000).
- [86] J. Sacristán, H. Reinecke, C. Mijangos, S. Spells, J. Yarwood, *Macromol. Chem. Phys.*, **203**, 678 (2002).
- [87] R. J. Erckens, F. H. M. Jongsma, J. P. Wicksted, F. Hendrikse, W. F. March, M. Motamedi, *J. Raman Spectrosc.*, **32**, 733 (2001).
- [88] N. J. Bauer, M. Motamedi, J. P. Wicksted, W. F. March, C. A. Webers, F. Hendrikse, *J. Ocular Pharmacology and Therapeutics*, **15**, 123 (1999).
- [89] N. J. Bauer, J. P. Wicksted, F. H. Jongsma, W. F. March, F. Hendrikse, M. Motamedi, *Investigative Ophthalmology and Visual Science*, **39**, 831 (1999).
- [90] A. N. Yaroslavskaya, I. V. Yaroslavsky, C. Otto, G. J. Puppels, H. Duindam, G. F. J. M. Vrensen, J. Greve, V. V. Tuchin, *Biofizika*, **43**, 125 (1998).
- [91] J. Crank, *The mathematics of diffusion*, Clarendon Press, Oxford (1995).
- [92] M. Schmitt, B. Leimeister, L. Baia, W. Kiefer, B. Weh, I. Zimmermann, J. Popp, *Chem. Phys. Chem.*, accepted.
- [93] D. W. Hall, M. A. Newhouse, N. F. Borelli, W. H. Dumbaugh, D. L. Weidman,

References

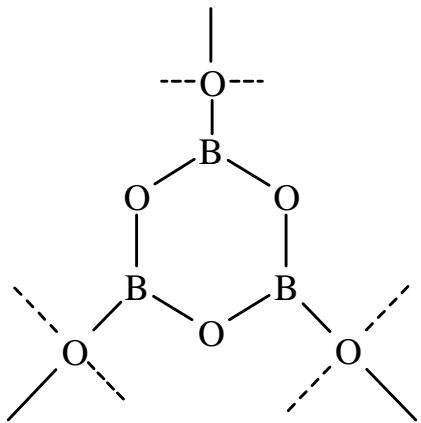
- Appl. Phys. Lett.*, **54**, 1293 (1989).
- [94] A. Gosh, *J. Appl. Phys.*, **64**, 2652 (1988).
- [95] K. Gerth, C. Rüssel, *J. Non-Cryst. Solids*, **221**, 10 (1997).
- [96] K. Fajans, N. Kreidl, *J. Am. Ceram. Soc.*, **31**, 105 (1948).
- [97] G. Cordoba, R. Arroyo, J. L. Fierro, M. Viniegra, *J. Solid State Chem.*, **123**, 93 (1996).
- [98] F. Perez-Robles, F. J. Garcia-Rodriguez, S. Jimenez-Sandova, J. Gonzales-Hernandez, *J. Raman Spectr.*, **30**, 1099 (1999).
- [99] J. Krogh-Moe, *Phys. Chem. Glasses*, **3**, 101 (1962).
- [100] R. L. Mozzi, B. E. Waren, *J. Appl. Crystallogr.*, **3**, 251 (1970).
- [101] B. P. Dwivedi, M. H. Rahman, Y. Kumar, B. N. Khanna, *J. Phys. Chem. Solids*, **54** (5), 621 (1993).
- [102] B. N. Meera, J. Ramakrishna, *J. Non-Cryst. Solids*, **159**, 1 (1993).
- [103] A. A. Kharlamov, R. M. Almeida, J. Heo, *J. Non-Cryst. Solids*, **202**, 233 (1996).
- [104] V. Dimitrov, Y. Dimitriev, A. Montenero, *J. Non-Cryst. Solids*, **180**, 51 (1994).
- [105] R. Iordanova, V. Dimitrov, Y. Dimitriev, D. Klissurski, *J. Non-Cryst. Solids*, **180**, 58 (1994).
- [106] S. Hazra, S. Mandal, A. Ghosh, *Phys. Review B*, **56**, 13 8021 (1997).
- [107] S. Hazra, A. Gosh, *Phys. Review B*, **51**, (2) 851(1995).
- [108] Y. Dimitriev, M. Mihailova, *Proc. 16th Int. Congress on Glass*, Madrid, Vol. 3 (1992), p. 293.
- [109] E. I. Kamistos, M. A. Karakassides, G. D. Chryssikos, *Phys. and Chem. Glasses*, **30**, (6) 229 (1989).
- [110] W. L. Konijnendijk, The structure of borosilicate glasses, *PhD doctoral dissertation*, UT Eindhoven (1975).
- [111] S. Simon, *XIX Int. Congress on Glasses*, Edinburgh, Scotland, Vol.2 (2001) p. 616.
- [112] D. Ilieva, B. Jivov, G. Bogacev, C. Petkov, I. Penkov, Y. Dimitriev, *J. Non-Cryst. Solids*, **283**, 195 (2001).
- [113] R. Iordanova, Y. Dimitriev, V. Dimitrov, S. Kassabov, D. Klissurski, *J. Non-*

References

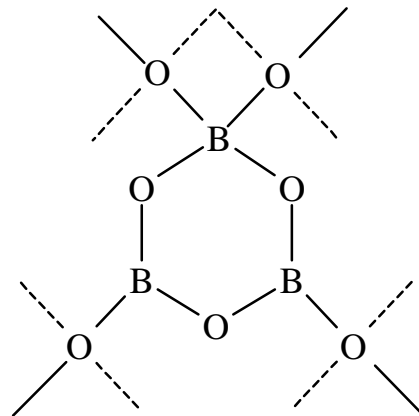
- Cryst. Solids*, **231**, 227 (1998).
- [114] C. Stehle, C. Vira, D. Vira, D. Hogan, S. Feller, M. Affatigato, *Phys. Chem. Glasses*, **39**, (2) 83 (1998).
- [115] N. Sugimoto, *J. Am. Ceram. Soc.*, **85**, 1083 (2002).
- [116] A. Bishay, C. Maghrabi, *Phys. Chem. Glasses*, **10**, 1 (1969).
- [117] W. H. Dumbaugh, *Phys. Chem. Glasses*, **27**, 119 (1986).
- [118] M. Iron. M. Couzi, A. Levasseur, J. M. Reau, J. C. Brethous, *J. Solid-State Chem.*, **31**, 285 (1980).
- [119] F. L. Galeener, G. Lukovski, J. C. Mikkelsen Jr., *Phys. Rev. B*, **22**, 3983 (1980).
- [120] J. Lorösch, M. Couzi, J. Pelouz, R. Vacher, A. Lavaseur, *J. Non-Cryst. Solids*, **69**, 1 (1984).
- [121] G. E. Jellison Jr., P. J. Bray, *J. Non-Cryst. Solids*, **29**, 187 (1978).
- [122] P. J. Bray, S. A. Feller, G. E. Jellison Jr., J. H. Yuh, *J. Non-Cryst. Solids*, **38-39**, 93 (1980).
- [123] A. C. Wright, N. M. Vedischcheva, B. A. Shakhmatahin, *J. Non-Cryst Solids*, **192-193**, 92 (1995).
- [124] D. Holland, A. Mekki, I. A. Gee, Mc. Conville, J. A. Johnson, C. E. Johnson, P. Appleyard, M. Thomas, *J. Non-Cryst Solids*, **253**, 192 (1999).
- [125] A. Matthai, D. Ehrt, C. Rüssel, *Glass Science and Technology*, **71**, 187 (1998).
- [126] A. Mekki, D. Holland, Kh. A. Ziq, C. F. Mc. Conviollle, *J. Non-Cryst. Solids*, **272**, 179 (2000).
- [127] H. Zheng, R. Xu, J. Mackenzie, *J. Mater. Res.*, **4**, 911 (1989).
- [128] A. E. Miller, K. Nassau, K. B. Lyons, M. E. Lines, *J. Non-Cryst Solids*, **99**, 289 (1988).

Appendix

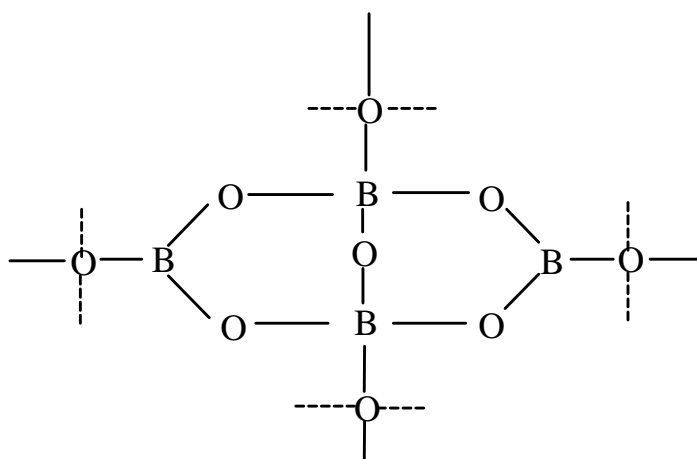
Various borate and bismuthate structural units present in glasses based on B_2O_3 and Bi_2O_3



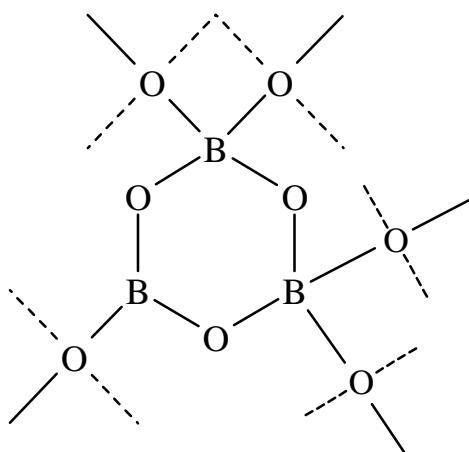
BOROXOL RING



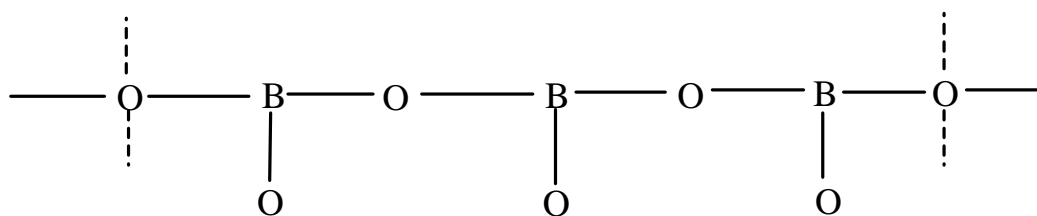
TRIBORATE GROUP



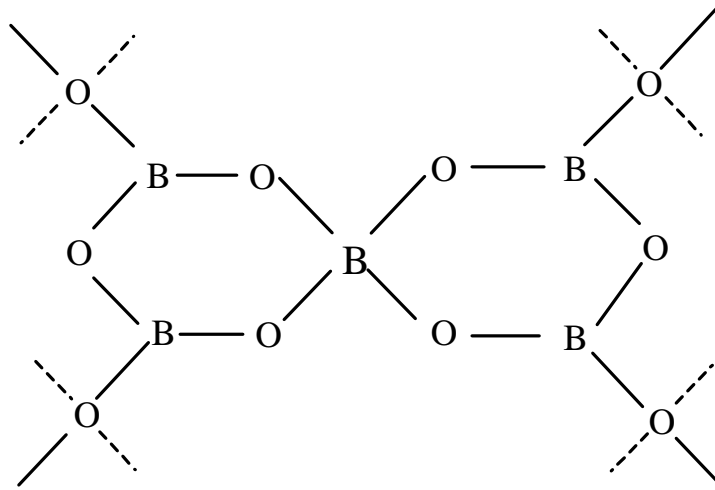
DIBORATE GROUP



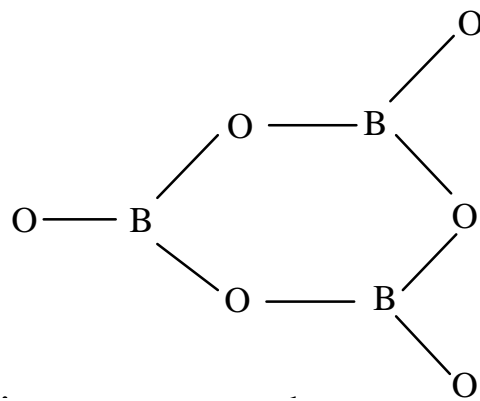
DI-TRIBORATE GROUP



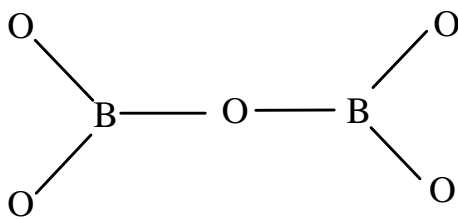
CHAIN-TYPE METABORATE GROUP



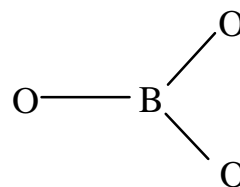
PENTABORATE GROUP



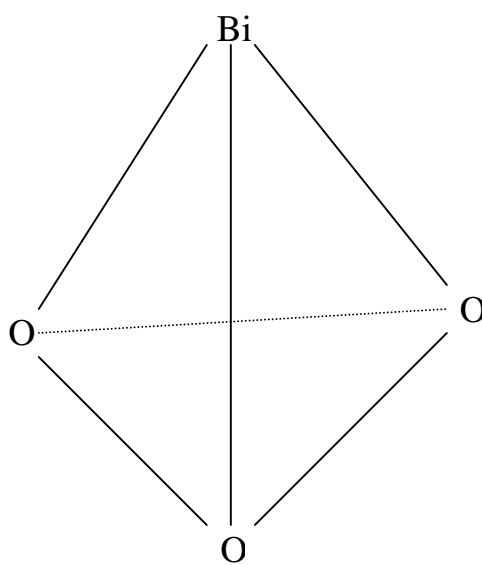
RING-TYPE METABORATE



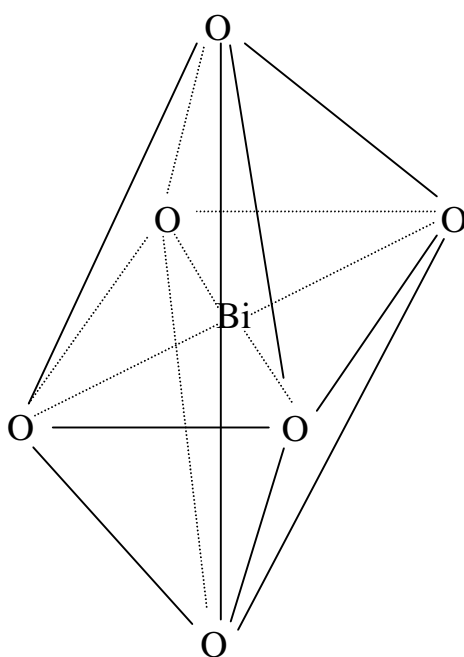
PYROBORATE GROUP



ORTHOBORATE GROUP



[BiO₃] PYRAMIDAL UNIT



[BiO₆] OCTAHEDRAL UNIT

Dank

An erster Stelle gilt mein besonderer Dank Herrn Prof. Dr. Wolfgang Kiefer und Herrn Prof. Dr. Jürgen Popp, die diese Arbeit im Rahmen des DFG Projektes (PO 563/2-1) ermöglichten und bei alle Fragen bzw. Problemen unterstützten. An dieser Stelle möchte ich mich auch für die Teilnahmemöglichkeit an mehreren internationalen Tagungen bedanken, erwähnt seien insbesondere die ICORS 2000 in Beijing und 2002 in Budapest sowie die ICAVS 2001 in Turku (Finnland).

Für die gute Zusammenarbeit im Rahmen des DFG Projektes möchte ich mich bei Dr. Uwe Posset und Karine Gigant, Mitarbeiter des Anwenderzentrums im Fraunhofer Institut für Silicatforschung in Würzburg, bedanken. Nicht nur die Proben wurden vorbereitet, sondern ich wurde bei der chemischen Fragestellung immer mit Rat und Tat unterstützt.

Ein herzlichen Dank geht an meine ehemaligen Professoren aus Rumänien, erwähnt seien insbesondere Frau Prof. Viorica Simon, Herrn Prof. Simion Simon und Herrn Prof. Gheorghe Cristea. Ich danke für die sehr guten Ratschläge und für die Zusammenarbeit.

Ein herzliches Dankeschön möchte ich Dr. Michael Schmitt, der diese Arbeit korrigiert hat, aussprechen. Mein Dank geht auch an Joachim Koster, Petra Meuer und Ralph Geßner für die Korrektur der deutschen Zusammenfassung. Belinda Leimeister danke ich für die Hilfsbereitschaft bei der Arbeit im Labor. Für die interessanten wissenschaftlichen Diskussionen möchte ich mich bei Dr. Barbara Weh bedanken.

Mein besonderer Dank gilt meinen Kollegen und ehemaligen Arbeitskreismitgliedern Cristina Dem, Krisztina Babocsi, Claudiu Dem, Nicu Tarcea, Nicolae Leopold, Dr. Oliver Sbanski und Dr. Victor Roman für die immer interessanten Gesprächsabende.

Ich danke allen, die mich während meiner Promotionszeit durch tatkräftige Hilfe oder gute Ratschläge unterstützt und so einen Beitrag zum Gelingen dieser Arbeit geleistet haben.

Zu guter Letzt danke ich Monica, die mich auf ihre Art ermutigte und mir während den letzten drei Jahren als wertvoller Diskussionspartnerin zur Seite stand.

Lebenslauf

Persönliche Daten

Name	Gheorghe Lucian Baia
Geboren am	12.04.1971
in	Tirnaveni
Familienstand	ledig

Ausbildung und Beruf

Schulbildung	1977 - 1981	Grundschule, Bahnea
	1981 - 1985	Gymnasium, Bahnea
	1985 - 1989	Industrie Gymnasium Nr. 2, Tirnaveni
Abitur	Juni 1989	
Wehrdienst	1989 - 1990	
Studium	1990 - 1995	Maschinenbaustudium an der Technischen Universität Cluj-Napoca
	Juni 1995	Lizenzprüfung
	1994 - 1998	Mathematik-Physikstudium an der Babes-Bolyai Universität Cluj-Napoca
	Juni 1998	Lizenzprüfung
	1998 - 1999	Masterstudium Physik der oxidischen Materialien an der Babes-Bolyai Universität Cluj-Napoca

	Juni 1999	Abschlussprüfung
Promotion	Okt. 1999	Beginn der Promotion am Lehrstuhl für Physikalische Chemie II der Universität Würzburg bei Prof. Dr. Wolfgang Kiefer
Anstellungen	Okt. 1999 - Dez. 1999 seit Jan. 2000	Wissenschaftliche Hilfskraft Wissenschaftlicher Mitarbeiter im DFG-Projekt PO 562/2-1.